All-optical assay to study biological neural networks

Wardiya Afshar Saber

A thesis submitted for the degree of PhD
at the
University of St Andrews

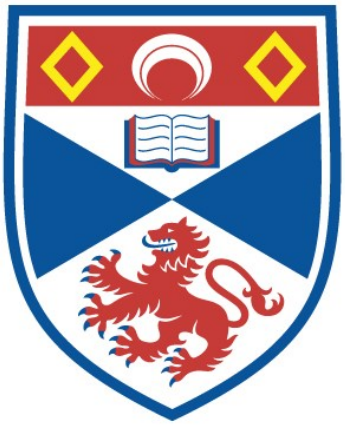

2019

Declaration

Candidate's declaration

I, Wardiya Afshar Saber, do hereby certify that this thesis, submitted for the degree of PhD, which is approximately 42,000 words in length, has been written by me, and that it is the record of work carried out by me, or principally by myself in collaboration with others as acknowledged, and that it has not been submitted in any previous application for any degree.

I was admitted as a research student at the University of St Andrews in May 2015.

I received funding from an organisation or institution and have acknowledged the funder(s) in the full text of my thesis.

Date Signature of candidate

Supervisor's declaration

I hereby certify that the candidate has fulfilled the conditions of the Resolution and Regulations appropriate for the degree of PhD in the University of St Andrews and that the candidate is qualified to submit this thesis in application for that degree.

Date Signature of supervisor

Permission for publication

In submitting this thesis to the University of St Andrews we understand that we are giving permission for it to be made available for use in accordance with the regulations of the University Library for the time being in force, subject to any copyright vested in the work not being affected thereby. We also understand, unless exempt by an award of an embargo as requested below, that the title and the abstract will be published, and that a copy of the work may be made and supplied to any bona fide library or research worker, that this thesis will be electronically accessible for personal or research use and that the library has the right to migrate this thesis into new electronic forms as required to ensure continued access to the thesis.

I, Wardiya Afshar Saber, confirm that my thesis does not contain any third-party material that requires copyright clearance.

The following is an agreed request by candidate and supervisor regarding the publication of this thesis:

Printed copy

Embargo on all of print copy for a period of 3 years on the following ground(s):

- Publication would preclude future publication

Supporting statement for printed embargo request

Publication would preclude further publication.

Electronic copy

Embargo on all of electronic copy for a period of 3 years on the following ground(s):

- Publication would preclude future publication

Supporting statement for electronic embargo request

Publication would preclude further publication.

Title and Abstract

- I agree to the title and abstract being published.

Date Signature of candidate

Date Signature of supervisor

Underpinning Research Data or Digital Outputs

Candidate's declaration

I, Wardiya Afshar Saber, hereby certify that no requirements to deposit original research data or digital outputs apply to this thesis and that, where appropriate, secondary data used have been referenced in the full text of my thesis.

Date Signature of candidate

Abstract

As life span increases, neurodegenerative diseases such as dementia, Parkinson's disease, Huntington's disease, amyotrophic lateral sclerosis become an emerging problem in modern society [2]. In particular Alzheimer's disease (AD), characterized by a progressive cognitive impairment and memory loss, is the dominant cause of disability in people aged over 60. Due to the lack of accurate models, understanding the disease mechanisms and developing a cure for AD remains challenging. However, a novel approach based on human induced pluripotent stem cell (iPSC) technology may offer an opportunity to overcome the limitations of the current models. These cells obtained by reprogramming patient's somatic cells such as fibroblasts can be differentiated *in vitro* into various types of neural cells which further develop complex networks. To explore these heterogeneous neural networks, it is often critical to understand the activity of multiple neurons and how they communicate with each other. The work presented in this thesis focuses on the development of the first molecular optogenetic tool called OptoCaMP used in an all-optical assay enabling simultaneous stimulation and calcium imaging of a large population of neurons with a single-cell readout [3]. This assay was further adapted to study the spread of excitation in a network thus allowing the quantification of its connectivity. The application of this assay in conditions where the neuronal connectivity was enhanced or decreased successfully demonstrated its sensitivity to changes in connectivity. This assay together with the iPSC technology bring the promise to greatly improve disease models studies and drug screening platforms [4].

Acknowledgements

To my supervisor Professor Frank J. Gunn-Moore, for his support, helpful advice and availability. I would like to particularly thank you for believing in me and for making my writing process such an enjoyable experience! To Dr Maciej Antkowiak, I am thankful for the opportunity you have given to me and I feel lucky to have had the chance to work with you. Thanks to our different scientific backgrounds, I have learned with you to innovate as a scientist and that science should always be viewed from a multidisciplinary perspective.

To my mentors Professor Philippe Ménasché, Professor Clifford Woolf, Dr Cédric Ghevaert and Dr Stéphane Bolduc who have inspired me, not only with their scientific achievements but also with their great personality and ethic. To all the amazing researchers I had the chance to interact with, in particular Dr Elizabeth Buttermore. Thank you for your availability, your advice and for sharing your passion.

To my fellows and friends who have brightened up this adventure. Thank you for the late nights “sciencing” in the lab, countless discussions and brainstorming but more importantly and simply for being such great friends. To my non-scientists friends who are very enthusiastic about my research and love to hear all about my adventures!

To my family, who has always believed in me and taught me to follow my dreams and aspirations. Words cannot explain how grateful I am for your unconditional support through this adventure. And finally, to my brother Ali, I feel extremely privileged to have you as a brother, protector and lifelong friend.

Funding

This work was supported by the Cunningham Trust PhD studentship and the Wellcome Trust Institutional Strategic Support Fund (ISSF), the RS MacDonald Charitable Trust Neurophotonics Grant, the EPSRC programme Grant EP/P030017/1 and the generous financial support of the University of St Andrews for my attendance at multiple conferences.

“Le progrès des sciences est l'ouvrage du temps et de la hardiesse de l'esprit.”

Voltaire.

“Search until you find a passion and go all out to excel in its expression…”

E.O Wilson.

Contents

List of Figures and Tables

List of Abbreviations

A

Aβ	amyloid-β
AD	Alzheimer's Disease
AMPA	α-Amino-3-hydroxy-5-methyl-4-isoxazole Propionic-Acid
AP	action potential
apoCaM	apocalmodulin
APOE	apolipoprotein E
APP	amyloid precursor protein
ASAP1	Accelerated Sensor of Action Potentials 1
ATP	adenosine triphosphate

B

BRET	Bioluminescence Resonance Energy Transfer
BDNF	Brain-derived neurotrophic factor
BP	BrainPhys

C

CaM	calmodulin
ChR	Channelrhodopsin
CNG	cyclic nucleotide-gated
CNQX	6-Cyano-7-nitroquinoxaline-2,3-dione
CNTF	Ciliary neurotrophic factor
CRISPR-Cas9	Short Palindromic Repeats-associated protein 9

D

D-APV	D(−)-2-Amino-5-phosphonopentanoic
DIV	days *in vitro*
DNA	Deoxyribonucleic acid

E

eGFP	enhanced Green Fluorescent Protein
eYFP	enhanced Yellow Fluorescent Protein

F

FRET	Fluorescence Resonance Energy Transfer
FDG	18F-2fluoro-2-deoxy-D-glucose

G

GDNF	Glial cell-derived neurotrophic factor
GECI	Genetically Encoded Calcium Indicator
GEVI	Genetically Encoded Voltage Indicator
GFAP	Glial Fibrillary Acid Protein
GFP	Green Fluorescent Protein

H

HEK	Human Embryonic Kidney
hiPSC	human induced Pluripotent Stem Cells
HVA	high-voltage-activated

I

iPSC	induced Pluripotent Stem Cells

L

LB	Luria-Bertani
LDH	lactate dehydrogenase
LED	light-emitting diode
LVA	low-voltage-activated

M

MAP2	Microtubule Associated Protein 2
MCBL	Multicell bolus loading
MCI	Mild Cognitive Impairment
MEAs	Multi-electrode arrays
MRI	magnetic resonance imaging
MTT	3-(4,5-dimethylthiazol-2-yl)-2,5-diphenyltetrazolium bromide

N

NA	Numerical Aperture
NB	Neurobasal
NCX	sodium-calcium exchanger
NFT	neurofibrillary tangle
NMDA	N-methyl-D-aspartate

P

PET	Positron emission tomography
PIB	Pittsburgh compound B
PMCA	plasma membrane calcium ATPase
PSD95	post-synaptic density-95
PSEN	presenilin
P2A	Porcine Teschovirus-1

R

RCN	Rat Cortical Neurons
RNA	Ribonucleic acid
ROI	region of interest
RRE	rev-response element
rtTA	reverse tetracycline transactivator

S

SCAPE	Swept Confocally-Aligned Planar Excitation
sdChR	*Scherffelia dubia* Channelrhodopsin
s.e.m	standard error of the mean
SNR	Signal-to-noise ratio

T

T2A	Thosea asigna virus
TE	Transfer entropy

V

VGCCs	voltage-gated calcium channels
VSV-G	Vesicular Stomatitis Virus

Numbers

2D	two-dimensional
3D	three-dimensional

Chapter 1 - Introduction

Chapter 1 - Introduction

1.1 Neuronal activity

Our brain is composed of billions of neurons connected to form neural circuits. Even though most neurons share the same cellular components, these cells are highly specialized [5]. They differ in size, shape and function. Neurons consist of a soma that contains a nucleus, a smooth and rough endoplasmic reticulum, the Golgi apparatus, mitochondria, and other normal cellular components [5]. Additionally, neurons are composed of unique structures responsible for neuronal communication such as dendrites, axons and synapses. Dendrites are tree-like structures that allow the reception of signals from other neurons at specialized junctions called synapses. An axon is a structure that propagates the integrated signal to axon terminals. Santiago Ramón y Cajal was the first to envision the neuron as an individual functional unit, polarized such that signals are received through its dendrites and transmitted through its axonal process [6]. Additionally, he suggested that although an axon terminates adjacent to a dendrite of the next neuron, the cleft between them would act as a synaptic switch regulating information flow through neural circuits. Chemicals released at axon terminals, called neurotransmitters, allow signals to be transmitted from one neuron to another [7]. The neuron transmitting the signal is called the presynaptic neuron, and the neuron receiving the signal is called the postsynaptic neuron. To understand how neurons are able to communicate, it is necessary to first describe the role of their excitable membrane in the generation of these signals.

1.1.1 Excitable membrane and action potential

Neurons are surrounded by a charged cellular membrane impermeable to charged molecules or ions. The steady state of a neuron is characterised by a resting membrane potential of approximately -70 mV [8]. This membrane potential is defined by the difference in total charges between the inside and outside of the neuron and changes in response to stimuli. Following a stimulus, voltage-gated ion channels present on the membrane, change their conformation thus allowing ions to flow through the membrane down their concentration gradient [8]. When the input is strong enough, it results in an action potential (AP). The formation of an AP can be divided in several steps where the opening of the sodium channels allows positive ions to enter the neuron and results in a depolarization of the membrane to its threshold potential (-55 mV) (*Figure 1)* [8]. Once the threshold potential is reached, the neuron completely depolarizes to a membrane potential of about +30/40 mV called the peak action potential (*Figure 1).* Once the depolarization is complete, the sodium channels close while the potassium channels open allowing K^+ to leave the neuron resulting in its repolarization. This repolarization allows the membrane potential to become negative again, leading to the hyperpolarization of the neuron at first and then the restoration of the resting potential (*Figure 1)* [8].

Consequently, for a successful transmission, the action potential must travel along the axon and reach the axon terminals. When an action potential reaches the axon terminal of the presynaptic neuron, it depolarizes the membrane resulting in the opening of voltage-gated sodium channels [7]. Consequently, Na^+ ions flow inside the cell to further

depolarize the presynaptic membrane. This depolarization causes the opening of voltage-gated calcium channels thus enabling the flow of calcium ions inside the cell initiating a signalling cascade and so synaptic transmission (*Figure 2*) [7].

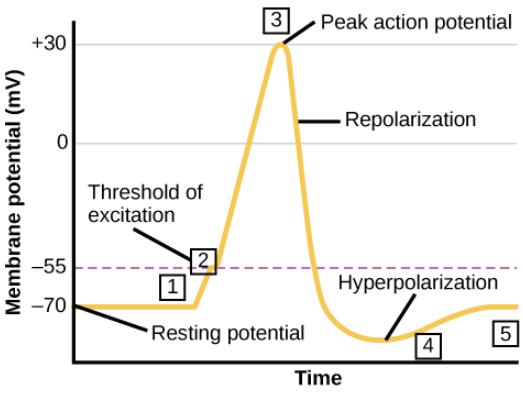

Figure 1 - The formation of an action potential. (1) A stimulus causes the depolarization of the neuron. (2) If the threshold of excitation is reached, all voltage-gated sodium channels open and the membrane depolarizes. (3) At the peak action potential, sodium channels close while potassium channels open. (4) The membrane becomes hyperpolarized as K^+ ions continue to leave the cell. The hyperpolarized membrane is in a refractory period and cannot fire. (5) The K^+ channels close and the Na^+/K^+ transporter restores the resting potential. Image adapted from **[8].**

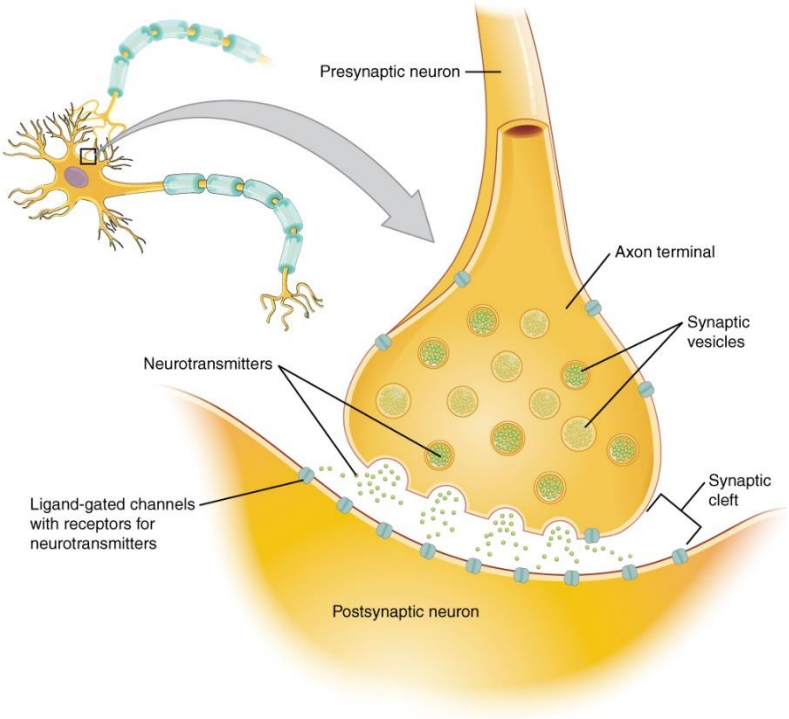

Figure 2 - Synaptic transmission The depolarization of the presynaptic membrane results in the opening of the voltage-gated calcium channels thus allowing calcium ions to enter the neuron. The calcium entry causes synaptic vesicles to fuse with the membrane and release neurotransmitter molecules into the synaptic cleft. The neurotransmitter diffuses across the synaptic cleft and binds to ligand-gated ion channels in the postsynaptic membrane, resulting in a localized depolarization or hyperpolarization of the postsynaptic neuron. Image adapted from **[7].**

1.1.2 Neuronal calcium signalling

Calcium is an essential intracellular messenger in mammalian neurons which participates in the transmission of the depolarizing signal and contributes to synaptic activity [9]. At rest, most neurons have an intracellular calcium concentration of about 50–100 nM which is determined by the balance between calcium influx and efflux and the exchange of calcium within intracellular stores [9]. Neuronal excitation results in a transient rise of the calcium in the cytoplasm. This calcium influx into neurons involves multiple mechanisms including voltage-gated calcium channels (VGCCs) and ionotropic glutamate receptors [10]. The VGCCs are categorised based on their threshold of voltage-dependent activation. They are divided into two main categories: the high- (HVA) and low-voltage-activated (LVA) channels and into subgroups called L-, P/Q-, R-, and N-type calcium channels based on their biophysical and pharmacological properties [11]. Consequently, they are present in various types of neurons and cellular structures. For example, it has been shown that the T-type LVA channels are highly expressed in thalamic neurons [12], while P-type channels are highly abundant in cerebellar Purkinje neurons [13]. In contrast, L-type and R-type VGCCs have been found in abundance in dendritic spines of pyramidal neurons [14], while P/Q- and N-type channels are found in many nerve terminals [11]. Additionally, it has been shown that VGCCs are activated by back-propagation of action potentials [15] and by synaptically mediated depolarization of dendritic spines [16]. In addition to the calcium flowing through the VGCCs, the ionotropic glutamate receptors N-methyl-D-aspartate (NMDA) receptors mediate a major part of the postsynaptic calcium influx in the dendritic spines of various neuronal cell types. This mechanism is particularly important for the long-term modification of

synaptic strength and has been demonstrated in hippocampal neurons and cortical neurons [17]. NMDA receptors are nonspecific cation channels that are permeable for sodium, potassium, and calcium ions which represent 6-12% of the total cation current [18]. The specific properties of NMDA receptors are determined by several factors including their phosphorylation status and the membrane potential of the neuron. An increased phosphorylation enhances the permeability of the NMDA receptors whereas the de-phosphorylation decreases it [19]. At resting membrane potential, NMDA receptors are blocked by magnesium which can be expelled with neuronal depolarization resulting in an increase of ionic current trough the NMDA receptors [20]. Like the NMDA receptors, another ionotropic glutamate receptors called α-Amino-3-hydroxy-5-methyl-4-isoxazole Propionic-Acid Receptors (AMPA) receptors reside postsynaptically [21]. These calcium-permeable receptors play an important role in mediating fast excitatory neurotransmission and are selectively recruited during activity-dependent plasticity to increase synaptic strength [21]. In addition to the calcium influx, calcium is released from intracellular stores such as the endoplasmic reticulum and intracellular channels. While this mechanism contributes to the elevation of the cytosolic calcium, the calcium concentration is controlled by the buffering action of cytosolic calcium-binding proteins and by its uptake and release by the mitochondria via the sodium-calcium exchanger (NCX) and the plasma membrane calcium ATPase (PMCA) [22]. Importantly, calcium plays a crucial role in the function and structure of neural circuits in the brain. Calcium signalling regulates multiple neuronal functions, such as neuronal growth, exocytosis, synaptic plasticity and cognitive function [23, 24]. A number of studies have demonstrated that disturbances in intracellular calcium

homeostasis can affect the neuron normal function and structure contributing to the memory loss and cognitive dysfunction in Alzheimer's disease [25, 26].

1.1.3 Connectivity and Network

One of the most complex aspect of the human brain resides in the interconnectivity of neural processing elements. Neural connectivity plays a crucial role in neural function and can be described at several levels including brain regions, neural networks connecting neuronal populations and finally individual synaptic connections that link individual neurons [27]. Moreover, neural connectivity refers to anatomical, functional or effective connectivity which respectively refer to a pattern of anatomical links, statistical dependencies or causal interactions between distinct units within a nervous system [27]. These units can be defined as brain regions, neuronal populations or individual neurons. Networks formed by physical connections, such as synapses linking neurons, are characterised by an anatomical connectivity. This connectivity is associated with structural biophysical parameters such as synaptic strength or effectiveness which are relatively stable at minute-timescale and subject to morphological changes over hours [27]. In contrast, functional connectivity is considered as a statistical concept focusing on the deviations from statistical independence between spatially distributed neurons which can be estimated by measuring correlations, spectral coherence or phase-locking [28]. Moreover, functional connectivity is described as highly time-dependent with statistical patterns between neurons varying on milliseconds to second-timescale. However, functional connectivity does not reflect the directional effects of the correlations between neurons. Therefore, the study of a neural networks and the effects of one neuron over another would require a combination of structural and

functional connectivity [27]. This connectivity is called effective connectivity where causal effects can be inferred through systematic perturbations of the system or through a time series analysis. Therefore, a possible way to extract the effective connectivity would be to focus on the application of time series causality measures such as Granger causality or transfer entropy [29]. The investigation of connectivity is crucial to understand how neurons and neural networks process information and how this is affected in neurodegenerative diseases such as Alzheimer's disease. Studies have shown that the dismantling of synapses and neural networks were associated with the accumulation of pathogenic Aβ assemblies in Alzheimer's disease [30]. Additionally, *in vitro* and *in vivo* studies provide evidence that Aβ oligomers reduce glutamatergic synaptic transmission by decreasing the number of surface α-amino-3-hydroxy-5-methyl-4-isoxazolepropionic acid (AMPA) and N-methyl-D-aspartate (NMDA) receptors [31]. These receptors play a crucial role in excitatory synaptic transmission and have been associated with a collapse of glutamatergic dendritic spines in Alzheimer's disease [30]. Taking these findings into consideration, studying neural networks in Alzheimer's disease may reveal key aspects of these mechanisms at a network level.

1.2 Alzheimer's disease

Alzheimer's disease (AD), the most common neurodegenerative disorder is characterised by a severe and progressive loss of cognitive function. The symptoms include memory loss, confusion about the location of familiar places and abnormalities in language. The brain regions affected by AD are the cerebral cortex and the hippocampus, areas also involved in memory formation and processing [32]. The

neuropathology of Alzheimer's disease consists of amyloid-β (Aβ) plaques and neurofibrillary tangles (NFTs) respectively composed of Aβ peptide and microtubule-associated tau protein [33]. The causative relationship between these mechanisms is unclear [34]. The early stages of the disease are marked by the loss of basal forebrain cholinergic and glutamatergic neurons while GABAergic and other neuronal cell types are affected at the end-stage of the disease [35]. Studies on AD suggest that the early-stages of the neurodegenerative process involves synaptic dysfunction [36] and precedes neuronal loss and clinical symptoms such as cognitive impairment by many years [37].

The Mini Mental State Exam (MMSE) is commonly used by clinicians to assess the disease progression and severity. This test relies on a series of questions and tests of memory attention and language [38]. Additionally, neuroimaging techniques have contributed to gather information on the brain changes underlying the symptoms of AD. These techniques include magnetic resonance imaging (MRI) which enables the visualization of grey matter, white matter and cerebrospinal fluid. Positron emission tomography (PET) is also used with various tracers such as 18F-2fluoro-2-deoxy-D-glucose (FDG) in a technique called FDG-PET which helps identify loss of brain mass and reduction in the glucose metabolic rate. Additionally, the accumulation of Aβ plaques can be detected using Pittsburgh compound B (PIB) in a technique called PiB-PET [39]. AD is categorised under two main forms: the early-onset familial AD and the late-onset sporadic AD [40]. Familial and sporadic forms of AD exhibit different aetiology while presenting the same hallmarks and symptoms of memory loss and confusion. There is

currently no definitive diagnosis for AD and the identification of late-onset sporadic AD is difficult, due to similarities with normal healthy aging [41].

1.2.1 Familial and sporadic Alzheimer's disease

The familial form is described by classic Mendelian inheritance to occur in an autosomal-dominant manner [42]. It represents less than 5% of disease burden and it is caused by mutations in three different genes: amyloid precursor protein APP, presenilin PSEN1 and presenilin PSEN2 [43, 44]. Multiple mutations in APP have been found including the London mutation APPV717I, one of the most common APP mutation worldwide [45] originally identified in an English family in 1991 [46, 47] which affects the γ-secretase cleavage site [48]. Several models have been used to characterize this mutation. Studies post-mortem have shown elevated Aβ42 levels relative to total Aβ in the brain plasma and lysates of patients carrying the mutation APPV717I [49]. In primary mouse neurons, this mutation resulted in an increase of the Aβ42/Aβ40 ratio caused by high levels of Aβ42 [50, 51]. The two most abundant alloforms of this peptide co-exist under normal physiological conditions in the brain in an Aβ42/Aβ40 ratio of ∼1:9. This ratio is often shifted to a higher percentage of Aβ42 in brains of patients with familial AD and this has recently been shown to lead to increased synaptotoxicity [52]. This finding has also been observed in brain lysates from transgenic mice expressing human APPV717I [53] and neurons generated from induced pluripotent stem cells (iPSCs) derived from the skin fibroblasts of mutation carriers [1]. In most studies, the increased ratio of Aβ42/40 is mainly attributable to an increase in Aβ42 with no change or little effect on Aβ40 levels. In addition to the increased Aβ42 levels, the V717I mutation in the iPSCs derived

neurons showed altered APP subcellular localization and tau expression and phosphorylation [1].

Interestingly, another recently identified APP mutation (A673V) stands out from all the genetic defects previously reported in the APP, PSEN1 and PSEN2 genes [54]. A673V is the first AD-associated mutation with a recessive Mendelian trait of inheritance. It is associated with the early-onset of AD in homozygous individuals, whereas heterozygous carriers are unaffected. This mutation consists of a C-to-T transition that results in an alanine-to-valine substitution at position 673 (APP770 numbering) corresponding to position 2 of the Aβ sequence. *In vitro* studies showed that the A673V mutation shifts APP processing towards the amyloidogenic pathway with increased production of Aβ peptides. Additionally, this mutation resulted in an aggregation and fibrillogenic properties of Aβ1–40 and Aβ1–42. However, the interaction of mutated and wild-type Aβ species inhibits Aβ folding, consistent with the observation that the A673V heterozygous carriers do not develop the disease [55]. The identification of a mutated Aβ sequence which acts in a dominant-negative fashion on amyloidogenesis has important implications for the development of a novel therapy for both sporadic and familial forms of AD.

The late-onset sporadic form is the most clinically observed cases of Alzheimer's disease in patients over 60 years age [56]. Its development seems to involve a genetically complex pattern of inheritance in which life exposure events, environmental factors and genetic risk factors seem to play an important role [57]. Genetic risk factors associated with the APOE gene have been identified in AD patients. This gene has three alleles (ε2,

ε3 and ε4) and encodes for a lipid transport protein called apolipoprotein E [58]. Studies on the APOE gene have identified the prevalence of the allele ε4 in AD patients [59]. This investigation has shown that the APOE-ε3/ε3 genotype was the most common in the control group whereas the genotype APOE-ε3/ε4 or APOE-ε4/ε4) were found in AD patients. These findings led to the conclusion that carriers of the APOE-ε4 allele were at a greater risk to developing AD than non-carriers [59]. The genetic risk linked to APOE-ε4 and AD resided in the fact that APOE isoforms bind to amyloid β peptides. It has been shown that APOE3 has greater affinity than APOE4 for both Aβ1-40 and Aβ1-42 [60]. The binding efficiency correlating inversely with the risk of developing late-onset AD, these results suggest a possible involvement of APOE3 in the clearance of Aβ from the central nervous system which would correlate with the build-up of Aβ in homozygote carriers of the APOE-e4 allele [60].

Although Aβ peptides of varying length are produced, Aβ1-42 has two additional hydrophobic residues at the C-terminus and readily assembles into soluble oligomers. Amyloid-β oligomers are linked to synaptotoxicity and progressive cognitive decline in AD [61] and Aβ1-42 is considered to be comparatively more amyloidogenic. Moreover, studies have suggested that Aβ monomers and plaque cores were largely inactive whereas oligomeric Aβ may be responsible for synaptic dysfunction and that oligomeric Aβ elevation and synaptic loss may indicate the severity of cognitive impairment in AD patients [62, 63]. Therefore, studying the synaptic dysfunction in AD may reveal the key characteristics of the early disease mechanisms [64].

1.2.2 Synaptic dysfunction

Although these mechanisms are still not fully understood, it has been shown that elevated levels of Aβ oligomers affect glutamatergic neurotransmission [65]. The accumulation of Aβ within neurons has been shown to disrupt axonal transport and synaptic function, resulting in alterations in protein expression and apoptosis. These observations correlate with the neurotoxicity and neuronal death resulting in the loss of memory in the late stage of AD. Further studies on the cortex of mild cognitive impairment (MCI) or very mild AD patients have demonstrated a significant decrease in synaptophysin immunoreactivity relative to age-matched subjects with normal memory function [66]. A decrease in synaptophysin immunoreactivity in presynaptic terminals together with an increase in Aβ42 was also observed in a transgenic mouse model expressing human wild-type APP [67]. Additionally, more recent studies on post-mortem frontal cortex samples from control and AD patients have correlated high levels of Aβ oligomers with a decrease in the postsynaptic protein, post-synaptic density-95 (PSD95) [68]. Various studies using direct exposure to Aβ oligomers, which has been linked to neuronal loss and neuronal network disruption in AD, confirm these observations [61, 62]. Moreover, it has been shown that intra-axonal oligomeric Aβ42, but not Aβ40 nor extracellular Aβ42, acutely inhibited synaptic transmission [69]. Therefore, the induction of Alzheimer's disease-related neuropathy based on high concentrations of soluble amyloid β oligomers or overexpression of APP constructs, that produce Aβ at high local concentrations, may not fully mimic the disease mechanisms in AD patients. In contrast, induced Pluripotent Stem Cells (iPSC) technology by using somatic cells from patients

might represent a more accurate model to study synaptic transmission early stages of AD.

1.2.3 Opportunities and Limitations of Modelling Alzheimer's disease with iPSC.

Understanding the mechanisms that underlie a pathology may help to target the causes of a particular disease. Although research has shown impressive advances in analysing these mechanisms and developing new therapies, numerous disorders such as Alzheimer's disease remain with no established methods of treating the underlying cause [70]. Genetically engineered animal models have contributed to our progress allowing testing of different therapeutic strategies but the construction of models that can accurately recapitulate a human pathology remains challenging. Due to species differences, there is a debate as to whether these systems are reliable and fully reflect the key aspects of a human disease [71]. This could explain why treatments that have been developed using animal models are not always effective when transferred to humans and why all clinical trials for the Alzheimer's disease have so far dramatically failed [70]. An alternative modelling strategy may be to use *in vitro* studies on *ex-vivo* tissue but the complexity of the nervous system and the lack of accessibility to human brain biopsies makes it unfeasible [72]. Thus most of the human studies on Alzheimer's disease have been performed on post-mortem tissues, a model that has severe limitations particularly because it represents the end-stage of the disease which limits its potential rise towards a better understanding of disease mechanisms [73]. A major issue of studying Alzheimer's disease and developing new drugs resides in the fact that human disease models are not available. However, a novel technology that offers an

unprecedented way to model a disease *in vitro* has recently emerged. By reprogramming somatic cells into a state similar to embryonic stem cell, the iPSC technology represents a promising tool to overcome the limitations of the disease models described above [73].

Takahashi and Yamanaka's laboratory first established induced pluripotent stem cells from mouse fibroblasts in 2006 [74]. Amazingly, these cells present similar properties to that of embryonic stem cells in terms of morphology, gene expression profile, self-renewal capacity, and pluripotency [75]. Human induced pluripotent stem cells were generated by the co-expression of four genes: Oct4, Sox2, Klf4 and c-Myc [76-78]. These transcriptions factors called the "Yamanaka factors" are naturally expressed in embryonic stem cells but not in differentiated cells such as fibroblasts. During the differentiation process, the expression of these genes is silenced, and another set of genes starts to be expressed which leads the differentiation of stem cells into specialised cells. Reprogramming and differentiation of somatic cells from patients into disease-relevant cell types [79] naturally opened new avenues for disease modelling [80] especially in neuroscience [81]. A wide range of disease-specific iPSC have been recently established from patients with neurodegenerative diseases. Somatic cells from patients with amyotrophic lateral sclerosis [82], Parkinson's disease [83, 84] and Alzheimer's disease [1, 85] have been successfully reprogrammed into iPSC and differentiated into disease-relevant cell types. Indeed, this infinite source of human cells carrying the genetic variations related to the disease development [86], allow new ways to study neurodegenerative diseases. In most studies of iPSC models for Alzheimer's disease, neuronal differentiation protocols are used to generate glutamatergic cortical forebrain neurons [87-89]. However, after several weeks, these cultures still consist of a mixture

of different cell types and maturity. Despite these facts, studies of iPSC for Alzheimer's disease have shown an accumulation of amyloid β [89] in Alzheimer's iPSC-derived neurons from familial Alzheimer's disease patients and more recently, also in iPSC-derived neurons from sporadic Alzheimer's disease patients [85]. In an interesting experiment, iPSC-derived neurons from two different sporadic patients have been treated with docosahexaenoic acid, an omega-3 fatty acid abundant in the central nervous system and a main constituent of the neuron's plasma membrane [90]. This treatment resulted in an amelioration of the stress response was observed in one of the cultures but not the other [88]. These recent studies reveal the remarkable capacity of these cells to be used as a disease model but also stress the potential variability in iPSC models. Additionally, three-dimensional (3D) models [91] and 3D human triculture systems consisting of co-cultures of neurons, astrocytes and microglia have been established to facilitate the development of more precise human neural cell models of Alzheimer's disease [92]. In these studies, the FAD mutations in the APP and PSEN1 genes were able to induce robust extracellular deposition of Aβ, including β-amyloid plaques, in a human neural stem cell-derived 3D culture system.

Before the iPSC technology had become available, studying Alzheimer's disease was challenging due to the lack of appropriate models as previously underlined. Although the generation of iPSC from patients is possible and has opened new ways to model Alzheimer's disease, the interpretation of the results remains challenging. This may results from the complexity of the mechanisms of neurodegeneration and also from the typical timescale of late-onset diseases measure in decades [93]. Various approaches such as a prolonged culture [94], treatment with progerin [95] and oxidative stressors

[96] have been investigated to mimic the ageing process *in vitro*. Furthermore, the extent of neuronal maturation also plays an essential role in the formation of functional synapses and synaptic plasticity [97]. This might constitute a challenge regarding the neuronal differentiation in iPSC-derived neurons compared to the natural neuronal development.

1.3 Tools to investigate neuronal activity

1.3.1 Patch-clamp electrophysiology and Multi-electrode arrays (MEAs)

Our brain is composed of billions of neurons connected to form neural circuits which encode information in electrical events called action potentials. Hodgkin and Huxley first described in 1952 the sodium current that triggers the initiation of action potentials across the neuronal membrane through voltage-gated sodium channels [98]. Positively charged ions flow through these channels into the neuron resulting in the depolarization of the neuron. Once a certain threshold is reached, the neuron can fire an AP called a spike. Recordings of currents or voltage transients can therefore give us insight into neuronal function [99]. These measurements can be achieved by inserting a glass pipette containing the electrode into the cellular membrane [100-102]. In the voltage clamp configuration, a holding voltage is set while measuring the current flowing through ion channels across the membrane [100]. In the current clamp configuration, a steady current is maintained to assess the voltage output. Current-clamp is commonly used to investigate the resting membrane and synaptic potentials, while voltage-clamp is best-suited to study the neuron firing activity [103]. Various protocols can be applied

such as a steps of injected current to determine the AP firing pattern at different current levels or a ramp of increasing current to determine the AP threshold [99, 104].

While electrophysiology enables the study of the functional output of single neurons [101, 105], this technique exhibits several limitations such as its invasiveness due to the physical contact established with the neuron thus impairing long term interrogation of neurons [104, 106]. Additionally, this "gold-standard" technique exhibits limitations when one wishes to characterise a highly heterogeneous neuronal population. Another limitation is the low throughput that can be achieved [105] as only a limited number of cells can be studied at the same time. Moreover, the use of an electrode renders the patch clamping technique technically demanding and labour intensive [101]. A non-invasive technique enabling interrogation of multiple cells simultaneously would overcome these limitations by increasing the number of cells studied, duration of the experiment and cellular viability thus opening new avenues to the study of neural networks [106, 107].

Novel technologies such as multi- or microelectrode arrays (MEAs) have been developed as a means to improve the throughput [108-110]. These devices are composed of multiple extracellular electrodes to simultaneously stimulate and record from an ensemble of neurons thus enabling the study of neural networks *in vitro*, brain slices and *in vivo* [108, 111, 112]. The extracellular electrodes allow characterization of single neurons by triangulating the signal through multiple recording points [108, 110]. Despite overcoming the limitations described above, MEAs exhibit a prominent drawback. While enabling the stimulation and recording from multiple neurons simultaneously, it is

difficult to determine the origin of the electric signals [108, 110]. Moreover, while MEAs overcome the low throughput issue in terms of number of cells analysed at the same time, applying this technique in high throughput screening studies remains challenging as multiple devices might be required to analyse neurons cultured/treated in/with different conditions.

1.3.2 Optogenetics

Optogenetics, a novel technique developed by Karl Deisseroth and his team may overcome these limitations [113]. By combining optic and genetic techniques, it allows light-mediated control of neural activity [114, 115]. This innovative approach introduces a microbial opsin gene that encodes light-activated channels to be expressed within specific neuronal populations. This technique consists in the excitation or inhibition through targeted illumination with high temporal precision [113, 116, 117]. Several families of opsins have been discovered and further engineered including bacteriorhodopsin [118], halorhodopsin [119] and channelrhodopsin (ChR) [120]. Optogenetic tools have generated a strong interest as it comes with multiple advantages [101, 115, 121]. First, this technology opens new avenues in neuroscience by overcoming the invasiveness of patch clamping with the use of opsins activated by specific wavelength of light [117, 122]. Moreover, by avoiding physical contact, it does not impact the cell viability while reducing the labour intensity and the need for technical skills training [101]. Additionally, this technique has demonstrated its potential use for network studies by enabling the activation of multiple neurons simultaneously [101, 114, 123]. Another significant advantage of this technique is the use of genetic

encoded proteins. Therefore, the optogenetics actuators can be engineered not only to facilitate their trafficking towards the cell membrane [124] but also to target specific cell types via transfection and the use of promoters [114, 115, 121]. Up to this day, the most commonly used and characterised optogenetic actuators are ChR derived actuators [113, 116, 125-127]. Channelrhodopsin-1 (ChR1) and Channelrhodopsin-2 (ChR2) were originally characterised as light-gated ion channel driving phototaxis in the green alga *Chlamydomonas reinhardtii* [120, 128]. These light-gated ion channels belong to a family of fast light-sensitive proteins found in prokaryotes, fungi and algae called microbial type I opsin group [121, 129]. Type I opsins consist of seven transmembrane helices forming the channel pore and contain the light-sensitive chromophore all-*trans*-retinal [121, 123, 126, 127, 129]. This chromophore is covalently bonded to the rest of the protein and changes its conformation to 13-*cis*-retinal in reaction to photon absorption. This change of conformation induces a depolarization resulting in the opening of the pore to allow non-specific cation influx of H^+, Na^+ and Ca^{2+}, but is also permeable to K^+ [126, 130]. This capability plays an important role regarding the speed and spectral properties of the light-gated ion channels [126, 129].

ChR2 for example has been shown to have an augmented rate of expression in mammalian neurons with a blue-shifted spectrum compared to ChR1 [127, 129, 131]. ChR2 has been shown to reliably evoke action potentials up to 40 Hz in mammalian cells [113] (*Table 1*). However, at higher frequencies, the evoked activity has been demonstrated to be less reliable in terms of spike fidelity [131-133]. The spike fidelity is linked to the opening and closing kinetics of the channel. ChR2 is relatively fast however its closing kinetics $\tau_{off=}$~10 ms is slower than a single AP [99, 134] (*Table 1*). This limitation

becomes critical for studies involving the auditory system in which neurons can fire at higher frequencies [135] or to achieve temporally precise manipulation of membrane potentials [136]. Another crucial aspect is the conductance which directly determines the effectiveness of the light-induced depolarisation [134]. Single channel conductance of ChR2 is below 1 picosiemens which is less than the conductance of the common membrane channels [120, 137]. ChRs exhibit additional limitations such as poor trafficking resulting in differences in expression levels or intracellular aggregation thus reducing their effectiveness of membrane depolarisation [131, 138]. Another significant limitation resides in the desensitisation which reduces the consistency of depolarisation [120]. In fact, the response of ChR2 decays of 80% from a peak response to a steady-state level response under continuous or repeated illumination exposure [120]. In addition, it is essential to focus on the development of opsins with the capability to generate a robust response at low light intensities to achieve spatial and temporal manipulation of multiple cells as this requires a higher energy light source [134, 138]. Lastly, the excitation spectrum of ChR2 restricts its use in combination with other optogenetic tools which can be overcome with the development of red-shifted opsins. This would enable a wider range of experiments while reducing the light-scattering and tissue damage through phototoxicity [125, 131, 132]. Efforts have been made towards the development of opsins addressing the limitations previously described [134]. Photocurrents and light sensitivity have been improved with the alteration of a single amino acid to create ChR2-H134R, however, this mutation had a negative effect on the kinetic of the channel [131, 139]. In contrast, the kinetics has been improved to support frequencies up to 200 Hz with the creation of ChETA (E123T), however, the later

appeared to display strong light desensitization and reduced photocurrent [131, 133] (*Table 1*). A consensus was found between the speed of the kinetics and light sensitivity with creation of a double mutant (E123T/T159C) which enabled reliable and sustained optical stimulation of hippocampal pyramidal neurons up to 60 Hz with good photocurrents [140].

Improvements of ChRs include ChIEF, an opsin based on a chimera of ChR1 and ChR2 named ChEF with an additional point mutation of Ile^{170} to Val. ChiEF exhibited increased channel closure rate compared to ChR2 and ChEF however, the introduction of I170V into ChEF reduced the sensitivity to light of ChiEF [137] (*Table 1*). Further improvements have given rise to the blue-light activated opsin Chronos, characterized as the fastest blue light-activated ChR available [141]. Moreover, research to improve the photocurrent has resulted in the discovery of four previously unknown channelrhodopsins from the species *Chloromonas oogama* (CoChR), *Chloromonas subdivisa* (CsChR), *Stigeoclonium helveticum* (ShChR) and Scherffelia dubia (SdChR) that bore either significantly higher blue photocurrents than ChR2 or significantly higher green photocurrents than $C1V1_{TT}$ [141]. $C1V1_{TT}$ belongs to the C1V1 variants exhibiting a redshifted peak of their absorption spectrum (λ=560nm) (*Table 1*). The development of a wide range of spectral selectivity is particularly important as a means to achieve independent optical excitation of distinct populations [141] or the use of opsins in conjunction with indicators of activity to enable all-optical systems [142]. In addition to the previously mentioned C1V1 variants, ReaChR has been designed to be activated under orange to red light (λ= ∼590nm) [143], Chrimson channelrhodopsin and his mutant ChrimsonR with augmented kinetics have been developed and characterised as

the more red-shifted opsins with a peak activation at 625 nm [141] (*Table 1*). Additionally, CheRiff was based on SdChR and designed with the mutation E154A which sped its kinetics and shifted the peak of the action spectrum to λ_{max} = 460 nm to enable an all-optical electrophysiology in mammalian neurons [142] (*Table 1*).

While optogenetics provides a powerful tool for studying neural function, as with any new technology, its limitations are slowly emerging: the poor trafficking resulting in intracellular aggregation reduces the effectiveness of membrane depolarisation and may cause toxicity over time [131, 138]; the light stimulation parameters (e.g. stimulation duration, frequency, and intensity) must be chosen carefully in order to avoid non-physiologic patterns of activity [144]. Additionally, although light has desirable properties it may potentially induce over-heating in tissue resulting in damages. In summary, ChRs are constantly being developed to improve particular features, however it seems that this generally results in a trade-off of some kind [125]. In conclusion, the advantages and limitations of optogenetics have to be carefully taken into consideration and the choice of the ChRs to be used depends on the application [131].

Opsin variant	**Activation Wavelength**	**Max. photo current (pA)**	**Speed (ms)**		Max. frequency (Hz)	Sources
			τ_{on}	τ_{off}		
ChR2	~ 470 nm	500 - ~ 1000	0.2 - 1.21	13.5	40	[113, 131, 138, 145]
ChETA (E123T)	~ 490 nm	645	0.86	7.9-8.5 4.4-5.2	200	[124, 131, 133]
ChiEF	~ 450 nm	~ 1400	1.618 -2.79	~12	50	[131, 134, 137]
CheRiff	~ 460 nm	2030	4.5	16	~ 60	[107]
Chronos	~ 500 nm	~ 1000	2.3	3.6	>60	[135, 146]
C1V1$_{TT}$	~ 540 nm	1072	-	34	10	[124, 134, 136]
ReaChR	~ 590 nm	~ 1250	68.1 - 100	137.2	10	[143]
Chrimson	~ 590 nm	674	~7	21.4	10	[146]
ChrimsonR	~ 590 nm	-	-	15.8	<20	[146]

Table 1 - Properties of selected depolarizing opsins. An overview of both fast and red-shifted ChRs, listed with parameters relevant for this project. Maximal photocurrent describes the reported peak of current mediated through the variant in pA. Light sensitivity is reported in mW/mm^2, calculated from light power needed for half maximum activation for peak and steady state responses. Speed of the channel kinetics is given in the rate of activation τ_{on} and deactivation τ_{off} in ms. The maximal firing frequency (Hz) is the highest frequency supported reliably by the channel, as reported in the sources. As this table is compiled from the literature, some parameters may be listed as intervals due to disparate reports.

1.3.3 Fluorescent reporters of electrical activity

The electrical potential across the plasma membrane of neurons is a key information carrier in the brain [147]. Therefore, monitoring the voltage dynamics of individual neurons is critical for understanding neuronal function. As previously mentioned, although electrophysiological methods for monitoring voltage have been successfully used for several decades (e.g. patch clamping), optical monitoring of voltage can overcome the invasiveness of the electrophysiology. Additionally, optical imaging can allow higher spatial resolution and recording from multiple neurons simultaneously. Optical methods have been developed to report the change in transmembrane voltage such as voltage-sensitive dyes (VSDs) and genetically encoded voltage indicators (GEVIs) [148, 149]. They are characterised by several features such as their brightness, kinetics, excitation and emission spectrum and signal-to-noise ratio (SNR) [150].

1.2.3.1 Voltage-sensitive dyes

The development and improvement of the voltage-sensitive dyes (VSDs) began in the 1970s. This line of work extends now for several decades, starting with invertebrate preparations, and has used chromophores for both absorption and emission [151, 152]. The VSDs shift their absorption or emission fluorescence based on the membrane potential thus enabling the visualization in real time of neuronal activity [153]. Unlike extracellular electrophysiology techniques, these dyes allow activity measurements in large populations of neurons simultaneously with high spatial resolution and millisecond temporal resolution [149]. With such resolutions, the use of voltage-sensitive dyes appears to enable the study of neural networks dynamics [153]. However, despite offering a large range of spectral properties and good SNR [107, 154-156], this technique

does not allow cell-specific targeting. In addition of being challenging to implement, the use of dyes can induce toxicity and cannot be used over prolonged periods of time which impairs long-term studies [157, 158]. In contrast, genetically encoded voltage indicators can be stably expressed to study how neuronal dynamics evolve over time while allowing selective sampling of neuronal subsets in heterogeneous populations with the use of genetic labelling [159, 160].

1.2.3.2 Genetically encoded voltage indicators: opportunities and challenges

Genetically encoded voltage indicators (GEVIs) are light-emitting protein-based sensors sensitive to changes in neuronal voltage. They typically change brightness in response to changes in membrane potential. They have been developed to overcome the limitations of the traditional electrophysiology and voltage-sensitive dyes. These two techniques exhibit significant drawbacks such as their invasiveness, toxicity and non-specificity [161]. Indeed, the need of selective labelling of specific cell types motivated the development of GEVIs. In fact, GEVIs can be stably expressed to study how neuronal dynamics evolve over time while allowing selective sampling of neuronal subsets in heterogeneous populations with the use of genetic labelling of specific neurons [159, 160]. However, in order to compete with traditional electrophysiology, GEVIs must have the kinetics to match or surpass those of the transients they are reporting with sufficiently low SNR [158]. Efforts towards the development of GEVIs started three decades ago with the design of the first GEVI called Fluorescent Shaker (FlaSh) designed with the gene fusion of GFP and the Shaker potassium channel that changes fluorescence emission in response to changes in membrane potential [162]. Additionally, the introduction of a W434F mutation prevented ions to flow through the pore while

maintaining voltage-dependent rearrangements [162]. Despite exhibiting a strong signal, its kinetics is rather slow (τ_{-on} ~ 100 ms; τ_{-off} ~ 60 ms) however, a strategy consisting of the replacement of GFP with several different fluorescent proteins resulted in an improvement in the kinetics [163]. Consequently, variations of GEVIs were designed in combination with fluorescent proteins that employ fluorescence resonance energy transfer (FRET) to signal a change in voltage such as VSFP1 [164]. The use of FRET expands the capabilities of the GEVIs from single wavelength fluorescence intensity changes to dual wavelength measurements based on both voltage-dependent spectral shifts and changes in FRET [165]. However, it has been shown that the membrane localization in mammalian cells was weak [158]. Further improvements led onto the creation of various GEVIs with faster kinetics including VSFP-Butterflies [166], Accelerated Sensor of Action Potentials 1 (ASAP1) isolated from the sea squirt *Ciona intestinalis* voltage sensitive phosphatase [167] and microbial rhodopsin proton pumps such as proton Archaerhodopsin-3 (Arch) [168]. Additional mutations resulted in significantly faster arch-based sensors such as Arch-D95N, Arch-EEQ and Arch-EEN [169] and QuasArs [107]. Interestingly, one of the improvements answered the need of enabling deeper imaging with the development of near-infrared GEVIs [170]. Other improvements focused on the ability to report action potentials with high temporal fidelity and on limiting the proton pumping with QuasAr1 which excels in terms of kinetics and increasing the brightness with QuasAr2, displaying a larger fluorescent amplitude in response to voltage changes [107]. Additionally, the development of near-infrared GEVIs enabled the combination with other types of indicators and optogenetic tools. Based on this approach, QuasArs were combined to CheRiff in a combination

called the Optopatch [142]. Although, this combination has been used to investigate neuronal function, it still suffers from various limitations such as the indicator's sensitivity and the complexity of the imaging system to enable the study of multiple neurons in a single recording [142]. As a means to further increase the brightness, a strategy using FRET was adopted to increase the SNR resulting in the creation of MacQ-mOrange, MacQ-mCitrine and QuasAr2-mOrange [171, 172]. Despite these improvements, the development of GEVIs seems to balance between kinetics and brightness [158, 173]. The ideal GEVIs would exhibit fast kinetics and high SNR in order to achieve high temporal resolution [154, 156, 174]. Taking all this into account, the choice of GEVIs must be carefully done considering their limitations and the application. As the central goal of neuroscience is to understand how the nervous system encodes and processes information at circuit and cellular levels, it is crucial to enable recordings from multiple neurons simultaneously to capture neural networks dynamics [167]. Indeed, to report changes in voltage, GEVIs must be expressed in the plasma membrane resulting in less effective imaging of voltage transients in larger population of cells under low magnification [175]. Additionally, GEVIs must produce enough photons to be detected above noise on a millisecond timescale to report action potentials. Taking into account the kinetics of the indicators and the signals they are monitoring, voltage imaging has to be performed at high frame rates (e.g. 1kHz) [161]. Consequently, faster acquisitions result in fewer photons captured per frame, which can be compensated for by the increased indicator brightness or higher illumination intensity. However, higher illumination intensities can result in photobleaching and phototoxicity [156].

In conclusion, GEVIs can enable a direct and precise measure of neuronal activity; however, these studies can be performed mostly at the single cell level. The complexity of the imaging setup required to image multiple cells simultaneously limits the throughput of this technique. In contrast, as previously mentioned, the neuronal electrical activity is accompanied with a change in the calcium dynamics. Therefore, a possible strategy to increase the throughput and thus study the neuronal function at a network level consists of imaging the resulting changes in the intracellular calcium concentration [176]. Indeed, the kinetics of the calcium dynamics are slower than action potentials, and so the subsequent recordings of calcium activity requires a lower frame rate (e.g. 5-10 Hz) compared to the one necessary to image the voltage-based events (e.g. 1kHz) [176]. Therefore, calcium imaging can be performed with widely accessible wide-field fluorescence microscopes thus enabling the recording of multiple cells simultaneously [177].

1.3.4 Calcium imaging

Calcium is a secondary neuronal messenger which participates in the transmission of the depolarizing signal and contributes to synaptic transmission. Neurons typically maintain low cytoplasmic-free calcium concentration (50–100 nM) at rest [178]. Action potentials trigger a large and rapid calcium influx into the cytoplasm through channels such as voltage-gated channels or is released from calcium-loaded organelles resulting in an increase of the local calcium concentration [178]. Calcium levels then return to baseline via extrusion from the cell and reloading of intracellular buffers and stores. Additionally, the activation of neurotransmitter receptors causes calcium transients in dendritic spines during synaptic transmission. The spatiotemporal evolution of

calcium transients is shaped by the localization, mobility, affinity, and kinetics of these processes [178]. Therefore, the intracellular calcium dynamics reflects neuronal spiking and synaptic activity across populations of neurons. One of the main advantages of calcium imaging stems from the larger magnitude and slower kinetics of these events compared to action potentials. The duration of a single AP from initiation to completion varies within 3 to 5ms while the resulting calcium transient can be detected at sampling intervals of 30–60 ms [179, 180]. The development of calcium imaging focuses on two aspects: the development of calcium sensors and the development and implementation of the appropriate imaging setup. The first class of calcium indicators were bioluminescent calcium-binding photoproteins, such as aequorin. Aequorin is a monomeric calcium binding protein derived from the marine and luminescent jellyfish *Aequorea victoria* [181]. The protein is composed of three calcium-binding sites and a noncovalently bound chromophore constituted of coelenterazine and molecular oxygen [182]. Upon binding of calcium ions, light is emitted via an intramolecular reaction in which the protein undergoes a conformational change resulting in the oxidation of coelenterazine to coelenteramide. Bioluminescent recordings have the great advantage of not requiring external illumination [183]. However, since the purified aequorin, is unable to penetrate the plasma membrane of intact cells, this approach requires single cell loading with a micropipette [184]. Additionally, bioluminescent recordings of calcium signals have been shown to suffer from a low quantum yield [185]. As a means to overcome this limitation, fluorescent proteins have been fused to aequorin in a technique called bioluminescence resonance energy transfer (BRET) [186]. While displaying the advantage of avoiding phototoxicity

and photobleaching, the use of bioluminescent calcium-binding photoproteins has a significant drawback as it is technically demanding and invasive [184]. More recently, to overcome the limitation of the low tissue permeability, analogues of D-luciferin were reported such as AkaLumine that when catalysed by Fluc produces near-infrared emission peaking at 677 nm, which can penetrate most animal tissues and bodies [187].

1.3.4.1 Calcium dyes

Efforts to develop more sensitive fluorescent calcium indicators led onto the hybridization of highly calcium-selective chelators like ethylene glycol-bis(β-aminoethyl ether)-N,N,N′,N′-tetraacetic acid (EGTA) or 1,2-bis(o-aminophenoxy)ethane-N,N,N′,N′-tetraacetic acid (BAPTA) with a fluorescent chromophore [188]. This approach resulted in the design of the first generation of fluorescent calcium indicators with quin-2, fura-2, indo-1, and fluo-3. These chemical calcium indicators change their conformation upon calcium ions binding resulting in a change in the emitted fluorescence. Quin-2 excited by ultraviolet light (339 nm) has been shown to suffer from low brightness and autofluorescence [189]. In contrast, fura-2 excited at 350/380 nm and significantly brighter than quin-2, offers improved quantification of calcium activity by ratiometric method [190]. This method is enabled with the use of dual wavelength excitation resulting in a quantitative determination of the calcium concentration in a neuron of interest independently of the intracellular dye concentration [190]. During the last three decades, several other calcium indicators have been developed with a higher SNR, wide range of excitation spectra and improved calcium-affinity such as Oregon Green BAPTA and fluo-4 dye families. These dyes are not only widely used in single-cell calcium imaging for the analysis of basic mechanisms of calcium signalling in

neuroscience but also for the monitoring of activity in local populations of interconnected neurons. Several studies involving dye loading of neuronal populations in intact tissues include the analysis of the circuitry of the cortex and the hippocampus [191, 192] and the identification of synaptically connected neurons [193]. Additionally, this technique has been applied to analyse pathological forms of network activity, such as epileptiform events [194]. Multicell bolus loading (MCBL) of membrane-permeable acetoxymethyl (AM) ester calcium dyes, is a common loading technique allowing the recording at a high spatial resolution of many cells simultaneously [195, 196]. However, this technique presents important drawbacks such as a high background resulting from the lack of genetic control [195]. The genetic control is an important feature not only because it avoids unspecific staining of non-neuronal cells but also allows the targeting of specific neurons relevant to a research question. Additionally it enables long-term expression which is more suitable for chronic imaging recordings from the same cell population [197]. Two decades ago, the introduction of GECIs represented an important breakthrough [198]. The first generation of GECIs suffered from their slow kinetics and low SNR. However, there had been great progress in the recent years towards the improvement these features.

1.3.4.2 Genetically Encoded Calcium Indicators

Extensive protein engineering efforts have contributed to the success of GECIs. Efforts to match with calcium dynamics in neurons have resulted in the improvement of the GECIs intrinsic properties such as adequate expression level [199], brightness [200], high SNR [201], photostability [202], large dynamic range [201] and fast kinetics [203]. The first GECIs to gain wide usage were called Cameleons [198]. These FRET-based indicators

contain calmodulin (CaM), the calmodulin-binding peptide M13 from myosin light chain kinase (MLCK) and consist of pair fusions of a blue- or cyan-emitting mutant of GFP and an enhanced green- or yellow-emitting GFP. Upon binding of calcium, calmodulin wraps around the M13 domain, altering the overall conformation of the construct. Consequently, the GFP molecules move closer together and thereby increase the fluorescence energy transfer between them. Meanwhile, single-fluorescent protein GECIs were developed to improve the dynamic range of FRET-based indicators. These indicators are based on enhanced yellow fluorescent protein (EYFP) or circularly permuted fluorescent proteins which change fluorescence intensity upon calcium binding. Camgaroos design is based on a calmodulin fragment between a split GFP molecule [204]. In contrast, Pericams and GCaMP family indicators are designed with CaM, its binding peptide M13 and a circularly permuted green fluorescent protein [205, 206]. Upon calcium binding, CaM interacts with calmodulin-binding peptide M13 switching the protonation state of the fluorescent protein resulting in a change of fluorescence. The GCaMP family has been particularly popular and kept being developed with various modifications of the GCaMP scaffold to improve features such as brightness with GCaMP2 [207], GCaMP3 [208], increased sensitivity with GCaMP-HS [209], GCaMP5 and improved kinetics with the Fast-GCaMPs [203] and GCaMP6 series [201]. Further development including GCaMP7a and GCaMP8 did not show significant improvement compared to the GCaMP6 series [201]. However, more recently, the jGCaMP7 series (Janelia GCaMP7) has been developed with increased brightness, higher calcium affinity and faster kinetics than the GCaMP6 series [210]. Importantly, it has recently been shown that GCaMP sensors could abnormally

accumulate in the nucleus of neurons and cause multiple side-effects such as cell damages and altered neural function [211]. To overcome this limitation, GCaMP-X was recently engineered with an additional apocalmodulin (apoCaM)-binding motif and an extra tag ensuring subcellular localization [212].

Interestingly, the potential of GECIs in multiplex imaging has been greatly improved with the expansion of the colour-spectrum including the design of red-shifted variant RCaMP1 based on mRuby [213], R-GECO and R-CaMP2 based on mApple [214] (

*Table **2***). The use of red-shifted indicators comes with the advantage to reduce light scattering and phototoxicity [215]. Multi-colour imaging not only enables simultaneous assay involving distinct cell population but also allows the potential combination of GECIs with other types of indicators and optogenetic tools. Researchers have been actively improving optogenetics tools, GEVIs and GECIs to potentially enable all-optical stimulation and interrogation of neural networks with high temporal resolution [107, 216]. Previous attempts to combine optogenetics with GECIs have shown limitations due to the excitation spectrum overlapping with those of light-activated ion channels. For example the excitation spectrum of GCaMP3, GFP-based GECI and the action spectrum of C1V1 red-shifted ChR variant show significant overlap compared to RCaMP1e mRuby-based GECI and ChR2 blue-light-activated ion channel [213]. Additionally it has been demonstrated that blue illumination induced a calcium-independent increase in mApple-based GECIs fluorescence indicative of photoswitching making the GECIs R-GECO, R-CaMP2 and jRGECO1a incompatible with blue-light activated ion channels [213]. Moreover, one drawback of these GECIs resides in their localisation in the neurons. It

has been shown that GECI responses are larger and faster in the cytoplasm than in the nucleus [217]. In fact, GCaMP indicators are naturally excluded from the nucleus while both RCaMP and R-GECO are expressed throughout the cell, including the nucleus [213]. This observation gave rise to the further development of red-shifted such as jRCaMP1a and jRCaMP1b engineered with an NES motif to restrict the expression to the cytoplasm [217]. Importantly jRCaMP1a and jRCaMP1b do not show photoswitching after illumination with blue light [217]. This advantage together with the brightness of these red-shifted GECIs could potentially enable their combination with ChR variants thus open new avenues for all-optical stimulation and interrogation of neural networks.

GECIs	**Excitation Wavelength (nm)**	**Maximum *ΔF/F in vitro*** [a]	**Ca^{2+} free brightness (mM^{-1} cm^{-1})** [b]	**Ca^{2+} saturated brightness (mM^{-1} cm^{-1})** [b]	**Source**
GCaMP3	~ 430	+12	1.8	23	[200]
GCaMP6f	450-490	+52	0.70	37	[218]
GCaMP6s	450-490	+63	0.66	42	[201]
R-CaMP2	~ 550	+4.8	2.3	11	[219]
jR-GECO1a	~ 560	+11	1.0	12	[217]
jRCaMP1b	~ 560	+6.2	4.0	29	[217]

Table 2 - Properties of selected Genetically Encoded Calcium Indicators (GECIs) - [a] Fluorescence change from zero to saturating calcium *in vitro* at 25°C. [b] Calcium-free brightness is calculated from calcium-saturated fluorescence and maximum ΔF/F. Table adapted from [150].

1.4 Thesis aims

The overall aim of this project is to develop a quantitative method that enables large scale functional characterization of neurons to elucidate neural network dynamics with single-cell resolution in healthy and diseased *in vitro* models.

Chapter 3 aims to understand the advantages and limitations of the molecular and imaging tools previously developed to achieve all-optical stimulation and interrogations of neurons. This represents a crucial step in order to design new strategies to overcome these limitations. Therefore, the first part of this chapter focuses on the use of the Optopatch, an optogenetics tools enabling all-optical stimulation and voltage recordings [142]. From these experiments the conclusion was that the recording of multiple neurons simultaneously remains challenging with the GEVI approach. These observations lead onto the development of a new optogenetics tool called the OptoCaMP, a combination of a ChR variant and a GECI which successfully enabled all-optical stimulation and recordings of multiple neurons with a single-cell readout resolution in rat cortical neurons in 2D-culture systems [3]. Chapter 4 focuses on the use of the OptoCaMP in an all-optical assay where a sub- section of a neural network is stimulated while the evoked calcium activity is recorded in both stimulated and non-stimulated neurons. This approach enabled the investigation of the spread of excitation through an interconnected network of rat cortical neurons and induced-pluripotent stem cells derived neurons 2D-culture systems. Furthermore, this assay was applied in a proof-of-concept experiment to demonstrate the sensitivity of this system to report changes in connectivity. This successful experiment brings the promise to enable the study of more complex pharmacological conditions and diseased *in vitro* models.

Chapter 2 - Material and Methods

Chapter 2 - Materials and Methods

2.1 Cell Culture

2.1.1 Human Embryonic Kidney 293T17

The Human Embryonic Kidney (HEK) 293T/17 cell line obtained from ATCC® is a derivative of the 293T cell line and is a highly transfectable derivative of the 293 cell line. The HEK 293T/17 cells were cultured in Dulbecco's Modified Eagle's Medium GlutaMAX™-I supplemented with 10% Fetal Bovine Serum and 10,000 U/mL penicillin, in 75cm^2 flasks. For the subculture, the medium was removed and replaced with 1.5mL of TrypLE Express no phenol red for 3minutes at 37°C. After incubation, 8.5mL of complete growth medium was added and the appropriate aliquot of the cell suspension was re-plated in 75cm^2 flasks for a subcultivation ratio of 1:4 to 1:8. The cultures were incubated at 37°C in a humidified atmosphere of 5% CO_2, 95% air. The medium was renewed every three days. The culture was then frozen down in order to make a stock at the same passage for the reproducibility of the lentivirus production. Each cryovial contained ~8 x 10^5 HEK 293T/17 in complete growth medium supplemented with 10% DMSO.

2.1.2 Mammalian cell culture

2.1.2.1 Primary Rat Cortical Neuron Culture

Primary Rat Cortical Neurons obtained from Gibco® by Life technologies™ were isolated from day-18 Fisher 344 rat embryos. Each vial contained 1 x 10^6 viable neurons highly pure cells containing minimum number of astrocytes and other glial cells (>90%

Microtubule Associated Protein 2 (MAP2)-positive live cells detected by immunofluorescence according to certificate analysis from Life technologies™). The plating medium was Neurobasal® supplemented with GlutaMAX™-I to a final concentration of 0.5 mM and 2% B27 Supplement by Gibco™. The primary rat cortex neurons were plated in WPI Fluorodish™ glass bottom cell culture dishes coated with poly-D-lysine. The poly-D-lysine used for the coating (mol wt 70,000-150,000, Sigma-Aldrich) is a lyophilized powder suitable for cell culture resuspended in HyClone water (2mg/ml) and stored at -20 °C. The poly-D-lysine aliquot was thawed on the day of the plating and diluted in D-PBS (final concentration 50µg/ml) then the coating was performed overnight at room temperature (150 µl). The coating was washed three times with HyClone water (200 µl, 5 minutes) and dried out for minimum 2 hours at room temperature, under the hood, dishes opened. The cryovial was rapidly thawed in a 37°C water bath and plated at a density of 2 x $10^5/cm^2$ for a plated volume of 650 µl in WPI Fluorodish™ glass bottom cell culture dishes coated with poly-D-lysine. The neurons were incubated at 37°C in a humidified atmosphere of 5% CO_2, 95% air. After 14 hours of incubation, half of the medium from was replaced with fresh plating medium. Half of the media was replaced every third day with fresh complete Neurobasal®, B-27™ Supplement and GlutaMAX™-I to a final concentration of 0.5 mM or complete BrainPhys™ and Neurocult™ SM1 to a final concentration of 0.5 mM.

2.1.2.2 Primary Rat Cortical Astrocytes Culture

Primary Rat Cortical Astrocytes obtained from Gibco® by Life technologies™ were isolated from the cortices of Sprague-Dawley rats at embryonic day 19 (E19) and cryopreserved

at the end of the first passage (the cells can be further expanded for at least two additional passages). Each vial contained 1×10^6 cells which were used for co-cultures with hiPSC-derived neurons. They exhibit ≥70% viability after thawing, and ≥80% stain positive for the astrocyte-specific marker glial fibrillary acid protein (GFAP). The plating medium Dulbecco's Modified Eagle's Medium (high glucose) was supplemented with 10% Fetal Bovine Serum and 10,000 U/mL penicillin. The Primary Rat Cortical Astrocytes were plated on WPI Fluorodish™ glass bottom cell culture dishes coated with poly-L-ornithine and laminin for co-cultures with human induced pluripotent stem cells-derived neurons. The poly-L-ornithine coating (150 µl) was performed over night at room temperature (final concentration 0.01mg/ml). The coating was then washed three times with HyClone water (200 µl, 5 minutes) and dried out for minimum 2 hours at room temperature, under the hood, dishes opened. The laminin coating (150 µl) was then performed for 2 hours at 37°C in a humidified atmosphere of 5% CO_2, 95% air. The laminin was removed prior plating of the astrocytes. The cryovial of astrocytes was rapidly thawed in a 37°C water bath and plated at a density of $2 \times 10^5/cm^2$ for a plated volume of 650 µl which were incubated at 37°C in a humidified atmosphere of 5% CO_2, 95% air. After 14 hours of incubation, half of the medium was replaced with Neurobasal® supplemented with GlutaMAX™-I (1:100) and B27 (1:50) from Gibco, 2.5% FBS, 20% Dextrose, MEM non-essential amino acids from Invitrogen (1:200), Doxycycline Hyclate from Sigma (2 µg/ml), Brain-derived neurotrophic factor (BDNF), Ciliary neurotrophic factor (CNTF), Glial cell-derived neurotrophic factor (GDNF) from Peprotech (10 ng/ml) and Cytosine β-D-arabinofuranoside (Ara-C 1 µM) from Sigma for 24 hours. The following day, human

induced pluripotent stem cells-derived neurons were seeded on top of the astrocytes (see *section 2.1.3.1 Healthy and Alzheimer's disease hiPSC-derived neurons*).

2.1.3 Human Induced Pluripotent Stem Cells-derived neurons (hiPSC)

2.1.3.1 Healthy and Alzheimer's disease hiPSC-derived neurons

Two cell lines were received from a collaboration with Dr Tracy Young-Pearse at Brigham and Women's Hospital Harvard Medical School. The first cell line was a human induced pluripotent stem cell (hiPSC) line carrying the mutation APPV717I mutation (London mutation) which will further be referred to here as "fAD". CRISPR-Cas9 (Clustered Regularly Interspaced Short Palindromic Repeats) technology was used to generate isogenic hiPSC lines to fAD with correction of the APPV717I mutation, which will further be referred as "fAD^{corr}". This technology allows genetic material to be added, removed, or altered at particular locations in the genome [220]. Each vial contained 1×10^6 cells and exhibits ≥95% viability after thawing. The plating medium Neurobasal® supplemented with GlutaMAX™-I (1:100) and B27 (1:50) from Gibco, 20% Dextrose, MEM non-essential amino acids from Invitrogen (1:200), Doxycycline Hyclate from Sigma (2 µg/ml), BDNF/CNTF/GDNF from Peprotech (10 ng/ml), ROCK inhibitor (10 µM) from STEMCELL Technologies and puromycin from Life Technologies (5 µg/ml). The hiPSC-derived neurons were rapidly thawed in a 37°C water bath and plated at a density of $5 \times 10^4/cm^2$ for a plated volume of 650 µl in WPI Fluorodish™ glass bottom cell culture dishes coated with poly-L-ornithine and laminin. The hiPSC-derived neurons were incubated at 37°C in a humidified atmosphere of 5% CO_2, 95% air. After 14 hours of incubation, half of the medium was replaced with fresh maintenance medium

Neurobasal® supplemented with GlutaMAX™-I (1:100) and B27 (1:50) from Gibco, 20% Dextrose, MEM non-essential amino acids from Invitrogen (1:200), Doxycycline Hyclate from Sigma (2µg/ml), BDNF/CNTF/GDNF from Peprotech (10 ng/ml) and puromycin from Life Technologies (5µg/ml). For the co-cultures with astrocytes, puromycin was not included in the hiPSC-derived neurons plating nor maintenance medium.

2.1.3.2 iCell® GlutaNeurons

iCell® GlutaNeurons is a commercial line developed by Cellular Dynamics. This line consists of human glutamatergic-enriched cortical neurons derived from human induced pluripotent stem cells (≥90% pure population of primarily glutamatergic human neurons). Each vial contained 1×10^6 cells and exhibits approximatively 70% viability post-thawing. The plating and maintenance medium were prepared as followed: BrainPhys™, iCell Neural Supplement B (1:50), iCell Nervous System Supplement (1:100), N-2 Supplement (1:100) and laminin (1 µg/ml). The hiPSC-derived neurons were rapidly thawed in a 37°C water bath and plated at a density of $2 \times 10^5/cm^2$ for a plated volume of 650 µl in WPI Fluorodish™ glass bottom cell culture dishes coated with poly-L-ornithine and laminin. The hiPSC-derived neurons were incubated at 37°C in a humidified atmosphere of 5% CO_2, 95% air. After 14 hours of incubation, half of the medium from was replaced with fresh maintenance medium. Half of the media was replaced every other day.

2.2 Lentiviral production and transduction

2.2.1 Lentivirus production

The HEK 293T/17 cell line obtained from ATCC® was used to produce the lentivirus FCK-*CaMKIIα*-OptoCaMP (FCK-*CaMKIIα*-jRCaMP1b-P2A-CheRiff) generated during this thesis for the transduction of primary cortical neurons and hiPSC-derived neurons. Viral work was performed within a certified class II biosafety culture hood designated for viral work only. Liquid viral waste was disposed of by aspiration into a viral container containing Virkon. Solid viral waste was placed in an autoclave bag within the biosafety hood and sealed before removal from hood and placed within a viral waste container. Liquid and solid wastes were autoclaved. HEK 293T/17 cells were plated on 10 cm dishes (Nunc) at a density of 5 x 10^6 cells/dish. The following day, the cells were transfected using TransIT®-LT1 Transfection Reagent by Mirus Bio. 27 µl of the Transfection reagent was mixed with 1.5 mL of Opti-MEM I without serum. In a second sterile 1.5 mL microcentrifuge tube, 4 µg of FCK-*CaMKIIα*-OptoCaMP was mixed with 3 µg of psPAX2 packaging plasmid and 2 µg pCMV-VSV-G expressing the envelope plasmid. These plasmids were kindly provided by Dr Paul Reynolds at the University of St Andrews. Both mixes were incubated for 15 minutes at room temperature. After incubation the tube containing the DNA was added to the other reaction tube and incubated for 30 minutes at room temperature. This was then added slowly at the edge of the 10 cm dish containing the 60 % confluent HEK293/T17 cells. These cells were then incubated for 24 hours in an incubator dedicated for viral work at 37°C, 5 % CO_2. Following the 24-hour incubation period, the medium was removed and disposed of by Virkon treatment and

autoclaved. Fresh medium (4mL) was added to the cells, this medium was Neurobasal® supplemented with GlutaMAX™-I to a final concentration of 0.5 mM and 2% B27 Supplement. The viral media were collected 48 hours and 72 hours post transfection and filtered through a 0.45µm Millex-HV filter. Viral stocks were produced and used fresh for every transduction.

2.2.2 Lentiviral transduction of Primary Rat Cortical Neurons

Primary Rat Cortical Neurons (recipient cells) were transduced after 6 days *in vitro* (DIV). On the day of the transduction, the viral media collections were filtered through a 0.45µm Millex-HV filter as previously described (*see section 2.2.1 Lentivirus production*) and various dilutions were prepared in Neurobasal® supplemented with GlutaMAX™-I to a final concentration of 0.5 mM and 2% B27 Supplement or complete BrainPhys™ and Neurocult™ SM1 to a final concentration of 0.5 mM to optimise the viral transduction efficiency (see *section 3.3.2.1 Lentiviral delivery*). 100 µL of the recipient cells media (conditioned media) were collected and incubated at 37°C in a humidified atmosphere of 5% CO_2, 95% air for 4 hours. Meanwhile, 100 µL of the diluted virus were added to the recipient cells and incubated at 37°C in a humidified atmosphere of 5% CO_2, 95% air for 4 hours. After incubation, 300 µL of the recipient cells media were discarded and replaced with a mix of 100 µL of the conditioned medium and 200 µL of pre-warmed Neurobasal® supplemented with GlutaMAX™-I to a final concentration of 0.5mM and 2% B27 Supplement or complete BrainPhys™ and Neurocult™ SM1 to a final concentration of 0.5 mM. Half of the media was replaced the day after and every third day with fresh

complete Neurobasal®, B-27™ Supplement and GlutaMAX™-I to a final concentration of 0.5 mM or complete BrainPhys™ and Neurocult™ SM1 to a final concentration of 0.5mM.

2.2.3 Lentiviral transduction of hiPSC-derived neurons

hiPSC-derived neurons (recipient cells) were transduced at 15 days *in vitro* (DIV). On the day of the transduction, the viral media collections were filtered through a 0.45µm Millex-HV filter as previously described (see *section 2.2.1 Lentivirus production*) and various dilutions were prepared in Neurobasal® supplemented with GlutaMAX™-I (1:100) and B27 (1:50) from Gibco, 20% Dextrose, MEM non-essential amino acids from Invitrogen (1:200), Doxycycline Hyclate from Sigma (2 µg/ml), BDNF/CNTF/GDNF from Peprotech (10 ng/ml) and puromycin from Life Technologies (5 µg/ml). For the co-cultures with astrocytes, puromycin was not included. 100 µL of the recipient cells media (conditioned media) were collected and incubated at 37°C in a humidified atmosphere of 5% CO_2, 95% air for 4 hours. Meanwhile, 100 µL of the diluted virus was added to the recipient cells and incubated at 37°C in a humidified atmosphere of 5% CO_2, 95% air for 4 hours. After incubation, 300 µL of the recipient cells media were discarded and replaced with a mix of 100 µL of the conditioned medium and 200 µL of pre-warmed Neurobasal® supplemented with GlutaMAX™-I (1:100) and B27 (1:50) from Gibco, 20% Dextrose, MEM non-essential amino acids from Invitrogen (1:200), Doxycycline Hyclate from Sigma (2 µg/ml), BDNF/CNTF/GDNF from Peprotech (10 ng/ml) and puromycin from Life Technologies (5 µg/ml). For the co-cultures with astrocytes, puromycin was not included. Half of the media was replaced the day after and every other day with fresh complete Neurobasal® supplemented with GlutaMAX™-I (1:100) and B27 (1:50)

from Gibco, 20% Dextrose, MEM non-essential amino acids from Invitrogen (1:200), Doxycycline Hyclate from Sigma (2 µg/ml), BDNF/CNTF/GDNF from Peprotech (10 ng/ml) and puromycin from Life Technologies (5 µg/ml). For the co-cultures with astrocytes, puromycin was not included.

2.3 Molecular Cloning

2.3.1 Streaking and Isolating Bacteria

FCK-Optopatch2 was a gift from Adam Cohen at Harvard University (Addgene plasmid # 51694) and pGP-CMV-NES-jRCaMP1b was a gift from Douglas S. Kim at Janelia (Addgene plasmid # 63136). Upon reception of the bacteria stab, the bacteria were streaked on a Luria-Bertani (LB) agar Petri dish containing the appropriate antibiotic (ampicillin 100 µg/mL for FCK-Optopatch2 and kanamycin 50 µg/mL for pGP-CMV-NES-jRCaMP1b) and incubated 16 hours.

2.3.2 Plasmid purification

Single colonies were picked from the agar plates using a sterile tip and added to LB Broth liquid culture (5mL or 100mL) supplemented with the appropriate antibiotic (ampicillin 100 µg/mL or kanamycin 50 µg/mL) overnight at 37°C on an orbital incubator at 210 rpm. After the 16 hours incubation, bacteria cultures (750 µL) were thoroughly combined with 80 % glycerol (250 µL) and stored at -80°C, giving a glycerol stock at final concentration of 20 % glycerol. The remaining culture was used for DNA purification using the QIAprep Spin MiniPrep Kit or Plasmid *Plus* Midi Kit from QIAGEN. The DNA concentration and purity were determined using the Thermo Scientific™ *NanoDrop* and

stored at -20°C. DNA was sequenced by the MRC PPU DNA Sequencing and Services at the University of Dundee, plasmid maps of sequences can be found in the Appendices.

2.3.3 Polymerase Chain Reaction (PCR)

PCR was carried out to amplify respectively jRCaMP1b and P2A-CheRiff, into a total reaction volume of 50 µL; Phusion High Fidelity DNA polymerase (NEB), 5X Phusion buffer GC (NEB, UK), 200 µM dNTPs (Roche, UK), 10 µM forward and reverse primers (Thermofisher, UK) (List of primers in Appendix) and 1 µg of DNA were combined. PCR reactions were carried out in a thermal cycler (Bio-Rad, UK) as follow: Step 1, 98°C for 30 s; Step 2, 98°C for 10 s; Step 3, 72°C for 30 sec then Step 4, extension for 60 s at 72°C. Step 2-4 were repeated for 40 cycles; Step 5, 72°C for 10 min; Step 6 incubation at 4°C

2.3.4 Restriction Digest

Restriction digests were carried out using enzymes from New England BioLabs (NEB, UK) in a 30 µL volume. In order to digest 3 µg of DNA, 1 unit of restriction enzyme and NEBuffer™ 3.1 by NEB were used according to manufacturer's guidelines available online (https://nebcloner.neb.com/#!/redigest). The vectors were incubated at 37°C for 120 min. Digested vector products were dephosphorylated with Alkaline Phosphatase, Calf Intestinal (CIP) from NEB at 37°C for 30 minutes to prevent self-ligation.

2.3.5 DNA extraction and purification from agarose gel

Agarose gels were prepared at 1% (w/v) by melting 1g of agarose in 100 mL of 1X TBE Buffer (0.45 mM Tris-borate, 10 mM EDTA, pH 8.3, Sigma-Aldrich, UK). The solution was left to cool down, SYBR Safe DNA Gel Stain from Invitrogen was added (1:10 000) and

the mix was then poured into a horizontal gel chamber and left at room temperature for 30 minutes. DNA samples were prepared with 5X DNA loading buffer. Samples were then loaded into the gel along with a Ladder and electrophoresis was carried out at 65 V for 45 min. The DNA bands were visualized under UV transilluminator (Herolab, UK) at 360 nm and the bands of interest were cut from the gel using a sterile scalpel. The DNA bands were weighted and purified using the QIAquick® Gel Extraction Kit from QIAGEN.

2.3.6 DNA Ligation

Ligation of purified linear DNA into a purified digested plasmid was carried out using Rapid T4 DNA Ligase from NEB. The ligation reaction was set up according to manufacturer's guidelines to include T4 DNA ligase buffer (10X), Vector DNA, Insert DNA and nuclease-free water in a total volume of 20 µL. The molar ratio of insert DNA to vector DNA was 3:1 and control 0:1, calculated using the NEB online tool (http://nebiocalculator.neb.com/#!/ligation). The reaction was incubated for 10 minutes at room temperature. Once ligation was complete, competent *E. coli* cells were used for the transformation (see *section 2.3.7 Transformation*).

2.3.7 Transformation

From a ligation mix, 5µL was added gently to One Shot™ Stbl3™ Chemically Competent *E. coli* from Invitrogen™ according to the manufacturer's guidelines. The cells were incubated on ice for 30 min, following the incubation, they were heat-shocked 45 seconds at 42°C and placed back on ice for 2 minutes. 250 µL of SOC (super optimal broth with catabolite repression) medium (2% tryptone, 0.5% yeast extract, 10 mM NaCl, 2 mM $MgCl_2$, 10 mM $MgSO_4$, 2.5 mM KCl, 20 mM glucose) was added gently to the cells

and the transformation mix was incubated in an orbital incubator at 210 rpm, 37°C for one hour. LB-Agar plates were prepared with the appropriate antibiotic resistance (100 µg/mL ampicillin or 50 µg/mL kanamycin) and 100 µL of the transformation culture was spread on to the plate. All plates were incubated for 16 hours at 37°C. Following the incubation, plasmid purification steps were performed as described in *section 2.3.2 Plasmid purification*.

2.3.8 Construction of the plasmid FCK-CamKIIα-OptoCaMP

The FCK-CaMKIIα-Optopatch2 plasmid was a gift from Adam Cohen (Addgene 51694) and was initially digested using the restriction enzymes BamHI and EcoRI with the NEBuffer™ 3.1 from NEB Biolabs to obtain the lentiviral vector FCK-CaMKIIα. NES-jRCaMP1b was amplified by PCR from the pGP-CMV-NES-jRCaMP1b plasmid (Addgene 63136) with the primers F-GAGAGA**GGATCC**ACCATGCTGCAGAACGAGCTT and R-GAGAGA**GGCGCGCC**CTACTTCGC TGTCATCATTTGTACAAACTC containing BamHI and AscI restriction sites respectively. The nuclear export sequence (NES) was present to the N-termini of jRCaMP1b to restrict its expression in the cytoplasm. P2A-Cheriff was amplified by PCR from the FCK-Optopatch2 plasmid (Addgene 51694) with the primers F- GAGAGA**GGCGCGCC**GGCTCCGGAGCCACGAACTTC and R-GAGAGA**GAATTC**TTACTTGTACAGCTCGTCCATGCC containing AscI and EcoRI restriction sites respectively. The amplified fragments jRCaMP1b and P2A-CheRiff were digested with BamHI-AscI and AscI-EcoRI. Following digestion, a ligation step was performed to link jRCaMP1b and P2A-CheRiff and create one insert jRCaMP1b-P2A-CheRiff. The ligated jRCaMP1b-P2A-CheRiff was then cloned into the FCK-CaMKIIα vector digested with BamHI and EcoRI. The integration of the two fragments jRCaMP1b and P2A-CheRiff

were confirmed by digestion with the restriction enzymes KpnI HF and XmaI. FCK-CaMKIIα-OptoCaMP DNA was submitted for sequencing to the DNA Sequencing and Services at the University of Dundee (*Appendix A - Sequencing and Plasmids*).

2.4 Cytotoxicity assay

Cytotoxicity of FCK-CaMKIIα-OptoCaMP and FCK-CaMKIIα-Optopatch2 via lentiviral transduction in primary cortical neurons was measured at DIV 14 by lactate dehydrogenase (LDH) release assays (Pierce™ LDH Cytotoxicity assay kit) as per the manufacturer's protocol, 7 days after OptoCaMP or Optopatch2 lentiviral transduction. Briefly, 50 µL of the medium supernatant was transferred to a 96-well plate and 50 µL of the reconstituted 2X LDH assay buffer were added to each sample medium and incubated for 30 minutes at room temperature protected from light. The maximum LDH activity was determined after treating neurons with lysis buffer as described in the manufacturer's protocol. The absorbance was measured at 490 nm and 680 nm and the 680 nm absorbance value (background) was subtracted from the 490 nm absorbance.

2.5 Imaging

The samples were imaged using an epifluorescence Nikon Ti inverted microscope, a Nikon 20X Numerical Aperture (NA) 0.75 air objective and a sCMOS Camera (Zyla 5.5, Andor) for OptoCaMP recordings and EMCCD camera (iXon Ultra 897, Andor) for Optopatch2 recordings. All recordings were performed in an automated incubated stage at 37°C in a humidified atmosphere of 5% CO_2, 95% air (Okolab). The change of fluorescence of the OptoCaMP and Optopatch2 were recorded in kinetic series using the software Andor Solis. The blue illumination was provided by a blue light LED at 470 nm

(Thorlabs M470L3 mounted LED) through a B2A filter set (no emission filter, excitation filter 450 – 490 nm). The green illumination was provided by the AURA Light Engine by Lumencor at 550 through a filter set (excitation filter 565/24 nm, dichroic mirror 562 nm, longpass emission filter >570 nm). The red illumination was provided by a stabilized laser (140 mW, Vortran Laser Technology, Inc. VL12148U03) at 637 nm.

2.6 Data Processing and Statistical analysis

Image processing was performed with a Matlab® script designed in our laboratory and a Matlab® toolbox called NeuroCa [221]. The mean global connectivity and the connectivity maps were obtained using the software FluoroSNNAP, an open-source program for the automated quantification of calcium dynamics of single-neurons and network connectivity [222]. Data were expressed as means ± s.e.m. and one-way or two-way ANOVAs tests were used as indicated in the figure legends. The data processing will be further detailed in the next chapters (see section *4.3.1 Method to quantify the neural network connectivity*).

Chapter 3 - Results

All-optical neuronal activity studies

Chapter 3 - Results - All-optical neuronal activity studies.

The aim of this chapter is to understand the advantages and limitations of the molecular and imaging tools previously developed to achieve all-optical stimulation and interrogations of neurons. This represents a crucial step in order to design new strategies to overcome these limitations. Therefore, the first part of this chapter focuses on the use of the Optopatch2, an optogenetics tools enabling all-optical stimulation and voltage recordings [142]. The main conclusion drawn from this all-optical electrophysiology experiment was that the recording of multiple neurons simultaneously remains challenging with the GEVI approach. These observations led onto the development of a new optogenetics tool called the OptoCaMP [3]. The OptoCaMP is a combination of a ChR variant and a GECI which successfully enabled all-optical stimulation and recordings of multiple neurons with a single-cell readout resolution.

3.1 Background

Functional studies of biological neural networks are fundamental to understand brain activity, to investigate how these networks are altered in brain disorders, and to help develop new treatments [223]. To explore heterogeneous neural networks, it is often critical to understand the activity of multiple neurons and how they communicate with each other. To achieve this goal, it is essential to have a tool enabling the simultaneous stimulation and recording from a large population of neurons with a single-cell readout. Electrophysiology has been one of the principal techniques in the field of neuroscience [99]. This approach facilitates both stimulation and recording of individual neurons at

high temporal resolution. Although single cell recordings are precise, it does not lend to high throughput analyses [105]. Moreover this technique is invasive, labour intensive and exhibits limitations when one wishes to characterise a highly heterogeneous neuronal population [101]. MEAs have been developed as a means to overcome the limitations of the invasiveness and the low throughput of electrophysiology with the use of arrays of extracellular electrodes [108, 110]. While enabling the stimulation and recording from multiple neurons simultaneously, the neuronal activity is characterized by triangulating the signal through multiple recording points thus impairing the quantification properties of individual neurons [108, 110]. A method that enables large scale functional characterization of neurons with single cell readout is crucial to elucidate the workings of both healthy and diseased neural populations. To answer this need, optogenetics, an emerging technology which benefits from the synergy of optical and genetic techniques, enables the optical stimulation of specific neuronal populations with high temporal and spatial resolution [101]. This approach uses light-gated ion channels to manipulate neuronal activity. This technique combined with genetically encoded voltage and calcium indicators would enable an all-optical system to stimulate and record the neuronal activity in a contact-free manner with a single-cell resolution thus overcoming the limitations previously described [3, 107]. In addition to these advantages, GEVIs and GECIs offer the advantage to be stably expressed to study how neuronal dynamics evolve over time, while allowing selective sampling of neuronal subsets in heterogeneous populations with the use of genetic labelling of specific neurons [159, 160]. However, elucidating the inner workings of neuronal circuits at the single-cell and network level with GEVIs remains challenging. The limitation of the GEVIs

to report the activity of multiple cells simultaneously stems from their low brightness and the kinetics of the millisecond scale signal they are monitoring. Indeed, recording of action potentials requires high frame rate (e.g. 1kHz) resulting in fewer photons captured per frame which can be compensated by higher illumination intensities. However, higher illumination intensities can result in photobleaching and phototoxicity [156]. In addition, the complexity of the imaging setup required to image multiple cells simultaneously limits the throughput of this technique. In contrast, as previously mentioned, the neuronal electrical activity is accompanied with a change in the calcium dynamics. One of the main advantages of calcium imaging stems from the larger magnitude and slower kinetics of these events compared to action potentials. Therefore, a possible strategy to increase the throughput consists of imaging the resulting changes in the intracellular calcium concentration using GECIs [176]. Combining light-gated ion channels with GECIs would enable the stimulation and recordings of multiple neurons simultaneously with a single-cell readout with the widely accessible wide-field at a lower frame rate (e.g. 5-10 Hz) [176].

3.2 All-optical electrophysiology for single-cell studies

3.2.1 The optogenetic tool Optopatch2

The plasmid FCK-*CaMKIIα*-Optopatch2 (FCK-*CaMKIIα*-QuasAr2-P2A-CheRiff) is an optogenetics tool developed by the Cohen laboratory at Harvard University [142]. It is one of the first molecular tools designed as a bicistronic plasmid to achieve all-optical electrophysiology in mammalian neurons [142]. The main feature of this plasmid consists in the co-expression of the GEVI QuasAr2 and the blue-light-gate ion channel CheRiff via the 2A self-cleaving peptide derived from Porcine Teschovirus-1 (P2A) [224]. Another important aspect is the use of the CaMKII promoter-based lentiviral vector FCK(1.3) for long-term expression of the Optopatch2 in excitatory neurons [225, 226]. Regarding the excitation and emission spectra, CheRiff is an optogenetic actuator based on *Scherffelia dubia* ChR (sdChR) [146] with the mutation E154A as a means to improve the kinetics and shift the peak of the action spectrum to λ_{max} = 460 nm [142]. In the original paper, dissociated hippocampal neurons were transfected with the Optopatch2 plasmid via the calcium phosphate transfection method [227]. This transfection is performed by mixing calcium chloride with recombinant DNA in a phosphate buffer. This allows the formation of DNA/calcium phosphate precipitates which, when gradually dropped onto the recipient cells, adhere to the cell surface resulting in an uptake by endocytosis. This technique exhibits significant drawbacks since the transfection is transient [228] and the typical transfection efficiencies range between 0.5-30% depending on the size of the plasmid and the age of the neuronal population [229, 230]. To overcome these limitations, in this project, a lentiviral-based delivery was optimised

in order to achieve long-term expression of the Optopatch2 with over 95% transduction efficiency and no toxicity (see *section 3.3.2 OptoCaMP and Optopatch2 are successfully expressed in Rat Cortical Neurons*). Importantly, the expression of the Optopatch2 in primary rat cortical neurons was assessed by fluorescence with CheRiff and QuasAr2 respectively tagged with Enhanced Green Fluorescent Protein (eGFP) and mOrange2 (*Figure 3*). Following the successful expression of the Optopatch2 in primary rat cortical neurons *in vitro*, all-optical electrophysiology experiments were performed 7 days post-transduction corresponding to 14 days *in vitro* (DIV).

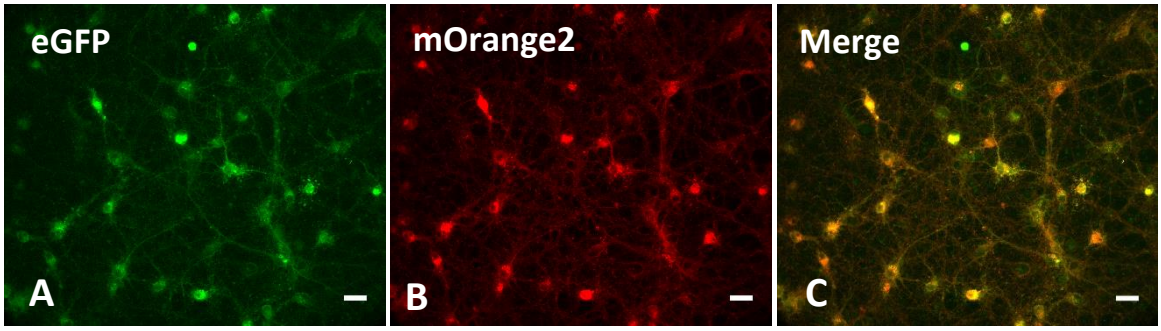

Figure 3 - Dissociated neuronal culture expressing Optopatch2 - Rat cortical neurons *in vitro* at 14 DIV expressing Optopatch2, seven days post lentiviral transduction. **(A)** CheRiff-eGFP expression in green (eGFP); **(B)** GEVI QuasAr2-mOrange2 in red and (C) Merge image of (A) and (B). Scale bar 50 µm.

3.2.2 Optopatch: Imaging system to achieve all-optical electrophysiology

3.2.2.1 Imaging system

To achieve all-optical stimulation and readout using the Optopatch2, the imaging setup was designed with two illumination sources (*Figure 4*). The blue illumination was provided at 470 nm by a mounted LED from Thorlabs (M470L3) and the red illumination was provided at 637 nm by a stabilized laser (140 mW, Vortran Laser Technology, Inc. VL12148U03) in accordance with the respective excitation wavelengths for CheRiff and

QuasAr2. Both illuminations were aligned to coincide into the back epi-fluorescence port of the inverted microscope (Nikon Eclipse Ti). This configuration allows the blue and red light to reach the sample after passing jointly through a Cy5 HQ dichroic mirror and barrier filter 700/75 nm (Nikon). The modulation of the blue light intensity was controlled using a T-cube LED driver (Thorlabs) modulated via a National Instruments LabVIEW 14.0 program designed in our laboratory (see *section 3.2.2.2 CheRiff activation*) [231]. The laser power was controlled with the provided User Interface Software (Vortran Laser Technology, Inc.) and the ensuing beam was passed through an excitation filter (HQ620/60x, Chroma Technology Corp.) before reaching the epifluorescence port. The imaging was performed through a Nikon 20X NA 0.75 air objective and the change of QuasAr2 fluorescence was recorded at ≥1 kHz framerate to capture AP dynamics at the millisecond time scale using an EMCCD camera (iXon Ultra 897, Andor) [142]. The field of view recorded was 96×96 pixels with 4×4 pixels binning (32µm x 32µm) and the "Optically Centred Crop Mode" was enabled using Andor's Optomask in order to increase acquisition speed.

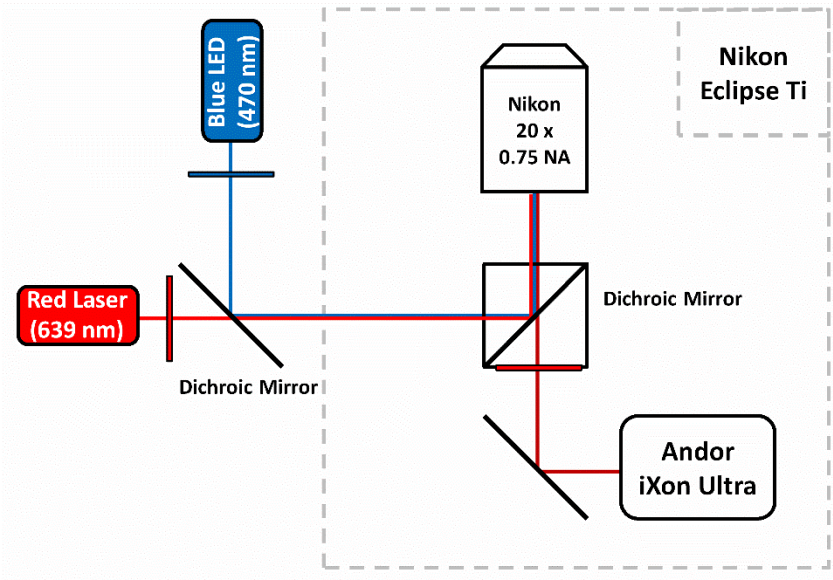

Figure 4 - Optical Setup for Optopatch2 experiment - Schematic drawing of the imaging setup for all-optical stimulus and readout using the Optopatch2. The setup is based on a Nikon Eclipse Ti epifluorescence, the blue and red illuminations reach the sample after passing jointly through a Cy5 HQ dichroic mirror and barrier filter 700/75 nm and the change of fluorescence of QuasAr2 is recorded at ≥1 kHz framerate with an EMCCD camera.

3.2.2.2 CheRiff activation

Precise control of the blue LED is necessary to activate CheRiff and reproduce protocols used in electrophysiology to assess neuronal activity. To achieve this, a LabVIEW script was designed in our laboratory by Marjet Dirks to create a voltage output allowing the change of the blue light pattern of illumination and intensity. This voltage output (0 to 5 V) was first converted by the T-cube LED to a driving current with maximum voltage corresponding to maximal output current and therefore maximal output light intensity. The Labview script was designed to output four distinct waveform types: square step waveforms, sinusoidal waveforms, a single pulse and a single ramp output. Additionally, a user-friendly interface was created as seen in *Figure 5*, where the type of waveform can be selected by clicking on the button "Waveform Selection" thus enabling the adjustment of relevant parameters for this waveform such as the frequency and duration in milliseconds (ms) (*Figure 5*). The frequency is defined by the number of times on cycle of the waveform is repeated per unit of time:

$$f = \frac{1}{T}$$

where f is the frequency in Hertz (Hz), and T represents the period in seconds (s). Additionally, the adjacent section to Waveform selection, titled "Waveform Parameters", allows the user to further determine the number of increments and the possibility to add a Delta Amplitude to the initial starting amplitude (*Figure 5*). Amplitudes are based on percentage of the maximum voltage received by the LED driver. Additionally, the interval which is the duration between each increment in ms can be adjusted at will. Finally, an additional option defined by as delay from the start of the

recording to the start of the waveform can be enabled by clicking on “start delay” and its duration can be adjusted as a delay length in ms. Once these parameters selected, the “Waveform output” is displayed as a plot representing the waveform that will be sent with voltage (V) on the y-axis and the accompanying timestamp on the x-axis (*Figure 5*). The choice of the start trigger for the software can be digital or driven by an external software. These modes can be selected in the tab “Trigger Selection”. The digital start is defined as a trigger upon registering a rising digital signal edge on the selected port of the DAQ card, thus enabling synchronization with auxiliary hardware or software. The software start on the other hand will cause the program to start as soon as the run button is pressed.

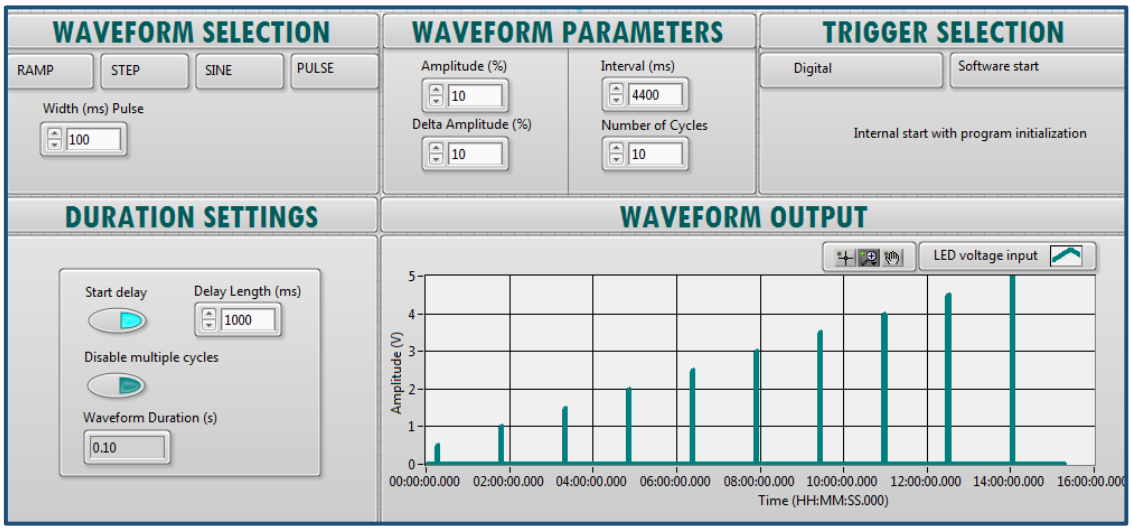

Figure 5 - Labview Interface. The type of waveform can be selected by clicking on the button “Waveform Selection”. “Waveform Parameters”, allows the user to further determine the number of increments and the possibility to add a Δ Amplitude to the initial starting amplitude. Additionally, the interval defined as the duration between each increment can be adjusted at will. An additional option defined by as delay from the start of the recording to the start of the waveform can be enabled by clicking on “start delay” and its duration can be adjusted as a delay length in ms. Once these parameters selected, the “Waveform output” is displayed as a plot according to the waveform that will be sent with voltage (V) on the y-axis and the accompanying timestamp on the x-axis.

Importantly, to characterise the evoked activity resulting from the activation of CheRiff, one must know the intensity of the blue illumination at the sample. Firstly, the relationship between the voltage output defined as a percentage of the maximum voltage output and the blue illumination was determined by measuring the light power using a power meter with Photodiode Sensor (Thorlabs) (*Figure 6*). The intensity at the sample was then calculated according to the surface illuminated and the magnification of the objective used for the imaging (Nikon 20X NA 0.75 air objective) using the formula:

$$I_{sample} = \frac{P}{\pi r^2}$$

where I_{sample} represents the light intensity at the sample in mW/cm^2, P is the light power in mW and r the radius of the illuminated area in cm^2. This calculation was applied to the watt capacity of the blue LED (Table 3*).*

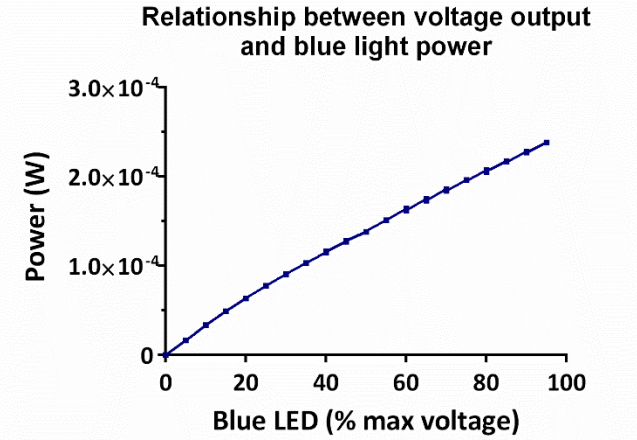

Figure 6 - Relationship between voltage output and blue light intensity. Blue light power (in W) as a function of the Blue LED voltage output (percentage of the maximum voltage output) determined by measuring the light power using a power meter with Photodiode Sensor.

% Blue LED	5	10	20	30	40	50	60	70	80	90	100
I_{sample} **(mW/cm^2)**	4	8	17	24	31	37	44	49	55	61	67

Table 3 - Table recapitulative of the intensity of the blue illumination at the sample. Relationship between the % of the maximum voltage output of the Blue LED and the resulting light intensity at the sample ***(I_{sample})***.

3.2.2.3 All-optical electrophysiology

The blue-light stimuli protocols were inspired from the current injection protocols employed by the Allen Institute to assess neuronal activity [104]. These protocols include the ramp protocol which consists of a continuous increased current until the rheobase is found and the short square or long square steps, which elicit single or multiple action potentials respectively [104]. The ramp protocol translated to blue-light stimuli consists of a continuous photostimulation of 10 seconds duration with increasing intensities until reaching 35mW/cm^2 (delta amplitude = 5 mW/cm^2 ± 1 mW/cm^2) (*Figure 7*). The short square protocol consists in a photostimulation at increasing intensities for 3 ms each sweep with 5 seconds intervals (*Figure 7B*). Finally, the long square steps protocol consists of a photostimulation at increasing intensities for 500 ms each sweep with 5 seconds intervals (*Figure 7C*). For the short and long steps protocol, the blue light intensity is increased of delta amplitude = 5 mW/cm^2 ± 1 mW/cm^2. In a typical experimental procedure, the field of view was chosen using a Nikon 20X NA 0.75 air objective by looking at the fluorescence of mOrange2 from QuasAr2 using a green illumination at 560nm to prevent CheRiff excitation before the experiment. The blue-light stimuli protocols were then applied to a field of view containing a single neuron while the change of the GEVI QuasAr2 fluorescence was recorded at 1 kHz framerate to capture AP dynamics at the millisecond time scale. The size of the field of view optically stimulated and recorded was 96 × 96 pixels with 4 × 4 pixels binning (32µm x 32µm) as a means to increase the number of photon collected. The blue-light stimuli protocols activated CheRiff and consequently changed its conformation inducing a depolarization and the influx of ions. This resulted in an increase in the fluorescence intensity of

QuasAr2 in response to depolarizing currents recorded under red light as previously described (see *section 3.2.2.1 Imaging system*). The fluorescence dynamics were further analysed by selecting a region of interest (ROI) out of the field of view containing the stimulated cell and calculating the average intensity as it changes over time. In order to correct for photobleaching, the image intensity was fitted with a mono-exponential decay as follow:

$$I_{corrected} = \frac{I_t}{e^{-kt}}$$

where $I_{corrected}$ represents the corrected intensity, I_t the signal intensity and *k* the decay constant. The traces show raw average intensity changing over time, with the action potentials increasing in appearance in this case as the intensity of administered blue light is increased (*Figure 7*). These results demonstrate the feasibility of optically stimulated and recording the activity of a single-cell [142] (*Figure 7*). Further trials to record the activity in a larger field of view (> 96x96 pixels binning 4x4 pixels, 32µmx32µm) was unsuccessful due to the impossibility to record the low-brightness signal from QuasAr2 from multiple cells simultaneously. Despite introducing a lentiviral-based approach as a means to improve the number of cells expressing Optopatch2 within the same field, this unsuccessful experiment confirmed the limitation of this imaging setup for low-magnification wide-field imaging. In fact, in the original paper, the illumination to achieve low magnification wide-field epifluorescence imaging was provided by six lasers 640 nm, 500 mW (Dragon Lasers 635M500) [142]. The need for a complex and costly imaging setup represents a significant drawback for the implementation of this novel technology in a non-specialized laboratory and high-throughput screening

platforms. Therefore, these observations emphasise the need of a novel approach and the development of new molecular tools and imaging systems to enable the stimulation and recording of neuronal activity in multiple neurons with a single-cell readout.

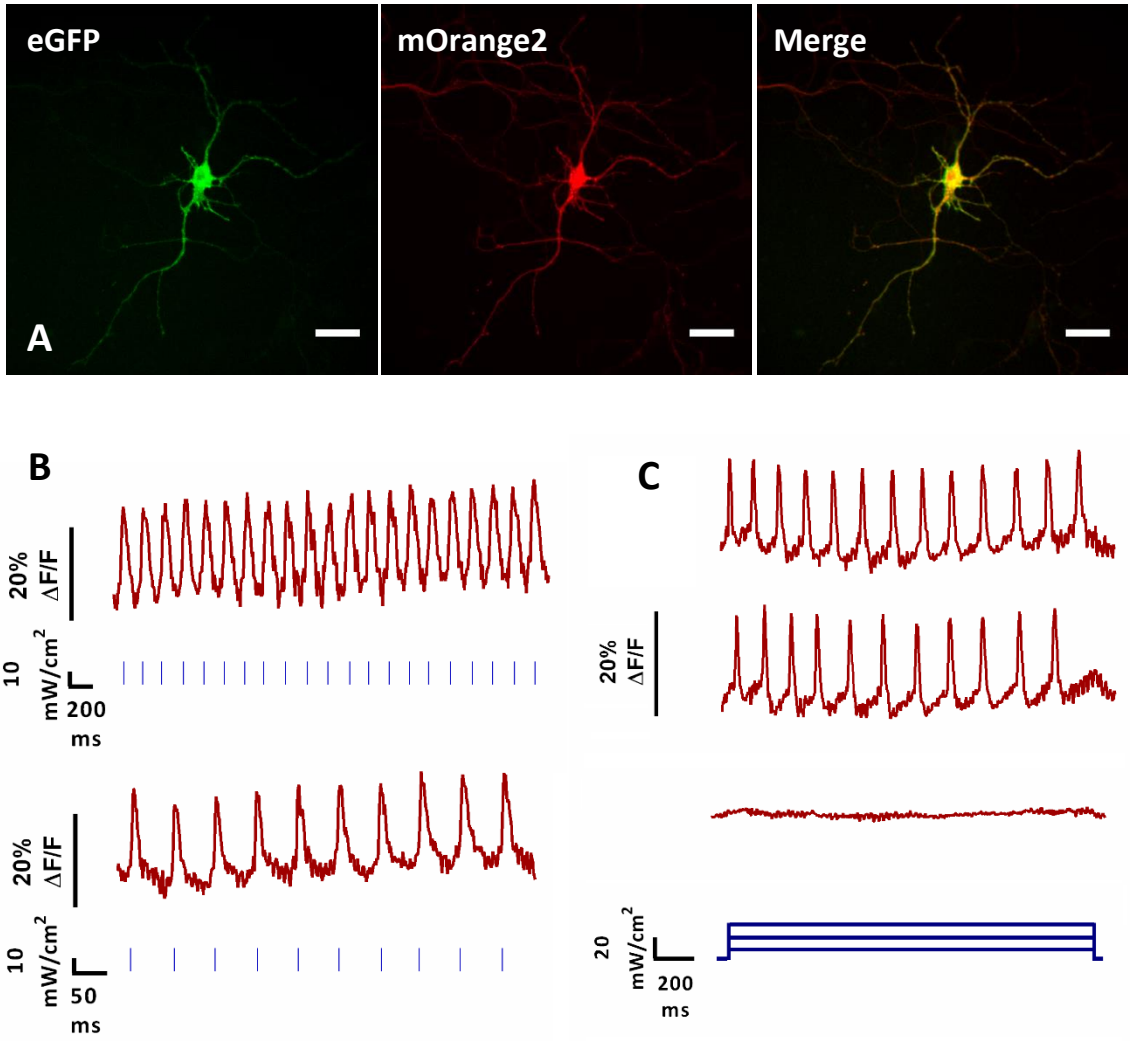

Figure 7 - All-optical electrophysiology. (A) Single channels and merged fluorescence images of a rat cortical neuron expressing Optopatch2 at 14 days *in vitro*: CheRiff-eGFP is displayed in green and the GEVI QuasAr2 in red. Scale bar 30 µm. **(B)** In a typical experimental procedure, the region of interest was chosen using a 20X by looking at the fluorescence of mOrange2 from QuasAr2 using a green illumination at 560nm to prevent CheRiff excitation before the experiment. Single-trial optical recordings of action potentials initiated by pulses of blue illumination (10 ms, 5 mW/cm^2). The red traces represent the signal from the whole-soma fluorescence of a single neuron without photobleaching correction or background subtraction. **(C)** Long pulse protocol with increased blue-light intensities. The red trace represents the signal from the whole-soma fluorescence without photobleaching correction or background subtraction.

3.3 All-optical stimulation and recording from multiple cells

3.3.1 Design of a novel optogenetic tool: OptoCaMP

3.3.2.1 Choice of opsins

A major limitation of all-optical systems is the optical cross-talk between the light-gated ion channel and the excitation/emission wavelength of the readout. The choice of the opsins regarding this matter is crucial to distinguish stimulation and readout. Additionally, another important aspect is the performance of each opsin. Ideally the most performing opsins would be chosen to be combined in order to achieve the greatest all-optical system. Regarding the light-gated ion channel, consistent response to repetitive light stimulation is necessary to enable multiple activations [137, 142, 146]. Regarding the readout, the signal-to-noise ratio is an important parameter to achieve imaging with low light intensity thus limiting photobleaching. Additionally, an important aspect to consider regarding the choice of the readout is how faithfully it reports neuronal activity. OptoCaMP was designed in our laboratory by combining the blue light-gated ion channel CheRiff [142] and the Genetically Encoded Calcium Indicator (GECI) jRCaMP1b [217]. CheRiff is an optogenetic actuator based on *Scherffelia dubia* ChR (sdChR) [146] with the mutation E154A as a means to improve the kinetics and shift the peak of the action spectrum to λ_{max} = 460 nm [142] (*Figure 8*). jRCaMP1b is an mRuby-based GECI which has a larger dynamic range compared to other red-GECIs and does not show saturation in the range of 1–160 action potentials [217]. The mRuby based GECI jRCamp1b excitation and emission spectra do not overlap with the peak excitation of CheRiff (λ_{max} =460 nm). Previously developed calcium indicators have shown a transient increase of red fluorescence after illumination with blue light, which

was not observed for jRCaMP1b making it an ideal candidate for the OptoCaMP. Additionally, in the original research paper, photo-switching was tested with a blue illumination at 470 nm and 3200mW/cm^2 confirming that the blue illumination does not elicit a transient increase of the red fluorescence [217]. Finally, the green illumination used to image the latter does not overlap with the action spectrum of CheRiff thus theoretically avoiding optical cross-talk (*Figure 8*).

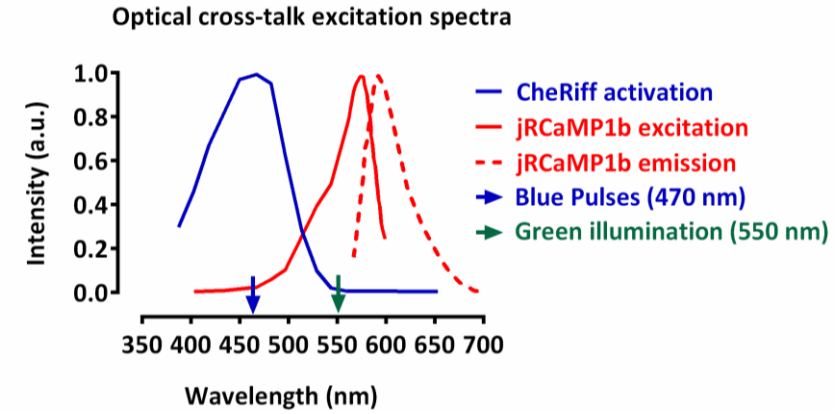

Figure 8 - Excitation and emission spectra of OptoCaMP. Activation spectrum of CheRiff (blue) and excitation/emission spectra of jRCaMP1b (red). The green and blue arrows, respectively, indicate the continuous green illumination at 550 nm and the blue pulses at 470 nm.

3.3.2.1 Construction of the plasmid

The plasmid FCK-CaMKIIα-OptoCaMP (FCK-CaMKIIα-jRCaMP1b-P2A-CheRiff) was designed in our laboratory. The main feature of this plasmid consisted of the co-expression of the GECI jRCaMP1b and CheRiff via the 2A self-cleaving peptide derived from Porcine Teschovirus-1 (P2A) [224]. The P2A sequence has previously been demonstrated to enable a higher cleavage efficiency than the Thosea asigna virus (T2A) [142] making it an ideal candidate for the design of the bicistronic plasmid OptoCaMP. Another important aspect of the cloning strategy was the choice of the vector. Indeed, the ability to infect non-dividing cells, and the ability to deliver complex genetic

elements such as polycistronic sequences and the efficiency of the plasmid expression were crucial especially since the purpose of this study was to investigate connectivity in biological neural networks [232]. To achieve this goal, the CaMKIIα promoter-based lentiviral vector FCK(1.3) developed by the Olsten laboratory was chosen to achieve high transduction efficiency [233]. This vector has previously been demonstrated to drive the strongest expression in pyramidal neurons correlating with the idea to express OptoCaMP in excitatory neurons [225, 226] and has been used for the design of the FCK-CaMKIIα-Optopatch2 [142]. The steps for the construction of the FCK-OptoCaMP are detailed in the Methods (see section *2.3.8 Construction of the plasmid FCK-CamKIIα-OptoCaMP*) (*Figure 9*). FCK-CaMKIIα-OptoCaMP DNA was submitted for sequencing to the DNA Sequencing and Services at the University of Dundee (*Appendix A - Sequencing and Plasmids*).

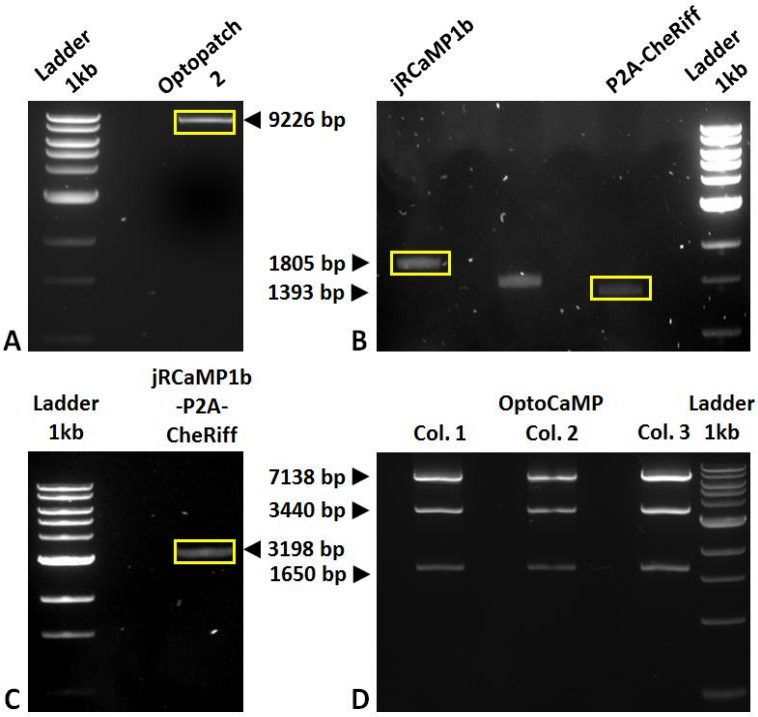

Figure 9 - Agarose gel electrophoresis the construction of FCK- OptoCaMP plasmid. (A) FCK-Optopatch2 digested with the restriction enzymes BamHI and EcoRI, size ~9250 bp; bp=base pairs **(B)** PCR products digested with the restriction enzymes BamHI and EcoRI, jRCaMP1b size ~1800 bp and P2A-CheRiff size ~1400 bp; bp=base pairs. The middle lane is not relevant for this project. **(C)** Ligation to link NES-jRCaMP1b and P2A-CheRiff and create one insert NES-jRCaMP1b-P2A-CheRiff, size ~3200 bp; bp=base pairs. **(D)** Three colonies (Col.) of FCK-CamKII-jRCaMP1b-P2A-CheRiff digested with the restriction enzymes KpnI and XmaI. Expected and confirmed bands: ~7100 bp, ~3400 bp, ~1600 bp; bp=base pairs.

3.3.2 OptoCaMP and Optopatch2 are successfully expressed in Rat Cortical Neurons

3.3.2.1 Lentiviral delivery

Lentiviral vectors derived from the human immunodeficiency virus (HIV-1) have become major tools for gene delivery in neuroscience [234]. The advantageous feature of lentivirus vectors stems from their ability to mediate potent transduction and stable expression in non-diving cells such as neurons [234]. The lentiviral production and transduction were experimentally carried out using the procedures previously described (see *sections 2.2.1 Lentivirus production* and *2.2.2 Lentiviral transduction of Primary Rat Cortical Neurons*). High-titer lentivirus was produced using a second-generation lentiviral system, by co-transfection of HEK293T/17 cells with the Vesicular Stomatitis Virus glycoprotein (VSV-G) pseudotyped lentivirus envelope vector and the packaging plasmid psPAX2 in addition to the viral plasmid FCK-CaMKIIα-Optopatch and FCK-CaMKIIα-OptoCaMP (*Figure 10*). In more details, the pseudotyped plasmid pVSV-G encodes the G protein of the VSV-G envelope gene, the packaging plasmid psPAX2 encodes the pol, gag, rev and tat viral genes and contains the rev-response element (RRE) and finally the plasmids FCK-CaMKIIα-Optopatch and FCK-CaMKIIα-OptoCaMP contain the psi (Y) packaging sequence and the transgene gene inserted between the lentiviral LTRs. After transfection of HEK 293T/17 cells, the cell supernatant contains recombinant lentiviral vectors which can be used to transduce the rat cortical neurons. Once in the rat cortical neurons (RCN), the viral RNA is reverse-transcribed, imported into the

nucleus and stably integrated into the host genome. One or two days after the integration of the viral RNA, the expression of the recombinant protein can be detected.

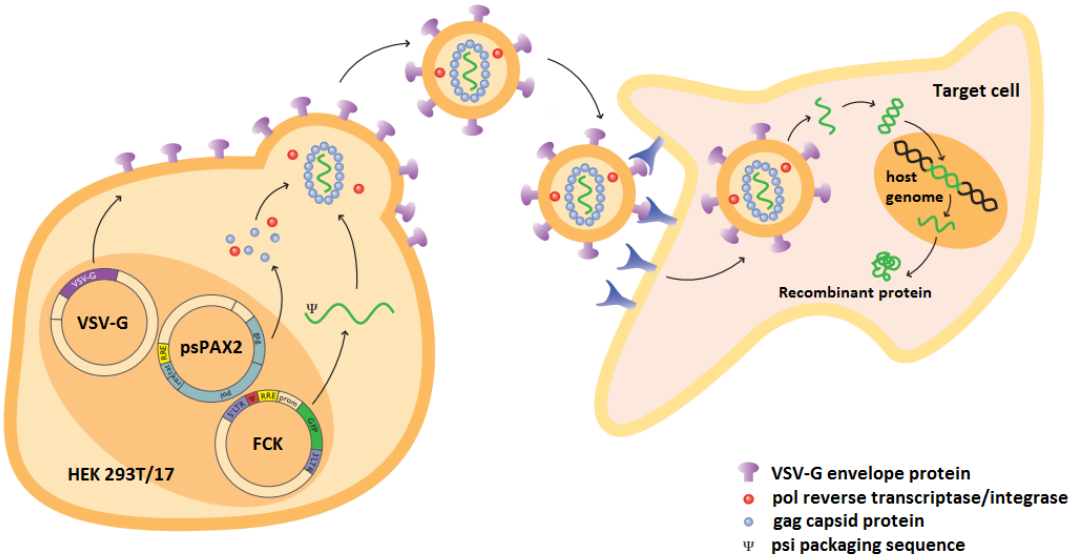

Figure 10 - Lentiviral system. The pseudotyped plasmid pVSV-G encodes the G protein of the Vesicular Stomatitis Virus envelope gene, the packaging plasmid psPAX2 encodes the pol, gag, rev and tat viral genes and contains the rev-response element (RRE) and finally the plasmids FCK-CaMKIIα-Optopatch and FCK-CaMKIIα-OptoCaMP contain the psi (Y) packaging sequence and the transgene gene inserted between the lentiviral LTRs (see plasmids map). After co-transfection of HEK 293T/17 cells, the supernatant contains recombinant lentiviral vectors which can be used to transduce the target cells. Source: Image Adapted from Invivogen.

The lentivirus was freshly produced for each transduction using HEK293/T17 at the same passage throughout this thesis to ensure reproducibility in the titration. Various conditions were tested to optimise the protocol and to find the best candidate to achieve high transfection efficiency and cell viability. These conditions varied by the media used to produce the virus, the use or not of hexadimethrine bromide (polybrene) to increase the transduction efficiency [235] and finally the final concentration of virus as recapitulated in Table 3. For all the conditions, the rat cortical neurons which are the recipient cells were incubated with the diluted virus for 4 hours. The health of the neurons was qualitatively assessed by phase contrast imaging 24 hours post-

transduction focusing on the appearance of beaded structures on the neurites as an indicator of poor health [236]. This qualitative analysis shown unhealthy neurons in the conditions where the virus was produced in DMEM GlutaMAX™-I 10% FBS 10,000 U/mL penicillin at dilutions of up to 1:120 with the total disintegration of the neurites or the apparition of beaded structures on the neurites (Table 4). A similar effect was observed for the neurons transduced with diluted virus produced in Neurobasal®, GlutaMAX™-I and B-27® at dilutions up to 1:30. However, an amelioration in the neuronal health was noticed for more diluted virus produced in Neurobasal®, GlutaMAX™-I and B-27® for dilutions from 1:60 to 1:120 (Table 4). These results emphasise the benefits of the use of diluted virus produced in Neurobasal®, GlutaMAX™-I and B-27® compared to DMEM GlutaMAX™-I 10% FBS 10,000 U/mL penicillin at similar concentrations (Table 4). Regarding the use of polybrene, the culture exhibited very poor health with the disintegration of neurons and neurites independently of the media used to produce the virus (Table 4). Another important parameter to take into consideration is the transduction efficiency which was assessed seven days post-transduction by overlapping fluorescent and phase contrast images. The transduction efficiency is defined by the following formula:

$$Transduction\ efficiency\ (\%) = \frac{Number\ of\ cells\ transduced}{Number\ total\ of\ cells} \times 100$$

This approach was possible since CheRiff and jRCaMP1b are respectively tagged with eGFP and mRuby (*Figure 11*). In addition to the assessment of the transduction efficiency, fluorescence imaging was used to confirm the successful co-expression of NES-jRCaMP1b and CheRiff via the use of the P2A linker (*Figure 11*). The results have shown

that the diluted virus (1:60) produced in Neurobasal®, GlutaMAX™-I and B-27® exhibited the higher transduction efficiency (>95%) among the concentrations tested, and therefore, this was the condition used throughout this thesis. Finally, this analysis confirmed the successful design of the OptoCaMP as a bicistronic plasmid (*Figure 11*).

Construct	Medium	Dilution	Polybrene	Qualitative evaluation of cell health	Transduction efficiency
FCK-*CaMKIIα*-Optopatch2 and FCK-*CaMKIIα*-OptoCaMP	DMEM GlutaMAX™-I 10% FBS 10,000 U/mL penicillin	1:2	8µg/ml	- few neurons in the dish - apparent discontinuous neurites - beaded neurites	>95%
			Not used		
		1:30	8µg/ml		
			Not used		
		1:60	8µg/ml		
			Not used		
		1:120	8µg/ml		
			Not used		
	Neurobasal® GlutaMAX™-I B-27®	1:4	8µg/ml		
			1µg/ml		
			Not used		
		1:6	8µg/ml		
			1µg/ml		
			Not used		
		1:30	Not used		
		1:60	Not used	apparent continuous neurites	> 95%
		1:120	Not used		50%
		1:300	Not used		0%

Table 4 - Lentiviral production and delivery optimisation. For all the conditions, neurons were incubated with the diluted virus for 4 hours. The health of the neurons was qualitatively assessed by phase contrast imaging 24 hours post-transduction focusing on the appearance of beaded structures on the neurites and discontinuous neurites as an indicator of poor health. The transduction efficiency was assessed seven days post-transduction by overlapping fluorescent and phase contrast images.

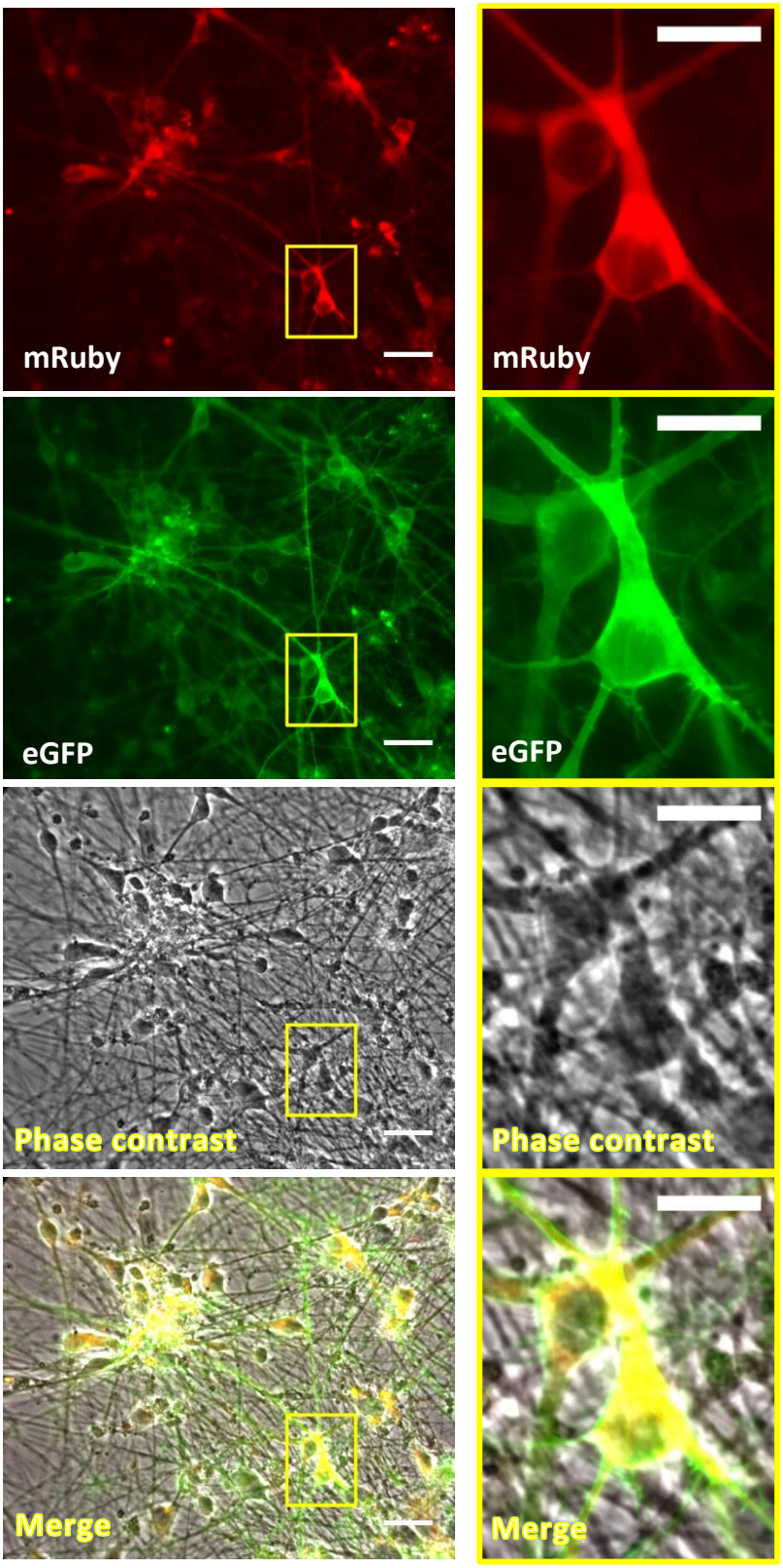

Figure 11 - Transduction efficiency. Single channels (mRuby in red, eGFP in green), phase contrast and merged fluorescence images of RCN expressing OptoCaMP at DIV 14, seven days post lentiviral transduction. Left panel: scale bar 50 µm, right panel: scale bar 30 µm.

3.2.2 OptoCaMP and Optopatch2 are not toxic for Rat Primary Cortical Neurons

A crucial aspect when studying neuronal function is the cell viability. Various approaches can be used to assess cell viability in neuronal cultures including the 3-(4,5-dimethylthiazol-2-yl)-2,5-diphenyltetrazolium bromide (MTT) assay [237], the Alamar Blue [238], the lactate dehydrogenase (LDH) release assay [239]. The MTT assay measures the mitochondrial activity of viable cells by quantifying the conversion of the tetrazolium salt to its formazan product [237]. The Alamar Blue assay has been widely used as a redox indicator to evaluate metabolic function and cellular health [240]. The LDH release assay measures the cytoplasmic lactate dehydrogenase released into the medium as an indicator of cell membrane integrity [239]. The cell membrane integrity being an important parameter for neuronal activity and membrane depolarization, the LDH assay was best-suited to investigate the toxicity of OptoCaMP and Optopatch2. The latter was performed at the time point of the functional imaging (7 days post-lentiviral transduction corresponding to 14 days *in vitro*). The results showed no significant different between the LDH release of the neurons expressing OptoCaMP or Optopatch2 via lentiviral transduction and the non-transduced neurons (a spontaneous LDH release control) (*Figure 12*). This assay demonstrated that the expression of OptoCaMP and Optopatch2 nor the lentiviral transduction were toxic to rat primary cortical neurons at the optimized concentration (1:60).

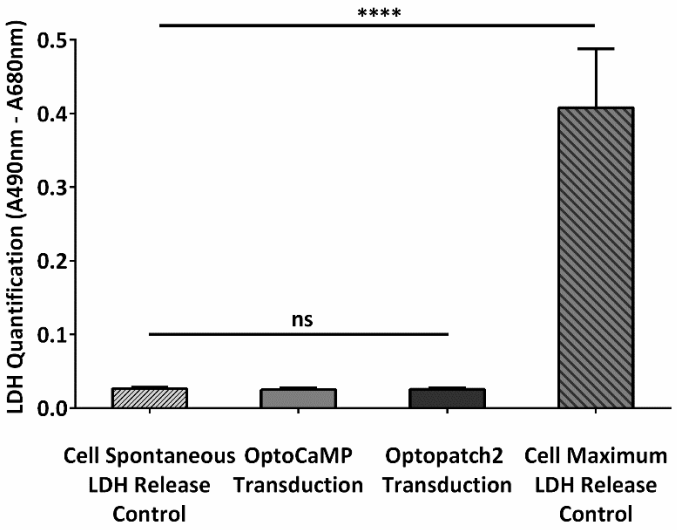

Figure 12 - Quantification of lactate dehydrogenase levels (LDH) in primary cortical neurons seven days after transduction with the OptoCaMP or Optopatch2 - The lentivirus delivery did not show any significant difference between the live rat cortical neurons non-transduced (cell spontaneous LDH release control) and the live rat cortical neurons transduced with OptoCaMP or Optopatch2. (n = 3 independent cell culture experiments, one-way ANOVA, $F(3,8) = 69.26$, $P < 0.0001$; followed by Tukey's multiple comparisons test: OptoCaMP transduction versus Cell spontaneous LDH release control, $P > 0.999$; Optopatch2 transduction versus Cell spontaneous LDH release control, OptoCaMP transduction versus Optopatch2 transduction were not significant different; Cell maximum LDH release control versus Cell spontaneous LDH release control, ****$P < 0.0001$; Cell maximum LDH release control versus OptoCaMP transduced, ****$P < 0.0001$; Cell maximum LDH release control versus Optopatch transduction, ****$P < 0.0001$).

3.3.3 OptoCaMP: Imaging System to achieve dual-excitation

To achieve all-optical stimulation and recording of multiple cells simultaneously, a dual-excitation system was required. The imaging system was designed accordingly with the use of two light-sources. This system was mounted on a Nikon Ti inverted microscope (*Figure 13*). The first illumination consisted of a blue light at 470 nm generated by a mounted LED from Thorlabs (M470L3). This illumination was used for the activation of CheRiff through a B2A filter set (no emission filter, excitation filter 450 – 490 nm) (*Figure 13*). Precise control of the blue LED is necessary to reproduce protocols used in

electrophysiology to assess neuronal activity. To achieve this, a National Instruments LabVIEW 14.0 program was designed in our laboratory to create a voltage output allowing the change of the blue light pattern of illumination and intensity (see *section 3.2.2.2 CheRiff activation*) (*Figure 5*) [231].

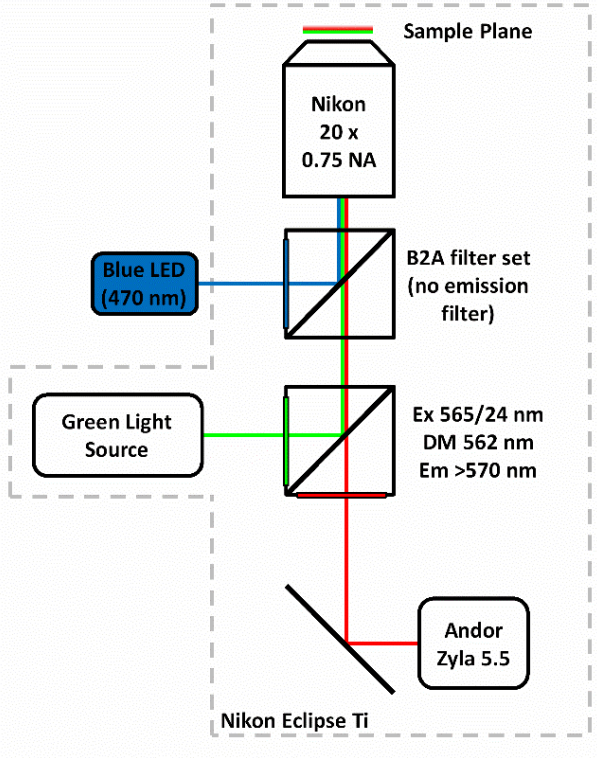

Figure 13 - Optical Setup. Schematic drawing of the imaging setup for all-optical stimulus and readout. The setup is based on a Nikon Eclipse Ti epi-fluorescence microscope mounting a B2A filter set (without the emission filter) for the blue LED illumination (470 nm) and a modified Cy3/TRITC longpass filter set (excitation filter 565/24 nm, dichroic mirror 562 nm, longpass emission filter >570 nm) for the green light source. Recordings are performed at 10 Hz using an Andor Zyla 5.5 sCMOS Camera.

Along with the characterisation of the blue illumination intensities (see *section 3.2.2.2 CheRiff activation*), the intensity of the green illumination at the sample was calculated. Firstly, the relationship between the voltage output defined as a percentage of the maximum voltage output and the green illuminations was determined by measuring the light power using a power meter with Photodiode Sensor (Thorlabs) (*Figure 14*). The

intensity at the sample was then calculated according to the surface illuminated and the magnification of the objective used for the imaging (Nikon 20X NA 0.75 air objective) using the formula:

$$I_{sample} = \frac{P}{\pi r^2}$$

where I_{sample} represents the light intensity at the sample in mW/cm^2, P is the light power in mW and r the radius of the illuminated area in cm^2. This calculation was applied to characterise the continuous green illumination used for imaging throughout this thesis as $I_{sample} = 15$mW/cm^2 corresponding to 7% of the maximum power of the green LED.

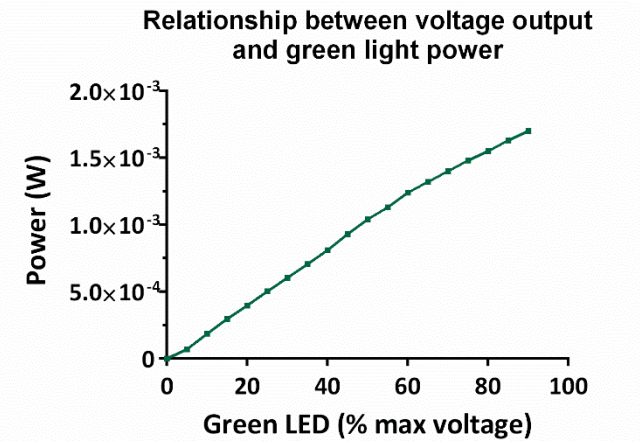

Figure 14 - Relationship between voltage output and green light intensity. Green light power (in W) as a function of the Green LED voltage output (percentage of the maximum voltage output) determined by measuring the light power using a power meter with Photodiode Sensor.

3.3.4 OptoCaMP, an optical crosstalk-free combination

As previously described, there was no optical crosstalk between excitation and emission spectra of the mRuby based GECI jRCamp1b and the spectral peak of CheRiff (λ_{max} =460 nm) (see *Figure 8* in *section 3.3.2.1 Choice of opsins*). Additionally, it has been demonstrated that jRCaMP1b did not show photo-switching after illumination with blue light (470 nm, 3200mW/cm^2) [217]. However, it was essential to experimentally demonstrate that the continuous green illumination did not excite the light-gated ion channel CheRiff thus affect the resting membrane potential of the neurons expressing OptoCaMP. To do so, the change of fluorescence of jRCaMP1b of the neurons included in the field of view was recorded under continuous green whole field illumination at 15mW/cm^2, 550 nm (*Figure 15A*). Following the recordings, traces of the change of fluorescence of jRCaMP1b were extracted and did not show any change under continuous green illumination (*Figure 15A*). Additionally, the neurons were exposed to steps of continuous green illumination (550 nm) with light intensities below (at 3% and 5%) and above (at 10% and 12%) the power used in the all-optical assays (7%, 15mW/cm^2). The average intensities of the whole field of view (*Figure 15B*) and individual traces (*Figure 15C*) of the neurons highlighted (*Figure 15A*) did not show any change under continuous green illumination. This experiment demonstrated that the green illumination at this intensity did not affect the membrane potential of the neurons expressing OptoCaMP thus confirming that it enables all-optical stimulation and recording of neuronal activity.

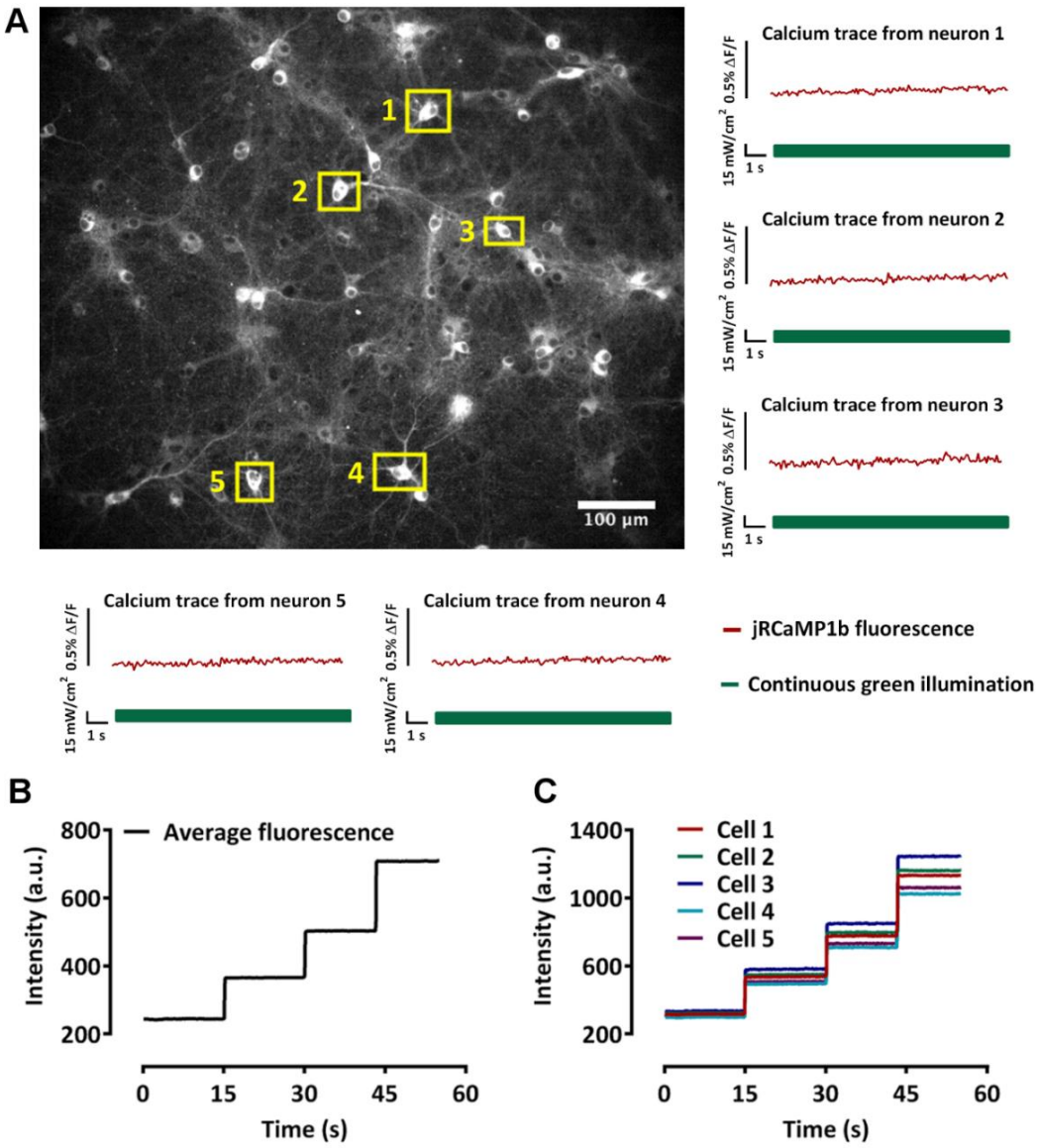

Figure 15 - CheRiff sensitivity under continuous green illumination at 550 nm. (A) Fluorescence image of the microscope field of view (Nikon 20x 0.75 NA air objective) showing a rat cortical neurons culture expressing OptoCaMP (only the mRuby-jRcaMP1b channel is shown) and traces of the change of the GECI jRCaMP1b (red) of individual neurons under continuous green illumination. These traces are representatives of the individual neurons in the whole field of view **(B)** Averaged fluorescence signal from the whole field of view and **(C)** raw data from the single cells highlighted in (A).

3.3.5 All-optical stimulation and recording from multiple neurons

In electrophysiology, protocols consisting of steps of current are injected to determine the AP firing pattern at different current levels [103]. Additionally, as previously described, the Channelrhodopsin variant CheRiff and the Genetically Encoded Calcium Indicator jRCaMP1b have been reported to reliably evoke single action potentials following optical stimulation with blue light (470 nm, 10 ms, 8mW/cm^2) [107] and to report a single action potential up to 160 times without saturation for the GECI [217, 241]. We initially wanted to test whether OptoCaMP would maintain these abilities. Based on this approach, the blue-light stimuli protocols were designed in our laboratory to validate the sensitivity of OptoCaMP and find the optimum illumination conditions. The protocols consisted of ten steps of increasing light intensity of 7mW/cm^2 (±1mW/ cm^2) from 0 to 67 mW/cm^2. The pulse duration varied between 10, 100, 250 to 500 ms. Each pulse was separated by a 5.5 second-interval (*Figure 16B*). The field of view studied typically contained approximately 60 neurons expressing OptoCaMP as a result of the high efficiency transduction with the lentiviral transduction (see *section 3.3.2.1 Lentiviral delivery*) (*Figure 16B*). The blue illumination was applied to the whole field of view to stimulate CheRiff in all the neurons expressing OptoCaMP. This stimulation elicited membrane depolarization resulting in a change of the fluorescence of the GECI jRCaMP1b. The change in fluorescence of each single neuron expressing OptoCaMP in the field of view was simultaneously recorded thus enabling the stimulation and recording of multiple neurons with a single-cell readout.

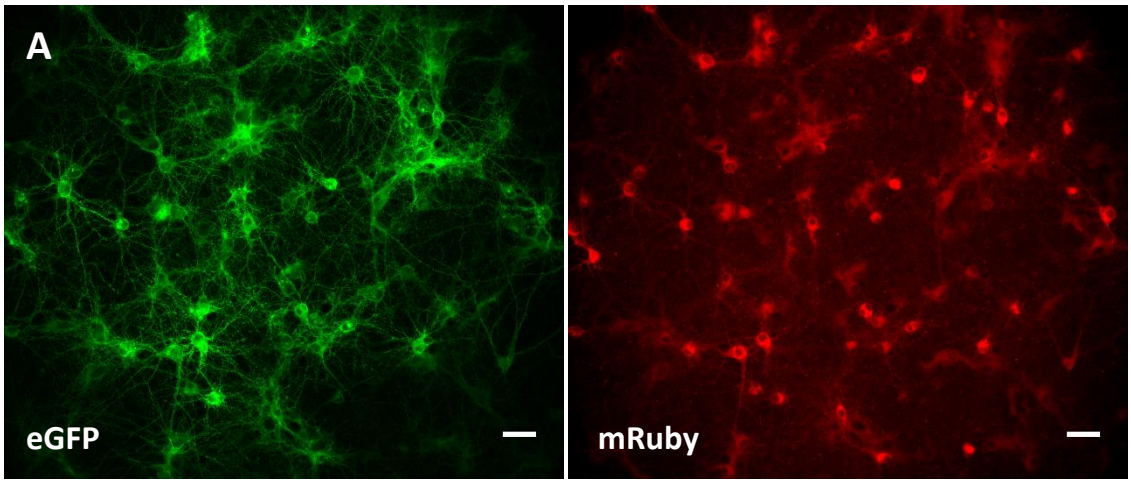

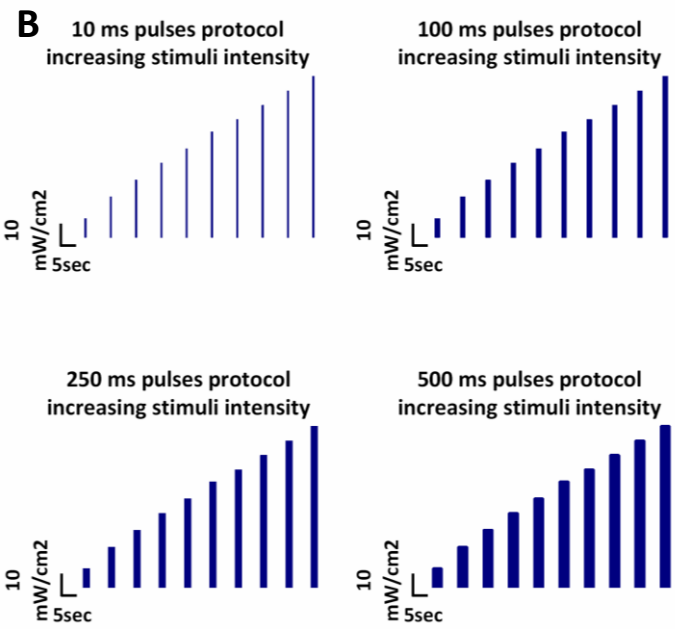

Figure 16 - Blue pulses stimuli protocol applied to neuronal cultures expressing OptoCaMP. (A) Rat cortical neurons at 14 DIV expressing OptoCaMP via lentiviral transduction. CheRiff-eGFP expression in green (eGFP) and GECI jRCaMP1b in red. (mRuby) Scale bar 50 µm. **(B)** Schematic of the blue-light stimuli protocols which consisted in 10 pulses of blue light of 10 ms, 100 ms, 250 ms, and 500 ms with increasing steps of 7 mW/cm^2± 1 mW/ cm^2 between each pulse (measured at the sample).

Following the acquisition, the kinetic series were exported from the Andor Solis software. These recordings were processed using a Matlab® script designed in our laboratory and a Matlab® toolbox called NeuroCa [221]. This process consists in several steps. Firstly, a segmentation is necessary in order to extract the change of fluorescence of single neuron in the field of view containing multiple cells (*Figure 17A and B*). The cell body detection can be achieved using Circular Hough Transform and the Matlab® function *imfindcircles*. Following this segmentation step, each soma is then considered as a ROI resulting in the production of traces indicating the change of fluorescence of each single neuron (*Figure 17B*). These signals were corrected for photobleaching using a bi-exponential curve:

$$I(t) = Be^{-bt} + Ce^{-ct}$$

where *I(t)* is intensity as a function of time *t*, which is directly proportional to the fluorescence level, *B* and *C* representing the initial fluorescence and *b* and *c* their respective rates. To further reconstruct the calcium dynamics of each neuron, the raw signal was converted into the relative value of the baseline *ΔF/F*. We used NeuroCa [221] to estimate the baseline F_0 for each calcium signal. After fitting an exponential decay function to the original fluorescence signal, the histogram of the errors between the original and fitted values was then fit to Gaussian distribution to determine the noise level of the signal. By only using the noise values for the second fitting of a new exponential decay function using NeuroCa [221], the background trend (F) for each ROI could be estimated. The change of fluorescence was then calculated as:

$$\frac{\Delta F}{F} = \frac{F_i - F}{F}$$

where *ΔF/F* represents the change of fluorescence, *Fi* represents the mean fluorescence value of all pixels for each ROI at the i^{th} frame (*Figure 17C*).

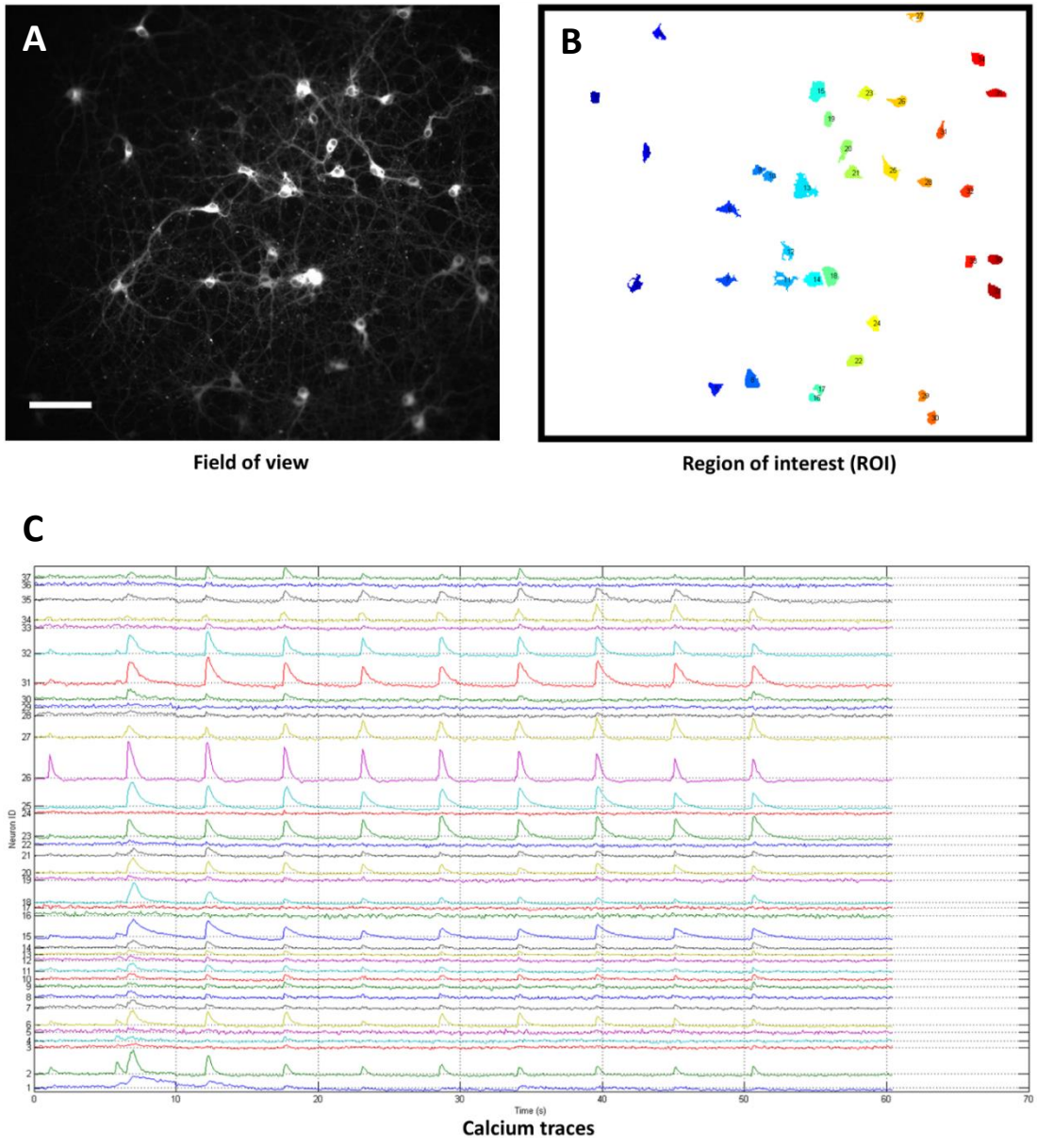

Figure 17 - Analysis Workflow. (A) Fluorescence image (mRuby channel - jRCaMP1b) of the field of view analysed. Scale bar 100 µm. The blue pulses were applied on the whole field of view as described in *Section (3.3.5 All-optical stimulation and recording from multiple neurons)* while recording the change of fluorescence of jRCaMP1b in the whole field of view **(B)** The cell body detection was achieved via Segmentation in order to extract the change of fluorescence of single neuron. **(C)** Following the segmentation step, the calcium trace from individual neurons (region of interest) is extracted. Colour code used for only clarification.

The single-neuron traces enabled the comparison of the evoked calcium activity during each blue pulses protocol (*Figure 18*). Briefly, the protocols applied consisted of ten steps of increasing light intensity of 7mW/cm^2 (±1mW/ cm^2) from 0 to 67 mW/cm^2. The pulse duration varied between 10, 100, 250 to 500 ms. Each pulse evoked a calcium activity which resulted in a change of fluorescence and consequently a peak fluorescence as shown in *Figure 18B*. The peak fluorescence of each neuron was extracted and used to calculate the mean ± s.e.m. of all the neurons in the field of view. This analysis resulted in a graph demonstrating the relationship between the pulse duration (10, 100, 250 or 500ms), the intensity of blue light at the sample (in mW/cm^2) and the peak of change of fluorescence ΔF/F and therefore the calcium activity resulting from the blue pulses stimulation. The lowest calcium influx was observed for the 10ms pulses stimulation while the highest calcium influx was evoked in the 500 ms pulses protocol ($p<0.0001$) (*Figure 18C*). This analysis showed that the peak fluorescence intensities significantly increased with the pulse duration. Interestingly, there was a plateau for the 500 ms pulses protocol by fitting a sigmoidal function to the data points suggesting that the maximum amplitude of calcium is reached for stimuli intensities above 25 mW/cm^2 (*Figure 18C*). Additionally, the two-way ANOVA test followed by Tukey's multiple comparisons test revealed that the peak fluorescence intensities recorded during stimuli intensities above 25mW/cm^2 were not significantly different from each other confirming the reach of a plateau. Synaptic blockers were not added to these recordings and the rat cortical neurons did not exhibit any bursts (*Figure 18B*). However, for further experiment, the addition of synaptic blockers may be required to characterise the culture *in vitro* while avoiding bursts or for some applications (*see*

section Chapter 4 - Results - OptoCaMP enables the study of neuronal network connectivity.) Our results confirmed that OptoCaMP enables simultaneous optical stimulation and monitoring of neuronal activity.

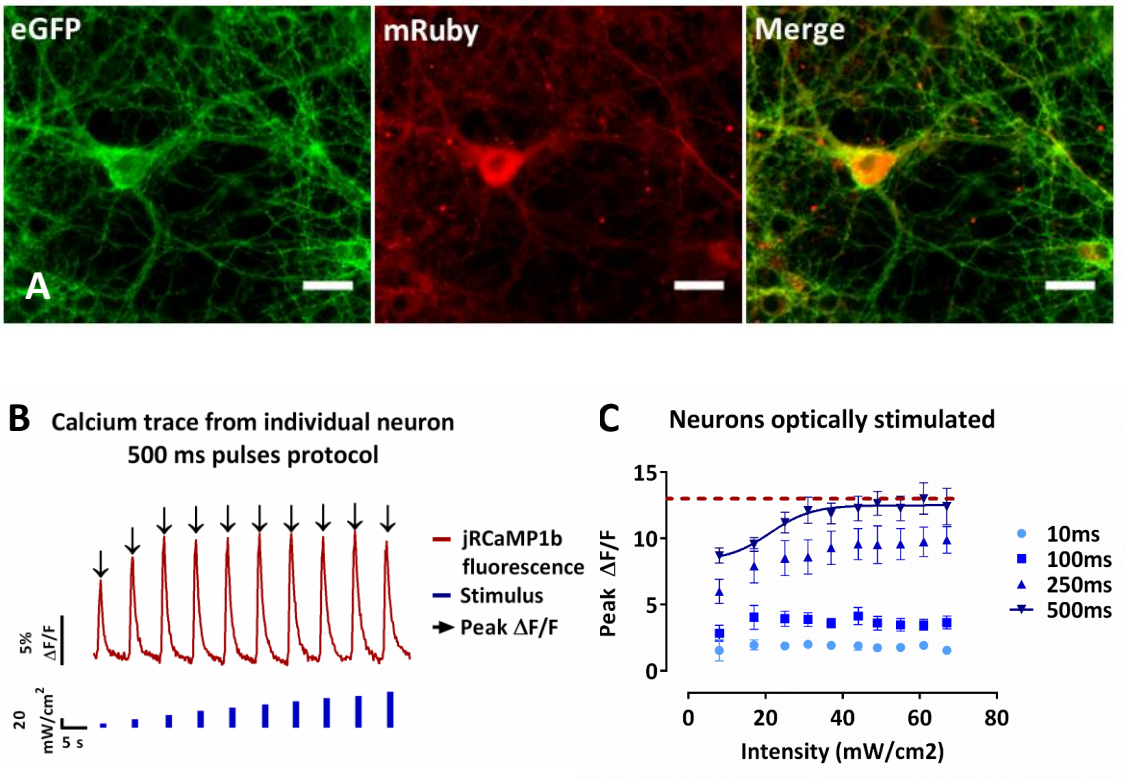

Figure 18 - Characterisation of OptoCaMP to various stimuli protocols. (A) Single channels and merged fluorescence images of rat cortical neurons expressing OptoCaMP at 14 days *in vitro*: CheRiff-eGFP is displayed in green and mRuby based GECI jRCaMP1b in red. Scale bar 25 µm. **(B)** Typical trace of the fluorescence change of the GECI jRCaMP1b (red trace) of a single-neuron during the 500 ms pulses protocol of increasing blue stimulation intensities (0 to 67mW/cm^2). From this trace we can then extract the peak fluorescence ΔF/F (black arrow) for each stimulus intensity for individual neurons of the field of view simultaneously. **(C)** Amplitude of the calcium events in response to increasing stimuli intensities and pulse duration of 10, 100, 250, and 500 ms. The peak fluorescence from individual neuron of the whole field of view stimulated and recorded (n = 60 neurons) was averaged to obtain mean ± s.e.m. values for each stimuli intensity and each protocol (n = 3, two-way ANOVA, effect of the stimulus intensity $F(9,560) = 41.80$, $P < 0.0001$, effect of the stimulation duration $F(3,560) = 4470$, $P < 0.0001$ followed by Tukey's multiple comparisons test showing a plateau (red dashed line) for 500 ms pulses protocol, stimulus above 25 mW/cm^2).

3.4 Discussion

The development of novel molecular tools for optogenetics is revolutionising the field of neuroscience. Notably the development of various ChR and GEVIs such as CheRiff and QuasAr2 represent a significant contribution to the optogenetics toolbox. CheRiff exhibits an important advantage with its improved kinetics and shifted peak of the action spectrum to λ_{max} = 460 nm thus opening new avenues for potential combination with other optogenetics indicators. Additionally, the improvement of the GEVIs has been focusing on the kinetics and brightness with the design of QuasAr2. QuasAr2 offers the ability to report action potentials with high temporal fidelity while displaying a larger fluorescent amplitude in response to voltage changes demonstrating an increased brightness compared to other red-shifted GEVIs. These advantages led to the combination of CheRiff and QuasAr2 in one optogenetics tool called Optopatch2 designed to overcome the limitations of the traditional electrophysiology. As previously described, the traditional electrophysiology is invasive, labour intensive and exhibits limitations when one wishes to characterise a highly heterogeneous neuronal population [101] whereas the Optopatch2 enables all-optical electrophysiology in a contact-free manner but also to target specific cell types via transfection and the use of specific promoters.

In this chapter, the delivery of Optopatch2 to dissociated neuronal cultures was based on a lentiviral transduction approach which resulted in its successful expression with high efficiency as shown in *section 3.3.2.1 Lentiviral delivery*. This optimisation represented a significant improvement compared to the calcium phosphate technique used in the original paper with low to medium efficiency. Indeed, the efficiency is an

important parameter to consider in order to take full advantage of the dissociated culture system, especially in conditions where the starting biological material would not be available in abundance. Additionally, in this chapter optical electrophysiology experiments were presented where various blue-light pulses protocols such as ramp, and long or short pulses successfully depolarized the membrane of single-neurons expressing Optopatch2 resulting in a change of the fluorescence of QuasAr2 as shown in *section 3.2.2.3 All-optical electrophysiology*. The neuronal activity of a single-neuron at a time was successfully optically recorded opening new avenues to optical electrophysiology for disease modelling and drug screening as it does not require mechanical access. Additionally, Optopatch2 is not lethal for mammalian neurons since it preserves the integrity of the cell membrane as demonstrated in *section 3.2.2 OptoCaMP and Optopatch2 are not toxic for Rat Primary Cortical Neurons*, and thus is compatible with studies of long-term responses to chronic pharmacological perturbations. However, to fully unlock the potential of this approach for drug screening, it is crucial to enable recordings from multiple neurons simultaneously to increase the throughput. Furthermore, as a central goal of neuroscience is to understand how the nervous system encodes and processes information at circuit and cellular levels, it is important to record the activity of multiple neurons simultaneously to capture neural networks dynamics [167]. Therefore, further attempts to record the activity in a larger field of view (> 96x96 pixels) in order to attempt to record the activity of multiple neurons simultaneously were performed. These experiments were unsuccessful thus confirming the limitation of the imaging setup with the Optopatch2 for low-magnification wide-field epifluorescence imaging. Indeed, to report changes in voltage,

QuasAr2 must be expressed in the plasma membrane resulting in less effective imaging of voltage transients in larger population of cells under low magnification [175]. Additionally, QuasAr2 must produce enough photons to be detected above noise on a millisecond timescale to report action potentials. Taking into account the kinetics of QuasAr2 and the millisecond scale action potentials, the imaging has to be performed at high frame rates (e.g. 1kHz) [161]. Consequently, faster acquisitions result in fewer photons captured per frame, which can be compensated for by increased indicator brightness or higher illumination intensity. In fact, the illumination to achieve low magnification wide-field imaging in the original publication was provided by six lasers 640 nm, 500 mW (Dragon Lasers 635M500). However, higher illumination intensities can result in photobleaching and phototoxicity [156]. The complexity of the imaging setup required to image multiple cells simultaneously limits the throughput of this technique. Additionally, despite enabling an all-optical approach, Optopatch2 is not suited for voltage clamp experiments [142]. Moreover, absolute voltage with GEVIs are challenging due to variations in expression level and membrane trafficking [216]. In conclusion, optical electrophysiology can indeed enable a direct and precise measure of neuronal activity; however, these experiments are limited to single-cell studies with the widely available microscopy. Applications to larger circuits will likely benefit from further improvements of QuasAr2 such as increased brightness. The neuronal electrical activity is also accompanied by a change in the calcium dynamics. Therefore, a possible strategy to increase the throughput and thus study the neuronal function at network level, consists of imaging the resulting changes in the intracellular calcium concentration [176]. Indeed, as the kinetics of the calcium dynamics are slower than action potentials, the

subsequent recordings of calcium activity requires a lower frame rate (e.g. 5-10 Hz) compared to the one necessary to image the voltage-based events (e.g. 1kHz) [176]. Therefore, calcium imaging can be performed with widely accessible wide-field fluorescence microscopes thus enabling the recording of multiple cells simultaneously [177]. To answer this need, a novel molecular tool for optogenetics called OptoCaMP was created for this thesis as detailed step-by-step in *section 3.3.2.1 Construction of the plasmid*.

OptoCaMP is the first optogenetics tool combining a light-activated ion channel and a GECI which represents a valuable addition to the optogenetics toolbox [241]. The design of OptoCaMP takes advantage of the development of red-shifted GECIs to enable all-optical stimulation and recording of neuronal activity. The lack of spectral overlap between the optogenetic excitation and jRCaMP1b emission wavelengths enabled distinct optical stimulation and recording of evoked calcium events in dissociated neuronal cultures *in vitro* as presented in *section 3.3.4 OptoCaMP, an optical crosstalk-free combination.* Furthermore, to enable the recording of multiple neurons simultaneously, the delivery of OptoCaMP to dissociated neuronal cultures was based on a lentiviral transduction approach to achieve high-transduction efficiency as shown in *section 3.3.2.1 Lentiviral delivery*. In the same section, the successful design of the OptoCaMP has been demonstrated with the co-expression of CheRiff and jRCaMP1b assessed by fluorescence imaging. Moreover, OptoCaMP preserves the membrane integrity which is a particularly important parameter for neuronal activity and membrane depolarization as shown in *section 3.2.2 OptoCaMP and Optopatch2 are not toxic for Rat Primary Cortical Neurons*. Along with the development of a new

optogenetic tool, appropriate analysis processes had to be established. The workflow consisted of several steps starting with the imaging correction such as photobleaching, segmentation to extract single-cell activity as explained step-by-step in 3.3.5 All-optical stimulation and recording from multiple neurons. These steps enabled the characterisation of OptoCaMP at various pulse duration and intensities of blue light stimuli. To do so, simultaneous stimulation and calcium imaging were applied on the whole field of view and it was shown that an increase in the pulse duration (from 10 to 500 ms) resulted in a significant increase in the fluorescence peak as shown in *section 3.3.5 All-optical stimulation and recording from multiple neurons*. Importantly, the excitation of CheRiff evoked significant higher calcium activity until a plateau was reached using a 500 ms pulses protocol at high intensity stimulation (>25 mW/cm2); therefore suggesting saturation of the calcium for long pulses, high blue light intensities (*Figure 18*). The characterisation of OptoCaMP demonstrates the high sensitivity of the channelrhodopsin variant used in OptoCaMP and emphasize a preferable use of low range stimuli intensities which comes with the advantage to reduce the risk of phototoxicity and photobleaching. The capability of OptoCaMP to enable simultaneous optical stimulation and calcium recording of a neural network *in vitro* opens new avenues for the study of disease models and drug screening as it is a contact-free technique. Additionally, OptoCaMP measurements preserve the integrity of the cell membrane and thus is compatible with studies of long-term responses to chronic pharmacological perturbations. Moreover, the recording of multiple cells simultaneously is a crucial aspect as it increases the throughput aspect of an all-optical system. Indeed, this capability represents a considerable advantage compared to the

Optopatch2 however, to clearly correlate Ca^{2+} activity and action potentials, electrophysiology measurements would be necessary to fully characterise this system. Furthermore, in order to confirm that the activity recorded is solely due to the direct optical activation, synaptic blockers could be added to the recording solution and therefore exclude the possibility of any indirect effect. This avenue will be further explored in the next chapter (see section *4.3.2 The all-optical assay based on OptoCaMP is sensitive to change in connectivity*).

In conclusion, the importance of all-optical simultaneous stimulation and recordings of neuronal activity has been demonstrated with the successful use of the Optopatch2 which is a step towards a better understanding of the challenges and limitations of this system. OptoCaMP was designed to tackle the limitations of Optopatch2 with another approach as previously described. However, one of the most fundamental features of a neural network is its connectivity since the single neuron activity is not due only to its intrinsic properties but especially to the direct or indirect influence of other neurons [242]. Therefore, in the next chapter, the development and characterization of an assay will be presented where a subsection of a neural network is stimulated and the activity of the neighbouring neurons along with the stimulated neurons is monitored. This assay allows the investigation of the spread of excitation in a studied network thus allowing quantification of network connectivity.

Chapter 4 - Results

OptoCaMP enables the study of neuronal network connectivity

Chapter 4 - Results - OptoCaMP enables the study of neuronal network connectivity.

This chapter focuses on the use of the OptoCaMP in an all-optical assay where a sub-section of a neural network is stimulated while the evoked calcium activity is recorded in both stimulated and non-stimulated neurons. This approach enabled the investigation of the spread of excitation through an interconnected network of rat cortical neurons and induced-pluripotent stem cells derived neurons 2D-culture systems. Furthermore, this assay was applied in a proof-of-concept experiment to demonstrate the sensitivity of this system to report changes in connectivity. This successful experiment brings the promise to enable the study of more complex pharmacological conditions and diseased *in vitro* models.

4.1 Background

One of the most complex aspect of the human brain resides in the interconnectivity of neural processing elements. Neural connectivity plays a crucial role in neural function and can be described at several levels including brain regions, neural networks connecting neuronal populations and finally individual synaptic connections that link individual neurons [27]. Moreover, neural connectivity refers to anatomical, functional or effective connectivity which respectively refer to a pattern of anatomical links, statistical dependencies or causal interactions between distinct units within a nervous system [27]. These units can be defined as brain regions, neuronal populations or individual neurons. Networks formed by physical connections, such as synapses linking neurons, are characterised by an anatomical connectivity. This connectivity is associated

with structural biophysical parameters such as synaptic strength or effectiveness which are relatively stable at minute-timescale and subject to morphological changes over hours [27]. In contrast, functional connectivity is considered as a statistical concept focusing on the deviations from statistical independence between spatially distributed neurons which can be estimated by measuring correlations, spectral coherence or phase-locking [28]. Moreover, functional connectivity is described as highly time-dependent with statistical patterns between neurons varying on milliseconds to second-timescale. However, functional connectivity does not reflect the directional effects of the correlations between neurons. Therefore, the study of a neural networks and the effects of one neuron over another would require a combination of structural and functional connectivity [27]. This connectivity is called effective connectivity where causal effects can be inferred through systematic perturbations of the system or through a time series analysis. Therefore, a possible way to extract the effective connectivity would be to focus on the application of time series causality measures such as Granger causality or transfer entropy [29]. The investigation of connectivity is crucial to understand how neurons and neural networks process information and how this is affected in neurodegenerative diseases such as Alzheimer's disease. Studies have shown that the dismantling of synapses and neural networks were associated with the accumulation of pathogenic Aβ assemblies in Alzheimer's disease [30]. Additionally, *in vitro* and *in vivo* studies provide evidence that Aβ oligomers reduce glutamatergic synaptic transmission by decreasing the number of surface α-amino-3-hydroxy-5-methyl-4-isoxazolepropionic acid (AMPA) and N-methyl-D-aspartate (NMDA) receptors [31]. These receptors play a crucial role in excitatory synaptic transmission and have

been associated with a collapse of glutamatergic dendritic spines in Alzheimer's disease [30]. Taking these findings into consideration, studying neural networks in Alzheimer's disease may reveal key aspects of these mechanisms at a network level. However, as previously exposed, it is challenging to predict the activity of neural networks by analysing individual neurons and synapses. To overcome this limitation, OptoCaMP was developed to enable studies of multiple cells simultaneously as described in Chapter 3. Although OptoCaMP enables multiple cells studies, this configuration does not fully reflect the network connectivity since the activity of individual neurons is not only due to their intrinsic properties but especially to the direct or indirect influence of other neurons [242]. Consequently, the "whole-field of view stimulated and recorded" configuration is not appropriate for neural network studies as it gives insight into multiple neurons activity but not connectivity. Therefore, this chapter focuses on a variation of the all-optical assay based on the OptoCaMP which could enable the study of the network connectivity. The first part of the chapter presents an all-optical assay where spatially selective optical excitation of a subsection of the network is achieved, while the activity of the neighbouring neurons along with the stimulated neurons are monitored (*see section 4.2 All-optical assay: Temporal and spatial stimulation*). This experiment demonstrated the successful use of this assay to investigate the spread of excitation in the studied network. The subsequent connectivity was investigated using cross-correlation, Granger causality and transfer entropy as means to reveal the effective connectivity (*section 4.3.1 Method to quantify the neural network connectivity*). Furthermore, this analysis was used for the quantification of the mean global connectivity which could potentially enable studies where the network connectivity is

disrupted or enhanced. To verify that this assay is sensitive to such changes, a proof-of-concept experiment was designed to mimic a disrupted and enhanced network connectivity (*section 4.3.2 The all-optical assay based on OptoCaMP is sensitive to change in connectivity*). These encouraging results bring the promise of enabling the study of more complex pharmacological conditions and how diseased neural networks communicate and respond to potential therapeutic agent. With this aim in mind, the last part of this chapter focuses on the translation of this assay to hiPSC-derived neurons models thus opening new avenues for the study of disease models (*section 4.3.3 OptoCaMP in hiPSC-derived neurons and future directions*).

4.2 All-optical assay: Temporal and spatial stimulation

4.2.1 Temporal and spatial stimulation

The purpose of this study was to compare the evoked activity in the stimulated and non-stimulated neurons during various blue-light stimuli protocols. This analysis represented an important step in the characterisation of the OptoCaMP and the all-optical assay to select a protocol to be used for further assays. The temporal stimulation designed and tested in a "whole-field of view stimulated and recorded" configuration previously described (see *section 3.3.5 All-optical stimulation and recording from multiple neurons*) was applied to a subsection of the field of view. Similarly to the setup described in *section 3.3.3 OptoCaMP: Imaging System to achieve dual-excitation*, the blue illumination was generated at 470 nm by a mounted LED from Thorlabs (M470L3) and was used for the activation of CheRiff through a B2A filter set (no emission filter, excitation filter 450 – 490 nm) (*Figure 13*). Additionally, a lever-actuated iris diaphragm (minimum aperture diameter 0.8 mm - maximum aperture diameter 12 mm; Thorlabs SM1D12) with a XY translating lens mount (Thorlabs LM1XY/M) was installed after the blue LED to achieve stimulation of a defined subsection of the field of view. This addition was made in a plane conjugated with the focal plane of the microscope objective to enable modifications of size and/or positions of the blue illumination in the field of view. Precise control of the blue LED was achieved using the National Instruments LabVIEW 14.0 program as previously described (*see section 3.2.2.2 CheRiff activation*). The intensity at the sample was calibrated as described in Chapter 3 (*3.2.2.2 CheRiff activation*) (*Table 3*). To assess the radius of the zone illuminated, a glass bottom dish (WPI) was covered with the ink from a marker fluorescent in the GFP channel when

illuminated with blue light (470 nm) (*Figure 19*). This measurement revealed an illuminated zone with a radius of 300 µm through the 20X objective. Importantly, to demonstrate that the blue pulses of light were restricted to the defined subsection of the field of view, synaptic blockers were added prior to the recording the temporal stimulation designed and tested in a "whole-field of view stimulated and recorded" configuration previously described (see *section 3.3.5 All-optical stimulation and recording from multiple neurons*) was applied to a subsection of the field of view while recording the whole field of view with the addition of synaptic blockers. For this experiment, the synaptic blockers CNQX (6-Cyano-7-nitroquinoxaline-2,3-dione) (2 µM) and D-APV (D(-)-2-Amino-5-phosphonopentanoic acid) (10 µM), respectively AMPA and NMDA receptors antagonists were added to the recording solution [243] (*Figure 19*). This addition modulates excitatory transmission by blocking the activation of postsynaptic ionotropic receptors (NMDA and AMPA) thus blocking the excitatory synaptic activity [243]. As expected, the recording showed activity in the stimulated neurons (black arrows *Figure 19C*) but no activity in the non-stimulated neurons (*Figure 19C*). Additionally, this experiment supported the potential use of this system in a configuration where the blue pulses of light are restricted to a subsection of the field of view to study neural networks.

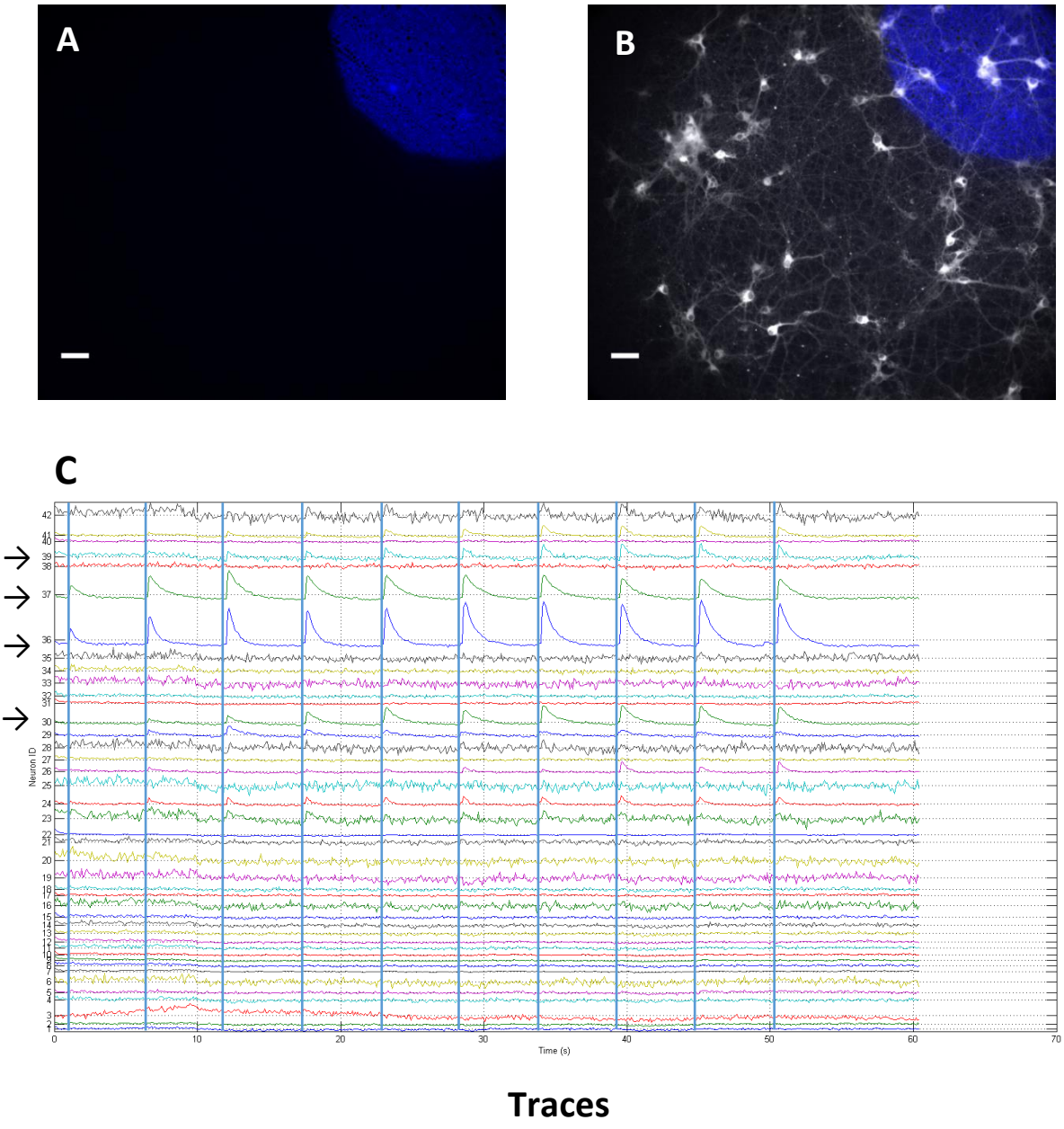

Figure 19 - Blue Illumination restricted to a subsection of the field of view. (A) Image of a glass bottom dish (WPI Fluorodish) covered with the ink from a marker that is fluorescent in the GFP channel when illuminated with blue light (470 nm), scale bar 50 µm. (B) (C) Overlapped image of Neurons expressing OptoCaMP, fluorescence image of jRCaMP1b (red channel), scale bar 50 µm and blue stimulus (A), scale bar 50 µm. Following the segmentation step, the calcium trace from individual neurons (region of interest) is extracted. The traces showed activity only for the neurons stimulated. Colour code used for only clarification. The vertical lines correspond to the time when the blue stimulus was applied. Black arrows showing the traces of the stimulated neurons.

4.2.2 Characterisation and optimisation of the system

For analysis purposes and to select the most robust protocol for further assays, the field of view recorded was divided into three zones: the blue zone containing the stimulated neurons and zones 1 and 2, respectively green and red, containing the non-stimulated neurons as shown in *Figure 20A*. In the green and red zones (zones 1 and 2, respectively) neurons were not stimulated with blue pulses of light. The discrimination between these two zones were defined by drawing a virtual circle of 600 µm which corresponds to two times the radius of the blue zone (300 µm). The traces of the changes of jRCaMP1b fluorescence of individual neurons were extracted using the method previously described in *section 3.3.5 All-optical stimulation and recording from multiple neurons* (*Figure 17)*. Briefly, following the segmentation of the field of view, each soma is then considered as a ROI resulting in the production of traces indicating the change of fluorescence of individual neurons. Additionally, the signals were further corrected for photobleaching as described in *section 3.3.5 All-optical stimulation and recording from multiple neurons*. As previously demonstrated in Chapter 3, each pulse of blue light depolarised the stimulated neurons resulting in a change in their activity reported by an increase in the fluorescence of jRCaMP1b as expected (see *section 3.3.5 All-optical stimulation and recording from multiple neurons*). Interestingly, the neurons expressing OptoCaMP which did not receive any direct stimuli, exhibited a change in the fluorescence of the GECI jRCaMP1b as well. This observation suggested that the calcium activity of the non-stimulated neurons resulted from a spread of excitation. Therefore, the protocols previously designed in Chapter 3 (see *section 3.3.5 All-optical stimulation and recording from multiple neurons*) were applied in this configuration in order to

select the most robust protocol for further assays. Briefly, the protocols consisted of ten steps of increasing light intensity of 7mW/cm^2 (±1mW/ cm^2) from 0 to 67 mW/cm^2. The pulse duration varied between 10, 100, 250 to 500 ms and each pulse was separated by a 5.5 second-interval (*Figure 16B*).

Following these steps, the values of the peak fluorescence intensities following each stimulus were extracted and the average ± s.e.m. for the neurons localised in the same zones was calculated. These values were plotted against the stimulus intensity corresponding to the intensity of the blue light pulses (I_{sample} in mW/cm^2). Each temporal protocol was analysed separately (*Figure 20*). The analysis of the 10 ms pulses protocol revealed an increase in the peak fluorescence for stimuli intensities between 44 mW/cm^2 and 60 mW/cm^2 for the non-stimulated neurons in the zones 1 and 2 ($p>0.05$) (*Figure 20B*). Moreover, this increase resulted in higher peak fluorescence intensities in the non-stimulated neurons compared to the stimulated neurons. However, there was no significant difference between the peak fluorescence in the non-stimulated neurons in zones 1 and 2 (*Figure 20B*). The analysis of the 100 ms pulses protocol showed that the peak fluorescence intensities for the non-stimulated neurons (*Figure 20C*). Additionally, the peak fluorescence intensities were not significantly different for the non-stimulated neurons in the zones 1 and 2 (*Figure 20C*). During the 250 ms, the peak fluorescence intensities for the stimulated neurons increased with the stimuli intensities and were significantly higher than the peak fluorescence intensities for the non-stimulated neurons zone 1 and 2 ($p<0.0001$) (*Figure 20D*). In contrast, there was no significant difference between the peak fluorescence intensities of zones 1 and

2 (*Figure 20D*). During the 500 ms protocol, the peak fluorescence intensities for the stimulated neurons increased with the stimuli intensities until reaching a plateau for stimuli intensities above 25 mW/cm^2 (*Figure 20E*). Additionally, the peak fluorescence intensities of the stimulated neurons were significantly higher than the peak fluorescence for the non-stimulated neurons in zone 1 and 2 (*Figure 20D*). Furthermore, the 500 ms pulses protocol revealed significantly lower peak fluorescence intensities for the neurons in zone 2 compared to the zone 1 ($p<0.0001$) (*Figure 20D*). Interestingly, this observation was not made during the shorter pulses protocols (10, 100 and 250ms) (*Figure 20B-D*).

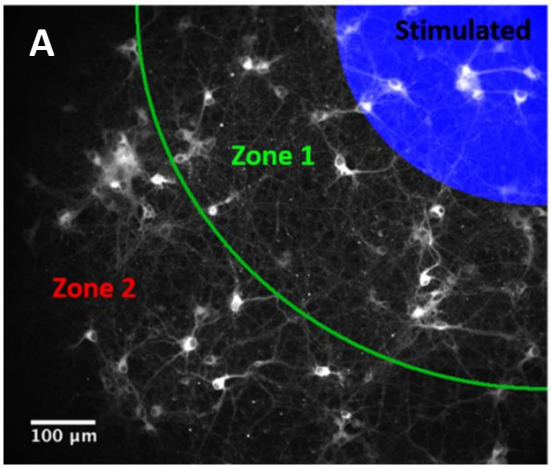

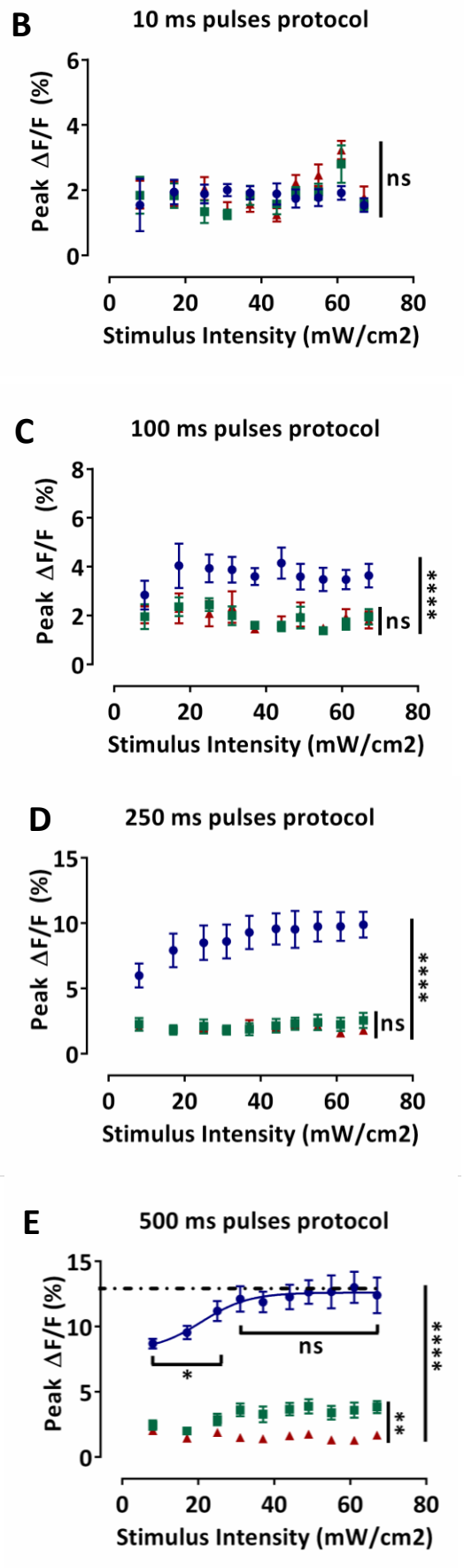

Figure 20 - Relationship between stimulus intensity, length and calcium activity. (A) Map defining the three zones for the spatio-temporal optical stimuli protocols and analysis. Neurons in the blue zone were stimulated, neurons in zone 1 (green) and 2 (red) were not stimulated. The discrimination between these two zones were defined by drawing a virtual circle of 600 µm which corresponds to two times the radius of the blue zone (300 µm). **(C-E)** The activity of each neuron is first extracted then the average of the peak fluorescence intensities of single-neurons in the same zone ± s.e.m. is calculated and displayed against the stimulus intensity for the 10 ms **(B)**, 100 ms **(C)**, 250 ms **(D)**, and 500 ms **(E)** pulses protocols. According to the map in (A), in blue, average peak fluorescence intensity for the stimulated neurons, in green, non-stimulated neurons in the zone 1 and in red, non-stimulated neurons in the zone 2 (n = 60 neurons and 3 independent cell culture experiments, one-way ANOVA, (A) $F(2,27) = 0.4533$, $P = 0.6403$; (B) $F(2,27) = 298.8$, $P < 0.0001$; (C) $F(2,27) = 301.7$, $P < 0.0001$; (D) two-way ANOVA, effect of the stimulus intensity $F(9,370) = 39.65$, $P < 0.0001$ and effect of distance to stimuli (zones) $F(2,370) = 9316$, $P < 0.0001$; (B–E) followed by Tukey's multiple comparisons test: ns=non-significant, $*P < 0.05$, $**P < 0.01$, $****P < 0.0001$).

To further characterise the protocols applied, the peak fluorescence intensities for each stimuli protocol were pooled and plotted against the stimulus duration (*Figure 21*). This analysis was performed for each defined zone separately to focus on the relationship between the pulse duration and the activity in each zone. This analysis revealed that an increase in the pulse duration resulted in a significant increase in the peak fluorescence intensities for the stimulated neurons ($p<0.0001$) (*Figure 21A*). Interestingly, there was no significant difference in the activity of the non-stimulated neurons (zone 1 and 2) during the 10ms, 100ms and 250ms protocol (*Figure 21B, 22C*). In contrast, the 500 ms pulses protocol exhibited significantly higher peak fluorescence intensities for the non-stimulated neurons in the zone 1 compared to other protocols ($p<0.01$) (*Figure 21B*). Additionally, this analysis showed a significant decrease in the peak fluorescence intensities for the non-stimulated neurons in the zone 2 during the 500 ms pulses protocol compared to the other protocols ($p<0.05$) (*Figure 21C*). Finally, the two-way ANOVA test revealed that the pulse duration and intensity had a significant impact in the stimulated neurons. In contrast, only the stimulus duration had a significant impact on the non-stimulated neurons zone 1 and zone 2 but not the stimulus intensity. Although an increase in the pulse duration evoked greater calcium response in the stimulated neurons, it did not result in greater calcium activity in the non-stimulated neurons (*Figure 21B, 22C*). This phenomenon is potentially linked to the maximum synaptic activation between stimulated and non-stimulated neurons being reached. Furthermore, the activity of the non-stimulated neurons in zone 2 showed a significant reduction for the 500 ms pulse protocol compared to shorter pulse duration (*Figure 21C*). This observation together with the fact that high levels of intracellular calcium have

been associated to cell damage [244], led to the conclusion that the 500ms pulses were not the optimum stimulation. In contrast, an increase in the pulse duration from the 10 ms, the 100 ms and 250 ms pulses protocols evoked significantly higher peak fluorescence intensities in the stimulated neurons without evoking significantly higher peak fluorescence intensities for the non-stimulated neurons in the zones 1 and 2. This observation is particularly important as it emphasises the fact that the 250 ms pulses protocol do not exhibit a particular advantage over the shorter pulses protocol. Moreover, the use of shorter pulses protocol results in an increase of the throughput of this system. Therefore, the 250 ms pulses protocol was not selected for further applications. Although the use of shorter pulses protocols increases the throughput of this system, the 100 ms protocol demonstrated a better reproducibility than the 10 ms protocol. Reproducibility being a challenging and crucial parameter [245], the 100 ms pulses was selected as the final protocol to achieve a higher throughput of this system with reproducibility.

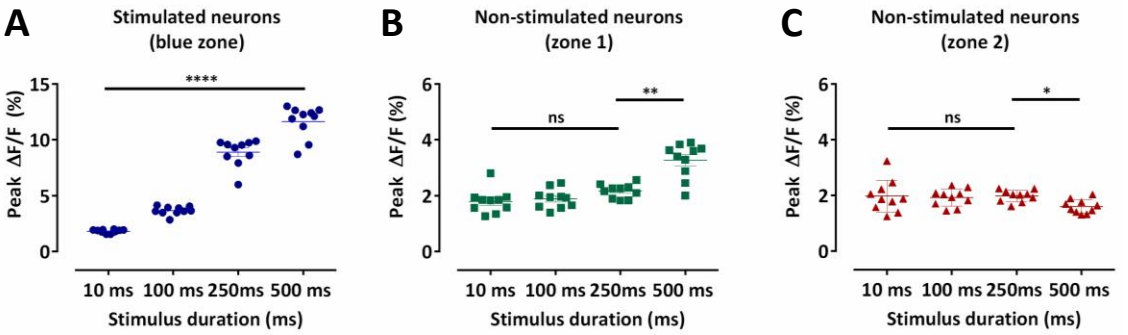

Figure 21 - Pooled peak fluorescence intensities of each defined zone separately ± s.e.m. (A) stimulated neurons, (B) non-stimulated neurons in zone 1, and (C) non-stimulated neurons in zone 2 for stimuli intensities from 0 to 67 mW/cm^2 against the pulse duration. (n=3 independent cell culture experiments, two-way ANOVA, (A) effect of the stimulus intensity $F(9,520) = 2810$, $P < 0.01$ and effect of the stimulation duration $F(3,520) = 296.1$, $P < 0.0001$; (B) effect of the stimulus intensity $F(9,520)=0.7990$, non-significant and effect of the stimulus duration $F(3,520) = 26.21$, $P < 0.0001$; (C) effect of the stimulus intensity $F(9,520) = 0.8480$, non-significant and effect of the stimulus duration $F(3,520) = 2.994$, $P < 0.05$; (A-C) followed by Tukey's multiple comparisons test: ns=non-significant, ∗$P < 0.05$, ∗∗$P < 0.01$, ∗∗∗$P < 0.001$, ∗∗∗∗$P < 0.0001$).

4.3 OptoCaMP enables the study of neural network connectivity

4.3.1 Method to quantify the neural network connectivity

In the first part of this chapter, the use of temporal and spatial stimulation has been demonstrated to enable the study of the activity of stimulated and non-stimulated neurons with a single-neuron readout. This successful experiment represents a crucial step in order to study the connectivity of a neural network since the single neuron activity is not due only to its intrinsic properties, but especially because of the direct or indirect influence of other neurons [242]. Therefore, the calcium activity of individual neurons can be temporally and spatially correlated to characterize the network connectivity [246]. To achieve this characterisation, an open-source program called FluoroSNNAP was used for the automated quantification of calcium dynamics of single-neurons and network connectivity [222]. As previously described, the traces of the changes of jRCaMP1b fluorescence of individual neurons were extracted using the method described in *section 3.3.5 All-optical stimulation and recording from multiple neurons* (*Figure 17*). Briefly, following the segmentation of the field of view, each soma is considered as a ROI resulting in the production of traces indicating the change of fluorescence of individual neurons. The signals were further corrected for photobleaching as described in *section 3.3.5 All-optical stimulation and recording from multiple neurons.* Following these steps, several measurements are implemented in FluoroSNNAP to phenotype the temporal dynamics of calcium activity occurring within individual neurons. Measures such as the distribution and kinetics of the calcium transients were provided for each neuron identified with the segmentation tool. These measurements describe the spatiotemporal profile of calcium transients on a single

neuron basis and can be a useful adjunct to changes in the network connectivity. The distribution of transients is characterised by the number of calcium events per neuron and the distribution of inter-event-interval which are important measures of the level of activity and rhythmicity. The mean and standard deviation of the inter-event-intervals distribution for each neuron is reported in this analysis (*Figure 22*). Additionally, the kinetics of the transients is characterised by the amplitude, the rise time and the fall time of the calcium events (*Figure 22*). The rise time is determined as the time-to-peak fluorescence intensity and the fall time is defined with the exponential decay of the curve-fitting calcium event. The amplitude is defined as the maximum peak fluorescence intensity over baseline following the onset of a calcium event (*Figure 22*).

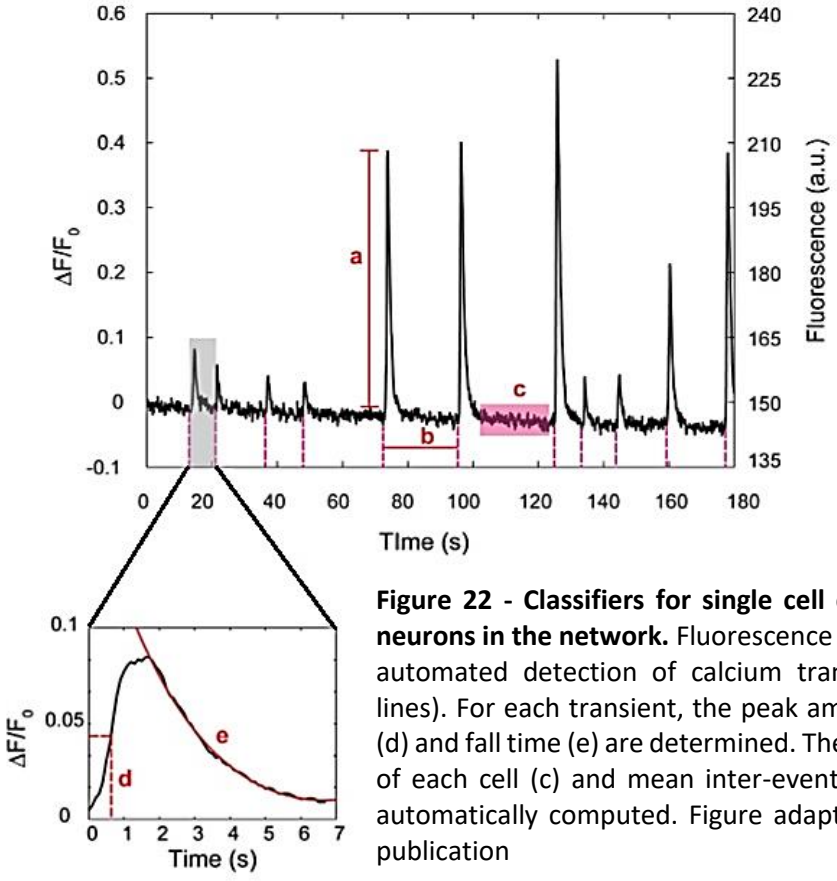

Figure 22 - Classifiers for single cell calcium dynamics of neurons in the network. Fluorescence vs. time trace depicts automated detection of calcium transients (pink dashed lines). For each transient, the peak amplitude (a), rise time (d) and fall time (e) are determined. The resting fluorescence of each cell (c) and mean inter-event-interval (b) are also automatically computed. Figure adapted from the original publication

These automated measurements are further used to determine the temporal relationships between the time series of two neurons through cross-correlation, Granger causality and transfer entropy. The cross-correlation approach is the simplest method to assess temporal relationships of calcium fluorescence between two different neurons. It indicates the strength of the delayed linear relationship between two neurons i and j:

$$\rho_{i\to j}(\tau) = \sum_{t=1}^{T} \frac{x_i(t)x_j(t\ +\ \tau)}{\sqrt{n_i n_j}}$$

where the parameter τ defines the delay of neuron j with respect to neuron i and n_i, n_j are the total number of spikes from neuron i and j respectively [247]. However, these operations are limited to linear interactions and would only reflect the functional connectivity but not the effective connectivity. In contrast, the transfer entropy (TE) would enable the quantification of the effective connectivity. It quantifies the statistical coherence between systems evolving in time and was used to estimate information flow between neurons [248]. TE is defined as the conditional mutual information between the future activity of target neuron j and past activity of source neuron i conditioned by past activity of target neuron j. TE is positive if including information about the spiking activity of a neuron i improves the prediction of the activity of a neuron j beyond the prediction based on the past of the neuron i. The maximum TE and a coincidence index which combines several cross-correlations at different time are computed for each pair using the FluoroSNNAP software [247]:

$$CI_{\,i\to j} = \frac{\sum_{\tau=0}^{r} \rho_{i\to j}(\tau)}{\sum_{\tau=0}^{T} \rho_{i\to j}(\tau)}$$

where CI represents the Coincidence Index, $\rho_{i\to j}(\tau)$ represents the cross-correlation, r is called the coincidence interval which specifies the interval of cross-correlation delays. A large CI indicates a larger reproducibility of correlated spike timing defines the delay of neuron j with respect to neuron i.

In addition to transfer entropy, the Granger causality is used to quantify the effective connectivity. Granger causality test is a statistical hypothesis test which can be used to determine whether one time series is useful in forecasting another. In this context, this test uses the ΔF/F traces to determine if one time series Granger causes another. By definition, a time series X is said to Granger-cause Y, if it can be demonstrated through a series of F-tests on lagged values of X and Y, and that those X values provide statistically significant information about the future values of Y. The Granger causality test is computed using a Matlab toolbox called "Granger causal connectivity analysis" implemented in the FluoroSNNAP software [249].

The network connectivity is then quantified using the mean global connectivity, based on a cross-correlation between pair-wise fluorescence traces, Granger causality and transfer entropy reshuffled 100 times for statistical significance. The mean global connectivity is defined as:

$$Mean\ Global\ Connectivity = \frac{mean\big(sum(A)\big)}{number\ total\ of\ nodes}$$

where A is a binary connectivity matrix, A(i,j) = 1 indicates connection between i and j nodes and A(i,j) = 0 indicates absence of connection. The average of the number of connections across all nodes divided by the total number of nodes is the mean global connectivity. The possible values are: $0 \leq Mean\ Global\ Connectivity \leq 1$. A graph where every node is connected to every other node will have mean global connectivity of 1. Similarly, a graph where nodes are not connected will have mean global connectivity of 0. This analysis was applied to the recorded activity during the 100 ms pulses protocol as described in *section 4.2.1 Temporal and spatial stimulation* (*Figure 20*) in various conditions in the next section of this chapter (see *section 4.3.2 The all-optical assay based on OptoCaMP is sensitive to change in connectivity*).

4.3.2 The all-optical assay based on OptoCaMP is sensitive to change in connectivity

The optical stimulation of a subsection of a neural network expressing OptoCaMP has successfully enabled the characterization of a network's connectivity as demonstrated in the previous section of this chapter (see *section 4.3.1 Method to quantify the neural network connectivity*). Furthermore, quantifying the connectivity of a network could potentially enable studies where the network connectivity is disrupted or enhanced. A crucial step to achieve this aim resides in the demonstration of the sensitivity of this assay to a change in connectivity. To verify that this assay is sensitive to such changes, a proof-of-concept experiment was designed where the all-optical assay using the 100 ms pulses protocol was applied to a subsection of the field of view of dissociated neuronal cultures in four medium conditions (*Table 5*). Briefly, the protocol consisted of ten steps of increasing light intensity of 7mW/cm^2 (±1mW/ cm^2) from 0 to 67 mW/cm^2. The pulse

duration was 100 ms and each pulse was separated by a 5.5 second-interval. This assay consisted of the spatially selective optical excitation of a subsection of the network while the activity of the neighbouring neurons along with the stimulated neurons were monitored.

Condition	Culture medium	Substance added to the recording solution	Expected effect of the condition
BrainPhys	Complete BrainPhys	Tyrode's solution	Supports synaptic function [250]
Neurobasal	Complete Neurobasal		Reduced synaptic communication [250]
BrainPhys + synaptic blockers	Complete BrainPhys	Tyrode's solution + CNQX and D-APV	Block synaptic communication [243]
BrainPhys + caffeine		Tyrode's solution + Caffeine	Increases the excitability of neurons [251, 252]

Table 5 - Summary of the conditions studied. For the BrainPhys and Neurobasal conditions, the dissociated rat cortical neurons were respectively cultured in these complete media (*see section 2.1.2.1 Primary Rat Cortical Neuron Culture*). Experiments for these two conditions were performed in the same Tyrode's recording solution. For the BrainPhys with synaptic blockers and Brainphys with caffeine, neurons were cultures in complete BrainPhys medium. Experiments were performed in Tyrode's solution respectively with the addition of CNQX (6-Cyano-7-nitroquinoxaline-2,3-dione) (2 µM) and D-APV (D(−)-2-Amino-5-phosphonopentanoic acid) (10 µM) or caffeine (1mM).

The first condition represented the control experiment where the rat cortical neurons were maintained in complete BrainPhys medium (see *section 2.1.2.1 Primary Rat Cortical Neuron Culture*). This medium has been recently developed to support *in vitro* neuronal activity such as action potentials and synaptic activity [250]. Aiming to reduce the differences between culture media and *in vivo* brain conditions, the calcium levels in BrainPhys medium were adjusted to be close to those in human cerebrospinal fluid *in vivo* (∼ 1.1 mM) [250]. Additionally, the energetic components in BrainPhys medium

were balanced to provide glycemic levels similar to those reported for the brains of healthy patients (∼2.5 mM) [250]. Furthermore, the osmolarity was set to approximate that of typical human cerebrospinal fluid (∼300 mOsmol/L) [250]. In the second condition, the rat cortical neurons were maintained in complete Neurobasal medium. This medium is a commonly used medium for the maintenance of neuronal cultures *in vitro* which has recently been linked to a reduction of synaptic communication and action potential firing compared to BrainPhys medium [250]. It has been demonstrated that the glucose levels in Neurobasal are at least two to five times higher than those in the brain of hyperglycemic patients [250]. Moreover, it has been shown that the osmolarity of Neurobasal is ∼30% lower than neurophysiological levels (∼220mOsmol/L). Taking these information into consideration, it was expected to observe a reduction in the activity of the non-stimulated neurons in the Neurobasal condition compared to the BrainPhys condition resulting in a decrease of the connectivity. In the third condition, the neurons were maintained in BrainPhys medium and the synaptic blockers CNQX (6-Cyano-7-nitroquinoxaline-2,3-dione) (2 μM) and D-APV (D(-)-2-Amino-5-phosphonopentanoic acid) (10 μM), respectively α-amino-3-hydroxy-5-methyl-4-isoxazolepropionic acid (AMPA) and N-methyl-D-aspartate (NMDA) receptors antagonists were added to the recording solution [243]. This addition modulates excitatory transmission by blocking the activation of postsynaptic ionotropic receptors (NMDA and AMPA) [243]. Therefore, it was expected to observe a reduction in the activity of the non-stimulated neurons with the addition of synaptic blockers when compared to the BrainPhys condition resulting in a decrease in the connectivity. Finally, in the fourth condition, the neurons were maintained in BrainPhys

basal medium and caffeine (1mM) was added to the recording solution. Caffeine is a nonselective adenosine receptor antagonist, acting on A1 and A2A receptor subtypes which has been shown to increase the excitability of neurons [251, 252] and excitatory synaptic transmission [253]. These two adenosine receptors have opposite effects on intracellular cyclic AMP (cAMP) levels. Adenylyl cyclase, an enzyme that synthesizes cAMP from adenosine triphosphate (ATP) is inhibited by the A1 receptors and stimulated by the A2A receptors. Therefore, inhibition of A1 receptors indirectly activates adenylyl cyclase and elevates cAMP levels. Caffeine also affects cAMP levels by inhibiting phosphodiesterase, an enzyme that degrades cyclic nucleotides therefore inhibition of phosphodiesterase reduces the degradation of cAMP. In summary, caffeine can boost cAMP levels by inhibiting either A1 receptors or phosphodiesterase. High levels of cAMP increase the activation and opening of the cyclic nucleotide-gated (CNG) channels resulting in an enhancement of the neuronal excitability. Therefore, caffeine can depolarize neurons and facilitate the firing of action potentials through activation of CNG channels. Therefore, it is expected to observe an increase in the activity of the stimulated neurons in this condition compared to the BrainPhys medium condition. In addition to facilitating action potentials, caffeine may also promote neurotransmitter release by antagonizing A1 receptors, which normally suppress neurotransmitter release at presynaptic sites. Taking this mechanism into consideration, it would be expected to observe an enhancement of the neuronal activity in the non-stimulated neurons compared to the BrainPhys medium condition, which would result in an increase in the connectivity. Therefore, to characterise the activity in each zone and study the quantify the network connectivity in the conditions described above, the 100

ms pulses protocol was applied to a subsection of the field of view as explained in *section 4.2.1 Temporal and spatial stimulation* (*Figure 19*). To compare the neuronal activity in each zone as shown in *Figure 20*, the amplitude of each event was initially collected for individual neurons and the response of all the neurons within the same zone was averaged (*Figure 23*). Briefly, the blue zone contained the stimulated neurons and the zones 1 and 2, respectively green and red, contained the non-stimulated neurons (*Figure 20*). This analysis was performed for each zone and each condition (*Figure 23*). There was no significant difference between the activity of the stimulated neurons in the BrainPhys medium, Neurobasal medium and BrainPhys medium with the addition of synaptic blockers (*Figure 23A*). Additionally, there was no significant difference between the activity of the non-stimulated neurons, in zone 1 (green - *Figure 23B*) and zone 2 (red - *Figure 23C*) in Neurobasal medium and BrainPhys medium with synaptic blockers; however, the neuronal response in these two conditions was significantly decreased compared to the BrainPhys medium condition ($p<0.01$ for zone 1 and $p<0.05$ for zone 2) (*Figure 23B, Figure 23C*). This result agreed with previous studies indicating that synaptic transmission is affected in Neurobasal [250]. Furthermore, this observation can be linked to previous studies showing evidence that L-cysteine, a specific component of Neurobasal, mediates NMDA receptor-dependent excitotoxicity in neurons [254]. Regarding the condition where synaptic blockers were added to the recording solution, as expected, the activity in the non-stimulated neurons was significantly lower than within the BrainPhys condition (*Figure 23B, Figure 23C*). This result confirms the successful modulation of the excitatory transmission with synaptic blockers [243] and demonstrates the capability of this assay to report this effect. In contrast, the addition

of caffeine resulted in a significant higher amplitude compared to the three other conditions in both stimulated (*Figure 23A*) and non-stimulated neurons (*Figure 23B, Figure 23C*). These observations correlate with previous studies which have shown that caffeine enhances the excitability of neurons and excitatory synaptic transmission ($p<0.0001$) [251, 253] and demonstrates the capability of this assay to report this effect.

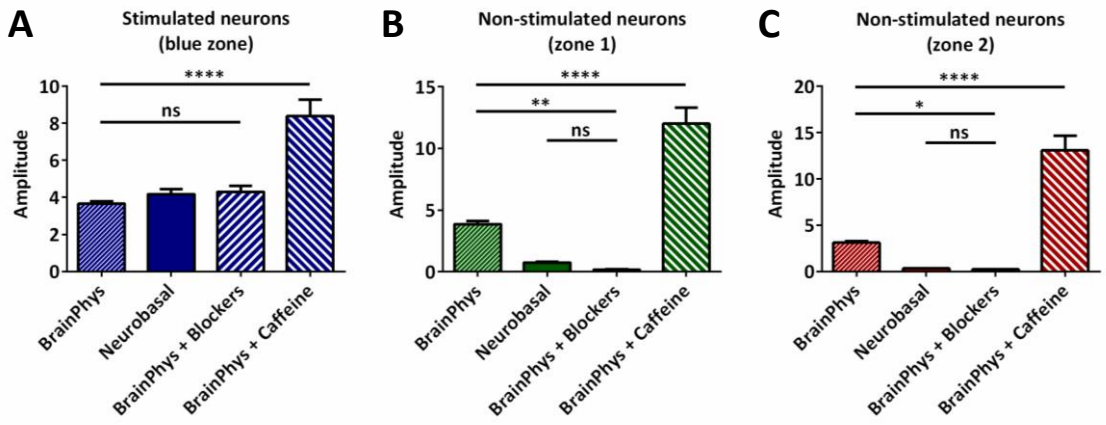

Figure 23 - Average amplitude in various conditions for each zone - (A–C) Average of the amplitude of the calcium events of multiple individual neurons in the same zone ± s.e.m.: stimulated neurons (A), non-stimulated neurons in zone 1 (B), and zone 2 (C) during the 100 ms pulses protocol in four conditions: BrainPhys complete medium (BP), complete Neurobasal medium (NB), synaptic blockers (BP + blockers) and caffeine (BP + caffeine) (n=3 independent cell culture experiments for each condition; one-way ANOVA, (A) $F(3,36) = 20.16$, $P < 0.0001$; (B) $F(3,36) = 66.31$, $P < 0.0001$ (C) $F(3,36) = 59.77$, $P < 0.0001$; (A–C) followed by Tukey's multiple comparisons test: ns=non-significant, $*P < 0.05$, $**P < 0.01$, $****P < 0.0001$).

As described in the previous section of this chapter, the software FluoroSNNAP enables the characterisation of the temporal dynamics of calcium activity occurring within individual neurons to then quantify the network connectivity using the mean global connectivity based on a cross-correlation, Granger causality and transfer entropy (see section *4.3.1 Method to quantify the neural network connectivity*). This analysis results in a map showing the connections between the neurons represented with red lines.

Additionally, each neuron is assigned an identification number which can further be used to describe the connections between each neuron on a colour map. The connectivity and colour maps for the BrainPhys medium (*Figure 24A*) and BrainPhys medium with caffeine (*Figure 24D*) show connections in the whole network. In contrast, neuronal activity was only observed within the zone optically stimulated for the Neurobasal medium (*Figure 24B*) and BrainPhys medium with synaptic blockers (*Figure 24C*). Additionally, the quantification of the mean global connectivity revealed a significantly lower mean global connectivity for the neurons cultured in Neurobasal medium compared to neurons cultured in the BrainPhys medium ($p<0.0001$) (*Figure 24E*). The addition of caffeine significantly enhanced the mean global connectivity compared to the BrainPhys medium condition ($p<0.0001$) (*Figure 24E*) while the addition of synaptic blockers significantly decreased the mean global connectivity compared to the BrainPhys medium condition ($p<0.0001$) (*Figure 24E*). These results demonstrate that the quantification of the mean global connectivity using this assay reflects the previously published results in regard to the synaptic connections in Neurobasal [250], synaptic blockers [243] and caffeine conditions [251]. Overall, these experiments highlight the sensitivity of the OptoCaMP all-optical assay and its potential application for *in vitro* studies aiming to evaluate the neuronal activity in conditions where the neuronal connectivity is enhanced or decreased. These encouraging results bring the promise to enable the study of more complex pharmacological conditions and how diseased neural networks communicate and respond to a potential therapeutic agent [255].

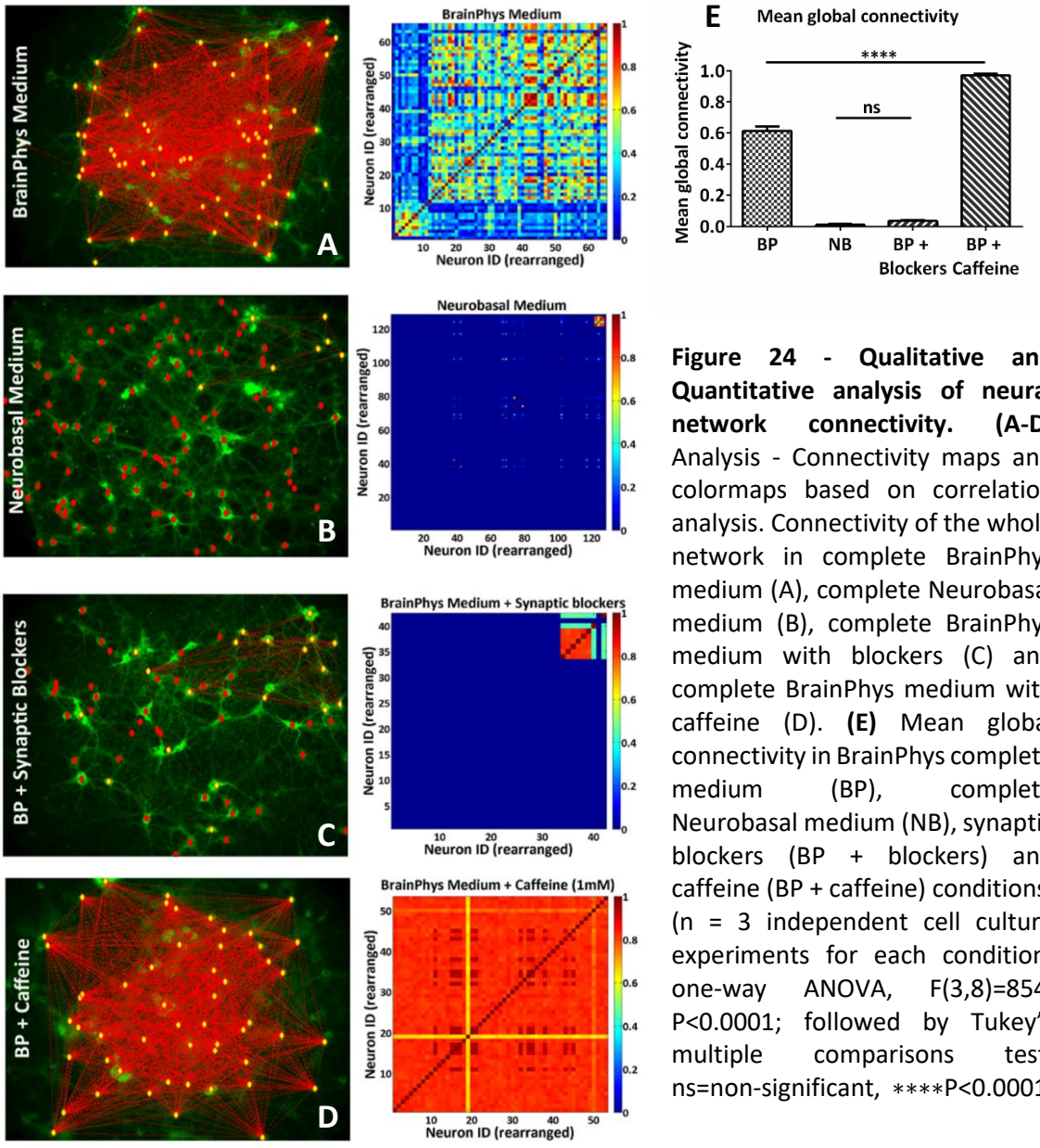

Figure 24 - Qualitative and Quantitative analysis of neural network connectivity. (A-D) Analysis - Connectivity maps and colormaps based on correlation analysis. Connectivity of the whole network in complete BrainPhys medium (A), complete Neurobasal medium (B), complete BrainPhys medium with blockers (C) and complete BrainPhys medium with caffeine (D). **(E)** Mean global connectivity in BrainPhys complete medium (BP), complete Neurobasal medium (NB), synaptic blockers (BP + blockers) and caffeine (BP + caffeine) conditions. (n = 3 independent cell culture experiments for each condition; one-way ANOVA, $F(3,8)=854$, $P<0.0001$; followed by Tukey's multiple comparisons test: ns=non-significant, ****$P<0.0001$.

4.3.3 OptoCaMP in hiPSC-derived neurons and future directions

Although the results presented in the previous sections of this chapter demonstrate the potential of the all-optical assay and the OptoCaMP, previous studies have demonstrated the challenge of the translation from murine dissociated neuronal cultures to hiPSC-derived neurons [256]. A recent publication regarding the optogenetic tool Optopatch2 presented in Chapter 3 (*see section 3.2.1 The optogenetic tool Optopatch2*) highlighted the challenge of the expression of Optopatch2 as bicistronic vector in hiPSC-derived neurons. As a method to overcome this limitation, the two components of Optopatch2 (CheRiff-eGFP and QuasAr2-mOrange2) were package in two separate lentiviruses under the same promoter (CamKIIα). This approach improved expression level of these proteins in hiPSC-derived neurons. Therefore, a crucial step in the successful translation of the all-optical assay presented in Chapter 4 resided firstly in the assessment of the successful expression OptoCaMP in hiPSC-derived neurons.

4.3.3.1 OptoCaMP is successfully expressed in iCell GlutaNeurons

The lentiviral delivery optimisation adopted for this translation was based on the approach presented in *section 3.3.2.1 Lentiviral delivery*. The expression of OptoCaMP was firstly assessed in a commercial hiPSC-derived neurons line called iCell GlutaNeurons from Cellular Dynamics (*see section 2.1.3.2 iCell® GlutaNeurons*). This cell line has been specifically designed with ≥90% pure population of primarily glutamatergic human neurons. Therefore, OptoCaMP being driven by the CamKIIα promoter is expected to successfully be expressed. The plating density (2 x 10^5/cm^2) and the virus concentration (1:60) were similar to the ones used for the rat cortical neurons. The

toxicity of the lentiviral transduction and the OptoCaMP was tested with the LDH assay using the same method previously described in *section 3.2.2 OptoCaMP and Optopatch2 are not toxic for Rat Primary Cortical Neurons*. Similarly to the rat cortical neurons, this assay did not show any toxicity of the construct via lentiviral transduction (*Figure 25*). Furthermore, the expression of OptoCaMP was assessed via fluorescence since CheRiff and jRCaMP1b are respectively tagged with enhanced Green Fluorescent Protein (eGFP) and mRuby (*Figure 26*). The fluorescence images confirmed the successful expression of OptoCaMP as a bicistronic plasmid driven by CamKIIα promoter in glutamatergic neurons derived from hiPSC.

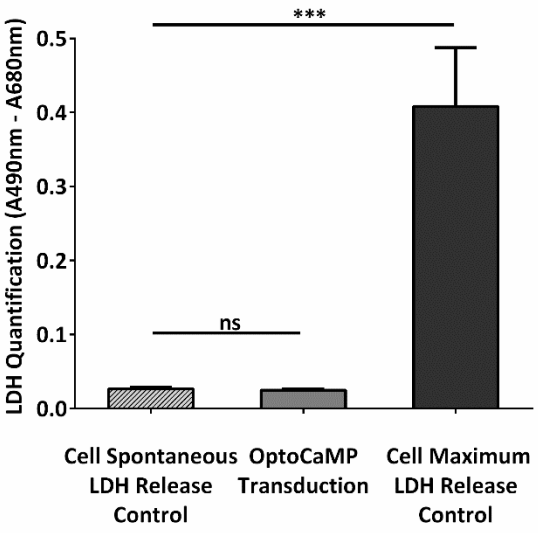

Figure 25 - Lentiviral transduction of OptoCaMP in iCell GlutaNeurons. Quantification of lactose dehydrogenase levels (LDH) in live iCell GlutaNeurons 6 days after transduction with the OptoCaMP. The lentivirus delivery did not show any significant difference between the cells non-transduced (cell spontaneous LDH release control) and the cell transduced with OptoCaMP. (n=3 independent cell culture experiments, one-way ANOVA, $F(2,6) = 68.47$, $P < 0.0001$; followed by Tukey's multiple comparisons test: OptoCaMP transduction versus Cell spontaneous LDH release control, $P = 0.991$; Cell maximum LDH release control versus Cell spontaneous LDH release control, $***P < 0.0001$; Cell maximum LDH release control versus OptoCaMP transduced, $***P < 0.0001$).

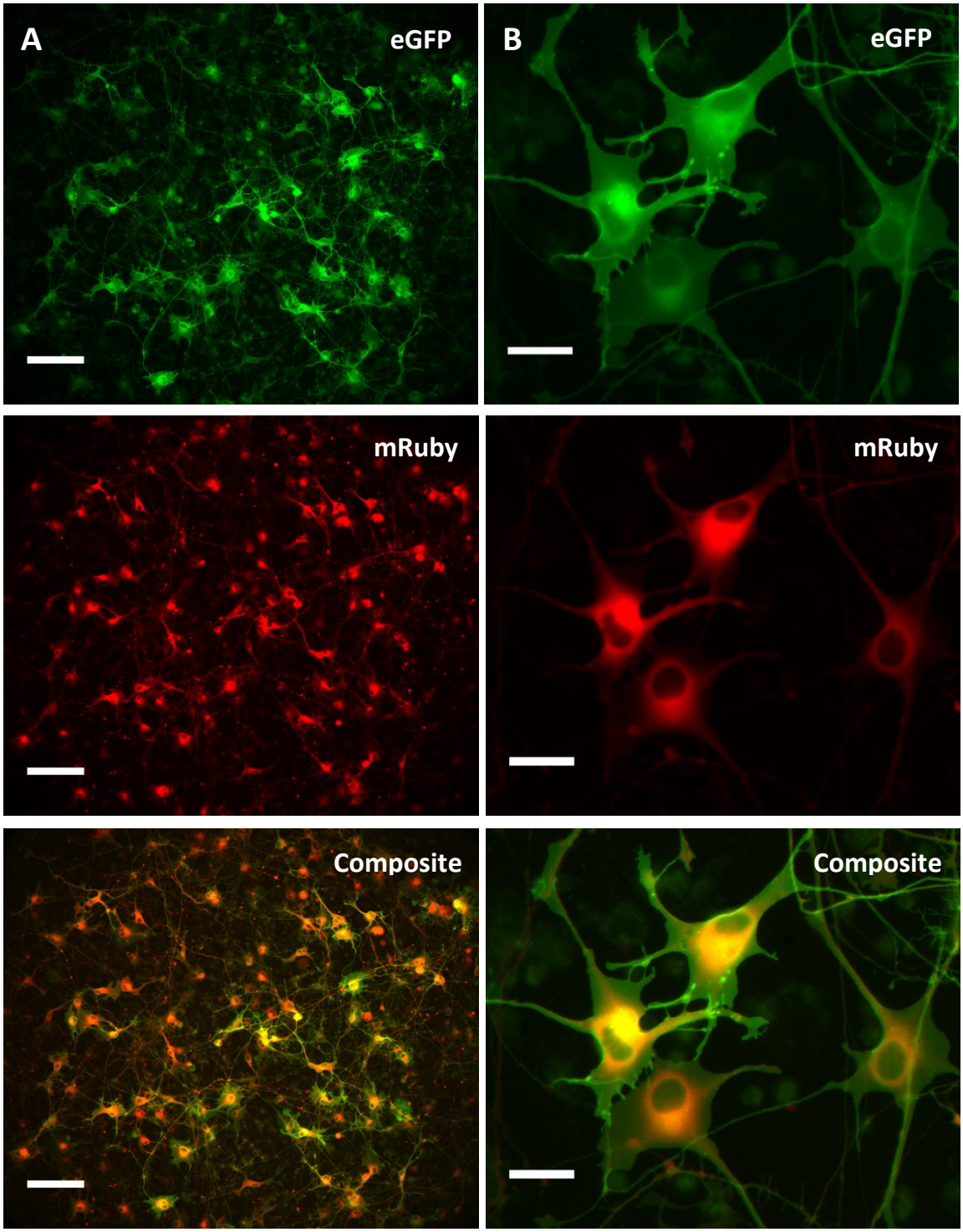

Figure 26 - OptoCaMP expression via lentiviral transduction in iCell GlutaNeurons. (A) Single channels and merged fluorescence images of iCell GlutaNeurons expressing OptoCaMP at 21 days *in vitro,* 7 days post-transduction: CheRiff-eGFP is displayed in green and mRuby based GECI jRCaMP1b in red. Scale bar 100 µm. 20X Magnification **(B)** Single channels and merged fluorescence images of iCell GlutaNeurons expressing OptoCaMP at 21 days *in vitro,* 7 days post-transduction: CheRiff-eGFP is displayed in green and mRuby based GECI jRCaMP1b in red. Scale bar 30 µm. 60X Magnification.

4.3.3.2 All-optical stimulation and recordings in iCell GlutaNeurons

Following the assessment of the successful expression of OptoCaMP in the iCell GlutaNeurons at three weeks *in vitro*, the all-optical assay previously described was performed (see *section 4.2.1 Temporal and spatial stimulation*). Briefly, the protocol consisted of ten steps of increasing light intensity of 7mW/cm^2 (±1mW/ cm^2) from 0 to 67 mW/cm^2. The pulse duration was 100 ms and each pulse was separated by a 5.5 second-interval. This assay consisted of the spatially selective optical excitation of a subsection of the network while the activity of the neighbouring neurons along with the stimulated neurons were monitored. As described in the previous section of this chapter, the software FluoroSNNAP enabled the characterisation of the temporal dynamics of calcium activity occurring within individual neurons to then quantify the network connectivity, using the mean global connectivity based on cross-correlation, Granger causality and transfer entropy (*see section 4.3.1 Method to quantify the neural network connectivity*) (*Figure 27*). The analysis showed activity of the stimulated and non-stimulated (*Figure 27C*) thus enabling the quantification of the connectivity (*Figure 27D*). Additionally, this analysis resulted in the creation of a map showing the connections between the neurons represented with red lines (*Figure 27D*). This experiment successfully demonstrated the use of OptoCaMP with the all-optical assay of a subsection of a neural network formed by the iCell GlutaNeurons. This preliminary experiment opens new avenues for the investigation of connectivity in hiPSC-derived neurons and Alzheimer's disease models.

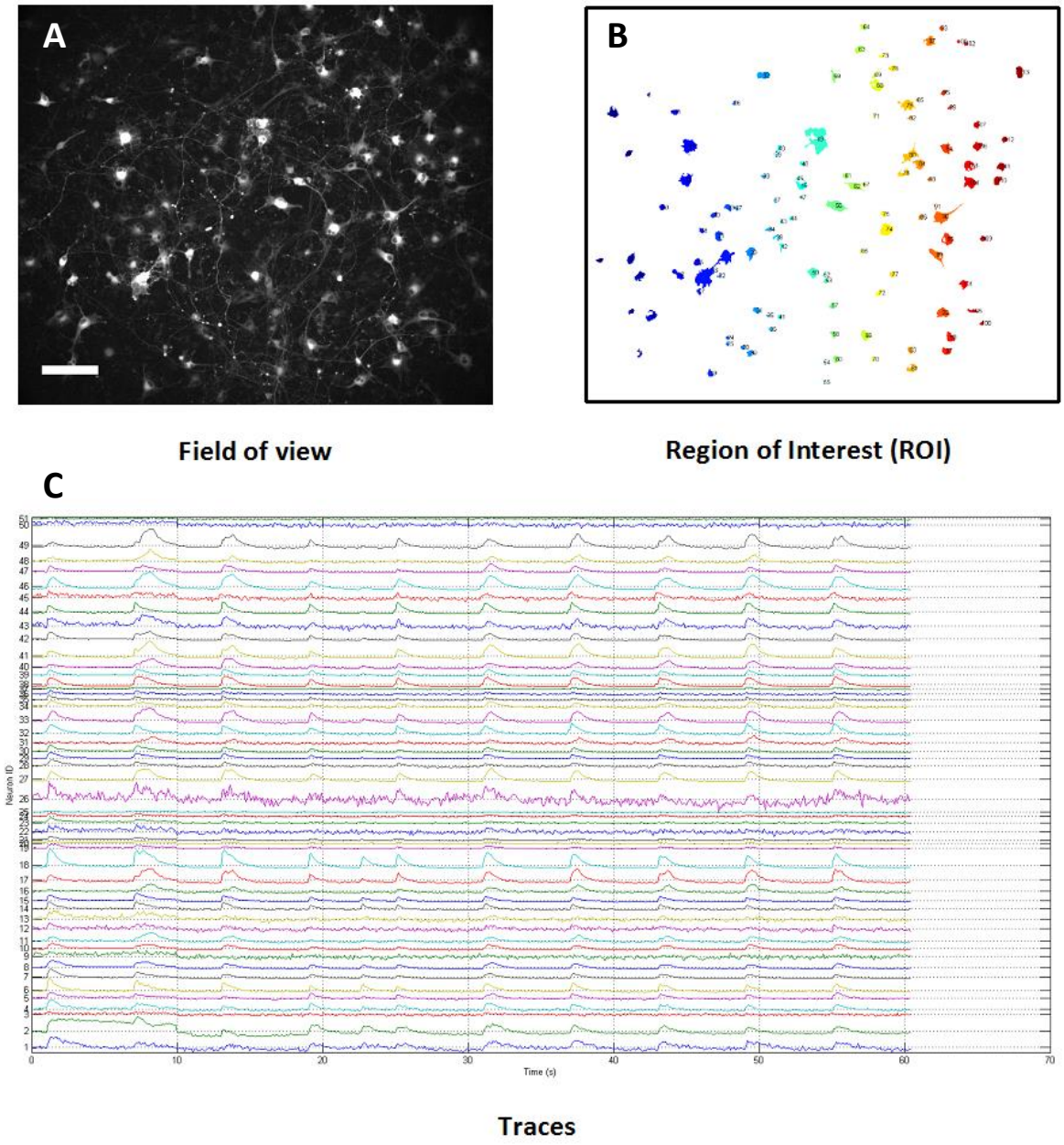

Figure 27 - Analysis iCell GlutaNeurons. (A) Field of view recorded containing the iCell GlutaNeurons expressing OptoCaMP. Scale bar 100 µm. (B) Segmentation of (A). (C) Traces of single-cell activity. (D) Connectivity map of the field of view. (E) Mean Global connectivity of the iCell GlutaNeurons (n=3).

4.3.3.3 Future directions and challenges

With this aim in mind, Dr Young-Pearse at Harvard Medical School shared two hiPSC-derived neurons cell lines with a familial Alzheimer's disease (fAD) model and a control cell line. The first line was derived from a father and daughter with a fAD mutation (APPV717I mutation, London mutation) which will further be referred as "fAD" [257]. Additionally, the Clustered Regularly Interspaced Short Palindromic Repeats-associated protein 9 (CRISPR-Cas9) technology was used to correct this mutation to establish the control cell line [1]. Briefly, the CRISPR system relies on the action of Cas9, a protein that has two endonuclease domains capable of cleaving the DNA: a double strand brake (DSB) is generated as one endonuclease cleaves the complementary DNA strand and the other cleaves the non-complementary DNA strand. In order to recognise, bind and then cleave the DNA target in a highly specific manner, Cas9 has to be driven by a guide RNA (gRNA). The gRNAs are sequences of about 20 nucleotides that perfectly match the sequence of the DNA target which in turn has to contain to its end a short-conserved sequence called Protospacer Adjacent Motif (PAM). This technology was used to generate an isogenic hiPSC line to fAD with correction of the APPV717I mutation, which will further be referred as "fAD^{corr}". Dr Young-Pearse's group has examined Aβ38, 40 and 42 levels in the fAD and fAD^{corr} lines. To summarise, this analysis demonstrated an increased ratio of Aβ42/40 which is mainly attributable to an increase in Aβ42 with no change or little effect on Aβ40 levels (*Figure 28*). Taking this into consideration, these two cell lines were selected for the application of the OptoCaMP and the all-optical assay in order to investigate connectivity in an Alzheimer's disease and control models.

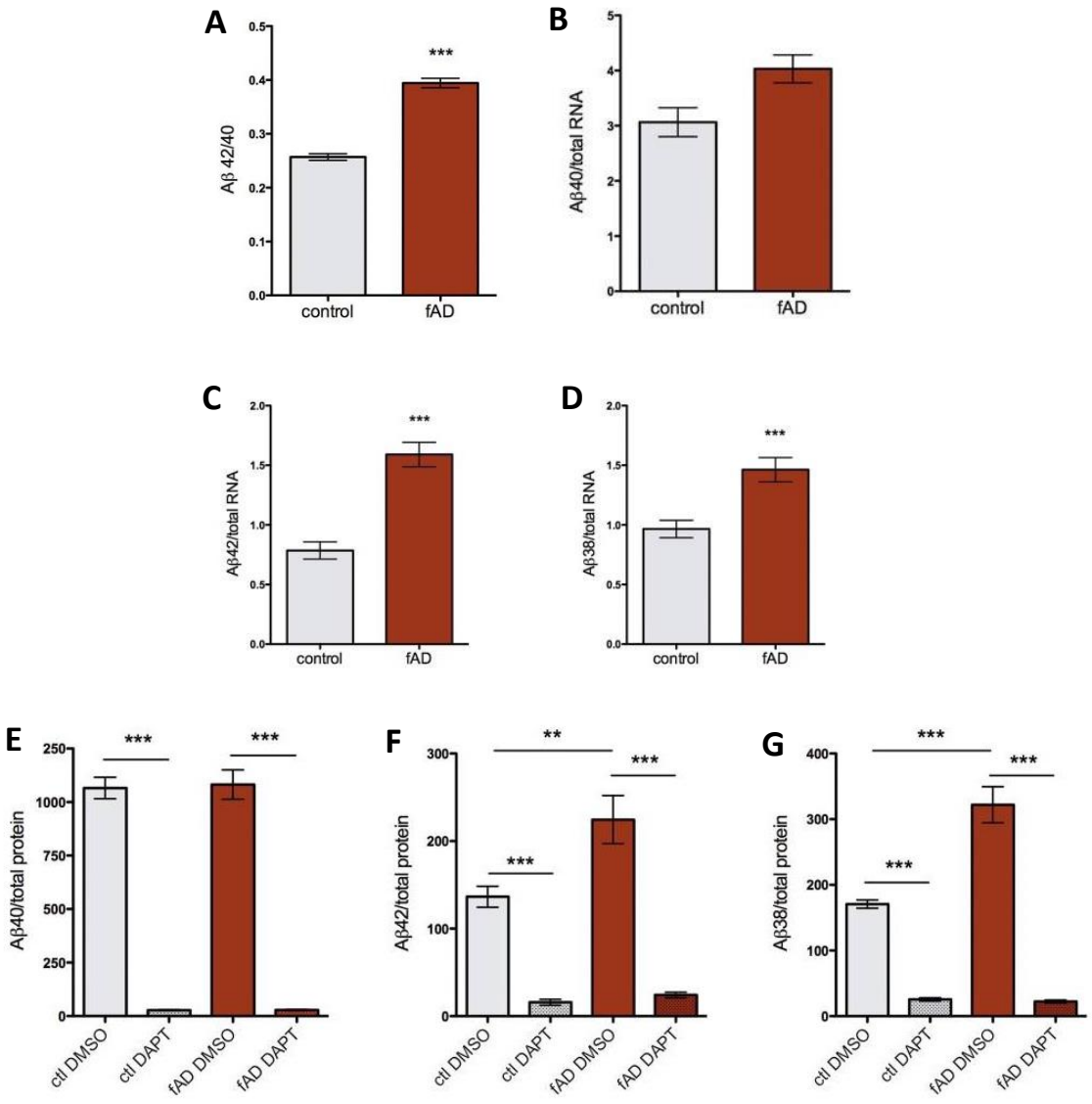

Figure 28 - Levels of Aβ in hiPSC-derived neurons - FAD mutation (APPV717I) in forebrain neuronal cells leads to increased Aβ42 and Aβ38 production. Control (fAD^{corr} line where APPV717I mutation was corrected using CRISPR-Cas9) and fAD iPSC lines were differentiated for 40–50 days to neuronal fates. Media conditioned on the cells for the final 48h were collected, and Aβ 38, 40 and 42 were detected in a single well using a multiplex ELISA (MesoScale Discoveries). Following collection of media, cells were lysed and RNA collected for parallel analyses of markers of differentiation. Data are shown for control (fAD^{corr} line) and APPV717I (fAD) (A-D). In (E–G), day 40 neurons were treated with vehicle or DAPT (5 µm) for the final 48 h of differentiation (n = 4–5 for each condition). Two-tailed t-tests were performed, **P < 0.01; ***P < 0.001. Error bars = SEM. Data normalized to RNA in (B-D) and total protein in (E-G). Figure adapted from *The familial Alzheimer's disease APPV717I mutation alters APP processing and Tau expression in iPSC-derived neurons, [1].*

The hiPSC-derived neurons fAD and fAD^{corr} were generated via overexpression of the transcription factor Neurogenin-2 [258]. The hiPSC are initially lentivirally transduced with the plasmids pLV-TetO-hNGN2-Puro and pLV-TetO-FUW-eGFP resulting in the downregulation of the pluripotency factors and the initiation of the neuronal transcriptional program [258]. The Tet-ON system consists of two components: a constitutively expressed transcriptional activator protein responsive to doxycycline (dox) (reverse tetracycline transactivator [rtTA]), and an inducible promoter regulated by rtTA (Tet-responsive element) that drives expression of the transgene [258]. Therefore, the hiPSC-derived neurons fAD and fAD^{corr} express eGFP during the differentiation which may interfere the assessment of the successful expression of FCK-OptoCaMP since CheRiff is also tagged with eGFP. To confirm the successful expression of FCK-OptoCaMP, it is essential to assess the expression of jRCaMP1b tagged with mRuby. To achieve this, the fAD and fAD^{corr} were co-cultured with primary rat cortical astrocytes in our laboratory (*see sections 2.1.2.2 Primary Rat Cortical Astrocytes Culture and 2.1.3.1 Healthy and Alzheimer's disease hiPSC-derived neurons*). The OptoCaMP was lentivirally transduced in these two cell lines and its expression was assessed via fluorescence. Although the cultures were successfully produced, and the iPSC-derived neurons developed networks as shown in *Figure 29 A-D*, there was no expression in the red channel of jRCaMP1b post-transduction (*Figure 29F-G*). Therefore, the all-optical assay described in the previous chapters were not applicable. This observation raised the question of the excitatory character of the neuronal population which could be further confirmed or refuted by looking at the expression of the vesicular transporters of glutamate (vGlut) via immunofluorescence [259]. This work requires further

investigation however, to overcome the limitation of the choice of promoter, a hiPSC stable cell line expressing OptoCaMP could also potentially be established thus opening new avenues to the study of neural network formation and maturation (*see section 4.4 Discussion*).

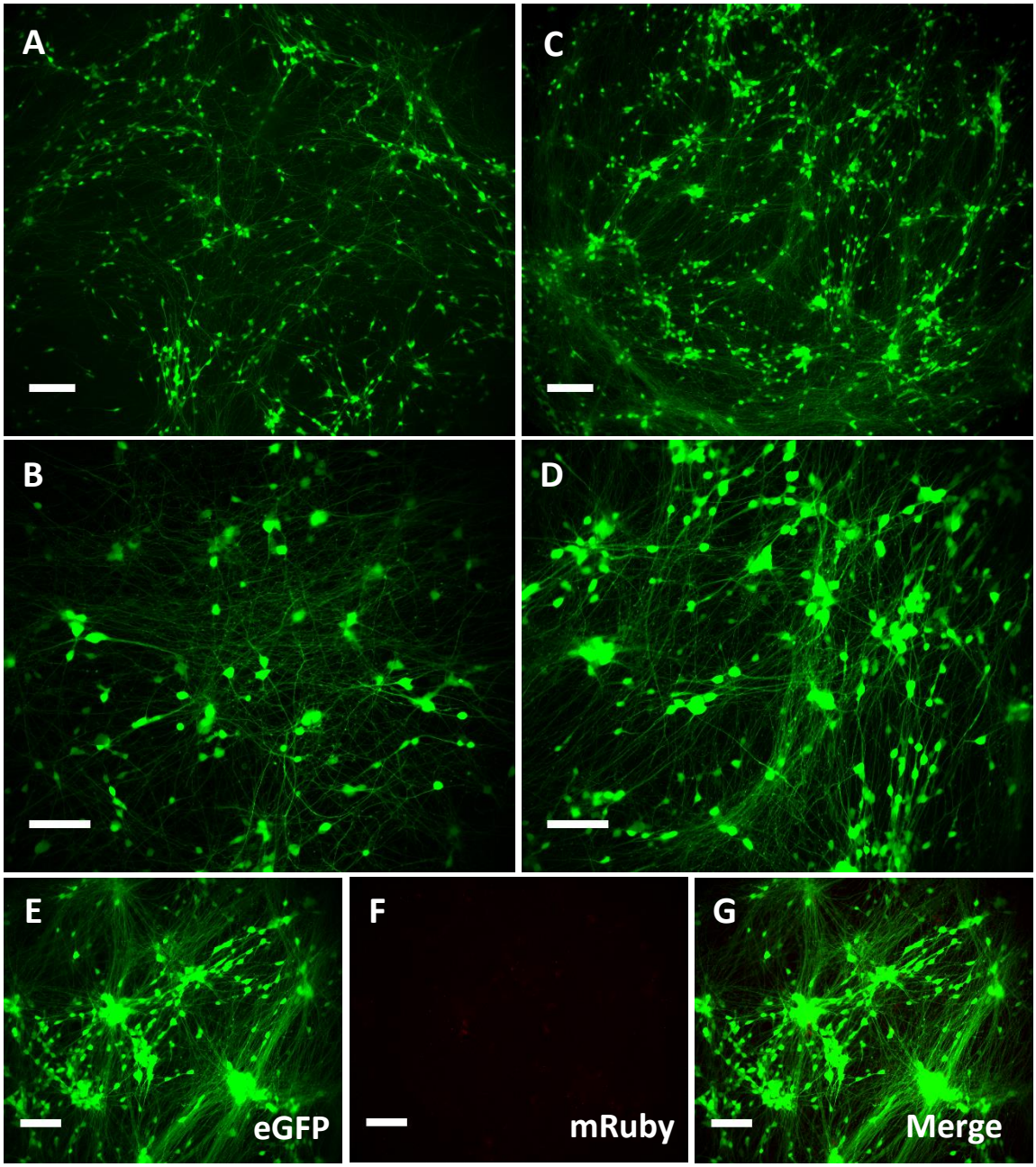

Figure 29 - hiPSC-derived neurons at four weeks *in vitro*. Successful culture of the hiPSC-derived neurons (fAD and fAD^{corr}). **(A-B)** Fluorescent images of the GFP reporter of the fAD line. **(C-D)** Fluorescent images of the GFP reporter of the fAD^{corr} line. **(A, C)** 10X magnification, scale bar 120 µm. **(B, D)** 20X magnification, scale bar 100 µm. **(E)** fAD line at DIV 24, 7 days post-transduction with FCK-OptoCaMP. Green Channel. **(F)** fAD line at DIV 24, 7 days post-transduction with FCK-OptoCaMP. Red Channel. **(G)** fAD line at DIV 24, 7 days post transduction with FCK-OptoCaMP. Merge image of (E) and (F). **(E-G)** 20X magnification, scale bar 100 µm.

4.4 Discussion

Despite successfully allowing the simultaneous stimulation and recording of the activity of a neural network with a single-neuron readout as shown in Chapter 3, the "whole-field of view stimulated and recorded" configuration is not appropriate for neural network studies as it gives insight into multiple neurons' activity but not connectivity. Importantly, one of the most fundamental features of a neural network is its connectivity since the single neuron activity is not due only to its intrinsic properties but especially to the direct or indirect influence of other neurons [242]. Therefore, in Chapter 4, the focus was placed on the development of a variation of the all-optical assay based on the OptoCaMP which could enable the study of the network connectivity. This variation of the all-optical assay consisted of the spatially selective optical excitation of a subsection of the network while the activity of the neighbouring neurons along with the stimulated neurons, are monitored. Furthermore, to select a protocol to study neural networks, various protocols were applied with pulses of 10 ms, 100 ms, 250 ms and 500 ms duration (*Figure 20*). This analysis demonstrated that the 10 ms stimulation evoked similar calcium events in the stimulated and non-stimulated neurons for stimuli intensities from 0 to 44 mW/cm^2 but not above 44mW/cm^2, showing that this protocol enables stimulation and reporting of the neural network activity, but also hinting at potential difficulties with reproducibility at higher light intensities (*Figure 20*). Although the activity of the stimulated neurons significantly increased with the pulse duration, there was no significant difference for the non-stimulated neurons during the 10ms, 100ms and 250 ms protocol (*Figure 20*). This finding implicates that longer stimuli do not result in higher calcium activity, but it also suggests that the spread of excitation

does not depend on the stimuli up to 250 ms pulses duration (*Figure 20*). In contrast, the activity of the non-stimulated in zone 2 (red) was lower to zone 1 (green) during the 500 ms protocol suggesting that strong stimulus may be linked to excessive glutamatergic excitation of neurons which can cause excitotoxicity, resulting in damage to, and the eventual death of the neuron (*Figure 20*) [244, 260]. This affects the spread of excitation resulting in the abolition of calcium events in the network, a situation that would impede the study of network connectivity. These observations together with the possibility to increase the throughput, resulted in the selection of the 100 ms pulses as the optimal pulse duration in this system.

In the first part of this chapter, the use of OptoCaMP along with the stimulation of a subsection of a neural network enabled the quantification of a network's connectivity. This technique was applied to study connectivity in various conditions where connectivity is supposedly reduced or enhanced. As shown in *Figure 24*, the addition of caffeine and synaptic blockers respectively significantly increased and decreased the mean global connectivity as compared to the BrainPhys medium control condition. These results agreed with the documented increase of the neuronal excitability with caffeine [251, 252] and depression with the addition of synaptic blockers [243]. Additionally, the mean global connectivity for the Neurobasal condition was significantly lower than the BrainPhys medium which also agrees with previous published findings showing that BrainPhys supports optimal action potentials and synaptic activity, while Neurobasal medium reduces synaptic communication and action potential firing [250]. Overall, these experiments highlighted the sensitivity of the OptoCaMP all-optical assay and its potential application for *in vitro* studies aiming to evaluate the neuronal activity

in conditions where the neuronal connectivity is enhanced or decreased. These encouraging results bring the promise to enable the study of more complex pharmacological conditions and how diseased neural networks communicate and respond to a potential therapeutic agent [255]. With this aim in mind, it has naturally led onto the translation of this assay to human iPSC-derived neurons. The lentiviral transduction of OptoCaMP was initially performed in a commercial line called iCell GlutaNeurons. This cell line has been specifically designed with ≥90% pure population of primarily glutamatergic human neurons derived from hiPSC. As shown in *Figure 26*, the fluorescence images confirmed the successful expression of OptoCaMP as a bicistronic plasmid driven by CamKIIα promoter in glutamatergic neurons derived from hiPSC. Following the expression of OptoCaMP, the all-optical assay to study network activity was applied to the glutamatergic neurons derived from hiPSC. As shown in *Figure 27*, this assay showed the activity of the stimulated and non-stimulated neurons thus enabling the quantification of the connectivity of the network. This preliminary data demonstrated the successful use of OptoCaMP with the all-optical assay of a subsection of a neural network formed by the iCell GlutaNeurons. Moreover, this assay could potentially be used to assess the maturity of the culture by looking at the ability of iPSC-derived neurons to connect with other cells in the system and if these synapses are functional thus enabling the study of the network formation. Importantly, when modeling neurological disorders, a co-culture system of iPSC-derived neurons and other cell types would mimic more accurately the complexity of *in vivo* conditions. In particular, astrocytes have been shown to increase the number of mature, functional synapses and are required for synaptic maintenance *in vitro* [261]. A recent publication has further

demonstrated this improvement with the co-culture of astrocytes together with the iCell GlutaNeurons [262]. Although the expression of OptoCaMP was successful in glutamatergic human neurons derived from hiPSC, there was no expression of OptoCaMP in the fAD and fAD^{corr} hiPSC-derived neurons established in Dr Tracy Young-Pearse's group at Harvard Medical School. This observation raised the question of the excitatory character of the neuronal population which requires further investigation. However, to overcome the limitation of the promoter, a hiPSC stable cell line expressing OptoCaMP could potentially be established based on the same approach using the Tet-ON, a tetracycline-inducible gene expression system [263]. Following the forward reprogramming of the hiPSC into neurons, the expression of OptoCaMP would be induced with the addition of doxycycline, a tetracycline analogue. This system would allow the recording of the neural network activity and connectivity at multiple time points to further enable the study of neural network formation and maturation.

Chapter 5 - Summary, conclusions and future directions

Chapter 5 - Summary, conclusions and future directions

Functional studies of biological neural networks are fundamental to our understanding of brain activity, to investigate how these networks are altered in brain disorders, and to help develop new treatments [223]. Moreover, the investigation of connectivity is crucial to understanding how neurons and neural networks process information and how this is affected in neurodegenerative diseases such as Alzheimer's disease [30]. Studies have shown evidence that Aβ oligomers reduce glutamatergic synaptic transmission by decreasing the number of surface of AMPA and NMDA receptors [31]. Therefore, to explore neural networks, it is critical to understand the activity of multiple neurons and how they communicate with each other. To achieve this goal, it is essential to use tools enabling simultaneous stimulation and recording from a large population of neurons with a single-cell readout. Although electrophysiology facilitates both stimulation and recording of individual neurons with high temporal resolution this technique is invasive, labour intensive and exhibits limitations when one wishes to characterise a highly heterogeneous neuronal population [101]. As a means to overcome the limitations of the invasiveness and the low throughput of electrophysiology, multi-electrode arrays (MEAs) have been developed with the use of arrays of extracellular electrodes [108, 110]. Despite the fact that MEAs enable the stimulation and recording from multiple neurons simultaneously, the neuronal activity is characterized by triangulating the signal through multiple recording points thus impairing the quantification properties of individual neurons [108, 110]. Considering the limitations of the commonly used techniques, it appears that there is a need for a novel approach which would enable large scale functional characterization of neurons with

single-cell readout to elucidate the workings of both healthy and diseased neuronal populations. To answer this need, optogenetics, an emerging technology which benefits from the synergy of optical and genetic techniques, enables the optical stimulation of specific neuronal populations with high temporal and spatial resolution [101]. Optogenetics uses light-gated ion channels to manipulate neuronal activity and can be combined with genetically encoded voltage indicators (GEVIs) and calcium indicators (GECIs). This approach enables an all-optical system to stimulate and record the neuronal activity in a contact-free manner with a single-cell resolution thus overcoming the limitations previously described [3, 107]. The first all-optical approach combining a channelrhodopsin variant and a GEVI was developed by the Cohen laboratory at Harvard University [142]. As described in Chapter 3, despite successfully enabling an all-optical interrogation and recording of neuronal activity, elucidating the inner workings of neuronal circuits at network level with the Optopatch2 remains challenging. In fact, the limitation of the Optopatch2 to report the activity of multiple cells simultaneously stems from the low brightness of the GEVI and the kinetics of the millisecond scale neuronal electrical activity. In addition, the complexity of the imaging setup required to image multiple cells simultaneously limits the throughput of this technique. In contrast, one of the main advantages of calcium imaging stems from the larger magnitude and slower kinetics of these events compared to action potentials. Therefore, a possible strategy to increase the throughput consists in imaging the resulting changes in the intracellular calcium concentration using GECIs [176]. With this aim in mind, a novel optogenetic called OptoCaMP was developed in this thesis project. As presented in Chapter 3, OptoCaMP has been designed as a combination of the light-gated ion channel CheRiff

with the GECI jRCaMP1b. OptoCaMP was successfully expressed as a bicistronic plasmid driven by CamKIIα promoter via lentiviral transduction in rat cortical neurons *in vitro* and human iPSC-derived glutamatergic neurons as demonstrated in Chapters 3 and 4. Importantly, the integrity of the cell membrane was not affected by OptoCaMP nor the lentiviral transduction. Additionally, the lack of spectral overlap between the optogenetic excitation and jRCaMP1b emission wavelengths enabled the simultaneous stimulation and recording of evoked calcium events in dissociated neuronal cultures *in vitro* with a single-neuron readout as shown in Chapter 3. Importantly, the development of novel technologies requires the characterisation of the system. Therefore, the first steps of this project focused on the characterisation of OptoCaMP at various pulse duration and intensities of blue light stimuli. The characterisation of OptoCaMP in Chapter 3 demonstrates the high sensitivity of the channelrhodopsin variant used in OptoCaMP and emphasizes a preferable use of low range stimuli intensities which comes with the advantage to reduce the risk of phototoxicity and photobleaching. Moreover, the recording of multiple cells simultaneously is a crucial aspect as it increases the throughput aspect of an all-optical system. Indeed, this capability represents a considerable advantage compared to the Optopatch2. Therefore, the capability of OptoCaMP to enable simultaneous optical stimulation and calcium recording of multiple neurons simultaneously with a single-cell readout opens new avenues for the study of disease models and drug screening.

One of the most fundamental features of a neural network is its connectivity since a single neuron's activity is not due only to its intrinsic properties but also to the direct or indirect influence of other neurons [242]. Consequently, the "whole-field of view

stimulated and recorded" configuration is not appropriate for neural network studies as it gives insight into multiple neurons activity but not connectivity. With this aim in mind, a variant of the all-optical assay was developed and presented in Chapter 4. This variation of the all-optical assay consisted of the spatially selective optical excitation of a subsection of the network while the activity of the neighbouring neurons along with the stimulated neurons are monitored. Various pulses duration and stimuli intensities were used to characterise the assay and the analysis together with the possibility to increase the throughput, resulted in the selection of the 100 ms pulses as the optimal pulse duration in this system. This assay allowed the investigation of the spread of excitation in the studied network thus allowing quantification of network connectivity. Furthermore, this assay was applied in conditions where the connectivity is supposedly enhanced or reduced and demonstrated its sensitivity to a change in connectivity. To fully unravel the potential of this all-optical assay and resolve single action potentials, this system could potentially be combined with the GEVI QuasAr2. However, this system combining all-optical electrophysiology and calcium imaging would still require advances in microscopy [264]. In contrast, OptoCaMP could be combined with multi-electrode arrays (MEAs) for a complete understanding and characterisation of the network studied [265].

Regarding the biological neural network studied and drug screening platforms, a major issue resides in the fact that human disease models are not available. Genetically engineered animal models have contributed to our progress allowing testing of different therapeutic strategies but the construction of models that can accurately recapitulate a human pathology remains challenging. Due to species differences, there is a debate as

to whether these systems are reliable and fully reflect the key aspects of human diseases [71]. However, the induced pluripotent stem cells technology [76] offers unprecedented ways to model diseases with the development of a wide range of disease-specific iPSC from patients with neurodegenerative diseases [89]. Somatic cells from patients with neurodegenerative diseases have been reprogrammed into induced pluripotent stem cells and differentiated into disease-relevant cell types in two-dimensional (2D) models [75, 266, 267] and more physiologically relevant three-dimensional (3D) models thus opening new avenues for disease modelling [91]. In Chapter 4, this assay was successfully applied to neural network formed by human iPSC-derived glutamatergic neurons which bring the great promise to enable the study of how connectivity is affected in diseased neural networks. Additionally, a co-culture system of iPSC-derived neurons and other cell types such as astrocytes would mimic more accurately the complexity of *in vivo* conditions and would be compatible with the OptoCaMP under CamKIIα promoter since it would restrict its expression to glutamatergic neurons. Considering that one of the current challenges in the iPSC technology resides in the maturity of the neurons, studying the ability of iPSC-derived neurons to connect with other cells in the system and if these synapses are functional would enable the study of the network formation. With this aim in mind, a hiPSC stable cell line expressing OptoCaMP could potentially be established using the Tet-ON, a tetracycline-inducible gene expression system [263]. Following the forward reprogramming of the hiPSC into neurons, the expression of OptoCaMP would be induced with the addition of doxycycline, a tetracycline analogue. This system would allow the recording of the neural network activity and connectivity at multiple time points to further enable the

study of neural network formation and maturation. Along with the development of 3D models *in vitro*, advances in imaging have been achieved with the development of light-sheet microscopy [268] and swept confocally-aligned planar excitation (SCAPE) microscopy [269] for volumetric imaging with sub-cellular resolution and high speed [270]. The use of the all-optical assay combined with the iPSC technology in 2D and 3D cellular models, SCAPE and light-sheet microscopy bring the promise to greatly improve the success and efficiency of study of neurodegenerative diseases and drug screening platforms [271]. As previously mentioned, Aβ oligomers have been linked to neuronal loss and neuronal network disruption in AD [61, 62], therefore, the application of the all-optical assay combined with the iPSC technology in 2D and 3D cellular models would enable the study of the network disruption in AD and evaluate the improvement of the neural network connectivity with potential compounds. It could also potentially be used to screen compounds which would protect neural networks from being disrupted. These meaningful findings could help advancing AD research.

Overall, these experiments highlighted the sensitivity of the OptoCaMP all-optical assay and its potential application for *in vitro* studies aiming to evaluate the neuronal activity in conditions where the neuronal connectivity is enhanced or decreased. These encouraging results bring the promise of enabling the study of more complex pharmacological conditions and how diseased neural networks communicate and respond to potential therapeutic agent. For example, this system could be easily integrated with hardware platforms used for quantitative *in vitro* high-throughput screening and could potentially be adapted to multi-well plates. Under these conditions,

it would take ~10s to record from each field of view in triplicate, which would correspond to approximatively 30s/well implying 50 min for a 96 well-plate. This capability could be achieved using automated liquid handlers and other currently available automated platforms to investigate how diseased neural networks communicate and respond to potential therapeutic agent [255]. In addition, it is worth mentioning that the use of a smaller magnification high numerical aperture objective (e.g. 10X 0.5 NA), a larger field of view and thus a bigger neuronal network, could also be investigated and analysed. Moreover, even though the OptoCaMP allows simultaneous stimulation and calcium imaging with single-neuron resolution and readout, the microscope setup used in this study can be considered as a limiting factor as it does not enable the excitation of CheRiff with a micrometre-precise blue illumination pattern. To achieve precise stimulation of single-neuron expressing OptoCaMP *in vitro*, the optical system could be adapted with the addition of more precise optical devices, such as a Digital Micromirror Device [272]. As future possibilities, this system could be extended *in vivo* with the use of single-cell two-photon optogenetic photostimulation [273]. In this context, ratio-metric calcium imaging would potentially provide a more accurate quantification than a single-wavelength indicator [274]. However, to achieve this goal, the development a Genetically Encoded Ratiometric Calcium Indicator version of jRCaMP1b based on the same approach as the GCaMP-R family would be necessary [275]. Though notably, previous studies have reported aberrant neuronal activity in GCaMP6-expressing transgenic mouse lines [276] indicating that potential OptoCaMP-expressing transgenic mouse lines would require further investigation to evaluate any aberrant activity.

References

References

1. Muratore, C.R., et al., *The familial Alzheimer's disease APPV717I mutation alters APP processing and Tau expression in iPSC-derived neurons.* Human Molecular Genetics, 2014. **23**(13): p. 3523-3536.
2. Liu, G.-H., Z. Ding, and J.C. Izpisua Belmonte, *iPSC technology to study human aging and aging-related disorders.* Current Opinion in Cell Biology, 2012. **24**(6): p. 765-774.
3. Afshar Saber, W., et al., *All-Optical Assay to Study Biological Neural Networks.* Frontiers in Neuroscience, 2018. **12**: p. 451.
4. Marchetto, M.C.N., B. Winner, and F.H. Gage, *Pluripotent stem cells in neurodegenerative and neurodevelopmental diseases.* Human Molecular Genetics, 2010. **19**(R1): p. R71-R76.
5. Bloom, F.E., *Chapter 1 - Fundamentals of Neuroscience*, in *Fundamental Neuroscience (Fourth Edition)*, L.R. Squire, et al., Editors. 2013, Academic Press: San Diego. p. 3-13.
6. Cajal, S.R., *Histology of the nervous system of man and vertebrates.* History of Neuroscience (Oxford Univ Press, New York), 1995(6).
7. Schwarz, T.L., *Chapter 7 - Release of Neurotransmitters*, in *Fundamental Neuroscience (Fourth Edition)*, L.R. Squire, et al., Editors. 2013, Academic Press: San Diego. p. 139-161.
8. McCormick, D.A., *Chapter 5 - Membrane Potential and Action Potential*, in *Fundamental Neuroscience (Fourth Edition)*, L.R. Squire, et al., Editors. 2013, Academic Press: San Diego. p. 93-116.
9. Bagur, R. and G. Hajnóczky, *Intracellular Ca²⁺ Sensing: Its Role in Calcium Homeostasis and Signaling.* Molecular Cell, 2017. **66**(6): p. 780-788.
10. Liang, H., et al., *Unified Mechanisms of Ca²⁺ Regulation across the Ca²⁺ Channel Family.* Neuron, 2003. **39**(6): p. 951-960.
11. Catterall, W.A., *Structure and Regulation of Voltage-Gated Ca2+ Channels.* Annual Review of Cell and Developmental Biology, 2000. **16**(1): p. 521-555.
12. Zhang, Y., et al., *Mutations in High-Voltage-Activated Calcium Channel Genes Stimulate Low-Voltage-Activated Currents in Mouse Thalamic Relay Neurons.* The Journal of Neuroscience, 2002. **22**(15): p. 6362.
13. Usowicz, M.M., et al., *P-type calcium channels in the somata and dendrites of adult cerebellar purkinje cells.* Neuron, 1992. **9**(6): p. 1185-1199.
14. Hoogland, T.M. and P. Saggau, *Facilitation of L-Type Ca²⁺ Channels in Dendritic Spines by Activation of β₂ Adrenergic Receptors.* The Journal of Neuroscience, 2004. **24**(39): p. 8416-8427.
15. Spruston, N., et al., *Activity-dependent action potential invasion and calcium influx into hippocampal CA1 dendrites.* Science, 1995. **268**(5208): p. 297-300.
16. Reid, C.A., R. Fabian-Fine, and A. Fine, *Postsynaptic Calcium Transients Evoked by Activation of Individual Hippocampal Mossy Fiber Synapses.* The Journal of Neuroscience, 2001. **21**(7): p. 2206-2214.

17. Nevian, T. and B. Sakmann, *Spine Ca²⁺ Signaling in Spike-Timing-Dependent Plasticity.* The Journal of Neuroscience, 2006. **26**(43): p. 11001-11013.
18. Burnashev, N., et al., *Fractional calcium currents through recombinant GluR channels of the NMDA, AMPA and kainate receptor subtypes.* The Journal of Physiology, 1995. **485**(2): p. 403-418.
19. Skeberdis, V.A., et al., *Protein kinase A regulates calcium permeability of NMDA receptors.* Nature Neuroscience, 2006. **9**: p. 501.
20. Mayer, M.L., G.L. Westbrook, and P.B. Guthrie, *Voltage-dependent block by Mg2+ of NMDA responses in spinal cord neurones.* Nature, 1984. **309**: p. 261.
21. Watson, J.F., H. Ho, and I.H. Greger, *Synaptic transmission and plasticity require AMPA receptor anchoring via its N-terminal domain.* eLife, 2017. **6**: p. e23024.
22. Berridge, M.J., M.D. Bootman, and H.L. Roderick, *Calcium signalling: dynamics, homeostasis and remodelling.* Nature Reviews Molecular Cell Biology, 2003. **4**: p. 517.
23. Ferreiro, E., C.R. Oliveira, and C. Pereira, *Involvement of endoplasmic reticulum Ca2+ release through ryanodine and inositol 1,4,5-triphosphate receptors in the neurotoxic effects induced by the amyloid-β peptide.* Journal of Neuroscience Research, 2004. **76**(6): p. 872-880.
24. Zhao, C., W. Deng, and F.H. Gage, *Mechanisms and Functional Implications of Adult Neurogenesis.* Cell. **132**(4): p. 645-660.
25. Bezprozvanny, I. and M.P. Mattson, *Neuronal Calcium Mishandling and the Pathogenesis of Alzheimer's Disease.* Trends in neurosciences, 2008. **31**(9): p. 454-463.
26. LaFerla, F.M., *Calcium dyshomeostasis and intracellular signalling in alzheimer's disease.* Nature Reviews Neuroscience, 2002. **3**: p. 862.
27. Karbasi, A., A.H. Salavati, and M. Vetterli, *Learning neural connectivity from firing activity: efficient algorithms with provable guarantees on topology.* Journal of Computational Neuroscience, 2018. **44**(2): p. 253-272.
28. Brown, E.N., R.E. Kass, and P.P. Mitra, *Multiple neural spike train data analysis: state-of-the-art and future challenges.* Nature Neuroscience, 2004. **7**: p. 456.
29. Kim, S., et al., *A Granger Causality Measure for Point Process Models of Ensemble Neural Spiking Activity.* PLOS Computational Biology, 2011. **7**(3): p. e1001110.
30. Gu, Z., W. Liu, and Z. Yan, *{beta}-Amyloid impairs AMPA receptor trafficking and function by reducing Ca2+/calmodulin-dependent protein kinase II synaptic distribution.* The Journal of biological chemistry, 2009. **284**(16): p. 10639-10649.
31. Parihar, M.S. and G.J. Brewer, *Amyloid-β as a modulator of synaptic plasticity.* Journal of Alzheimer's disease : JAD, 2010. **22**(3): p. 741-763.
32. Ray, M. and W. Zhang, *Analysis of Alzheimer's disease severity across brain regions by topological analysis of gene co-expression networks.* BMC Systems Biology, 2010. **4**(1).
33. Musiek, E.S. and D.M. Holtzman, *Origins of Alzheimer's Disease: Reconciling CSF biomarker and neuropathology data regarding the temporal sequence of Aβ and tau involvement.* Current opinion in neurology, 2012. **25**(6): p. 715-720.

34. Wray, S. and W. Noble, *Linking Amyloid and Tau Pathology in Alzheimer's Disease: The Role of Membrane Cholesterol in Aβ-Mediated Tau Toxicity.* The Journal of Neuroscience, 2009. **29**(31): p. 9665-9667.
35. Braak, H. and E. Braak, *Morphological criteria for the recognition of Alzheimer's disease and the distribution pattern of cortical changes related to this disorder.* Neurobiology of Aging, 1994. **15**(3): p. 355-356.
36. Masliah, E., *The Role of Synaptic Proteins in Alzheimer's Disease.* Annals of the New York Academy of Sciences, 2000. **924**(1): p. 68-75.
37. Jack, C.R., et al., *Introduction to Revised Criteria for the Diagnosis of Alzheimer's Disease: National Institute on Aging and the Alzheimer Association Workgroups.* Alzheimer's & dementia : the journal of the Alzheimer's Association, 2011. **7**(3): p. 257-262.
38. Brugnolo, A., et al., *The factorial structure of the mini mental state examination (MMSE) in Alzheimer's disease.* Archives of Gerontology and Geriatrics, 2009. **49**(1): p. 180-185.
39. Rowe, C.C., et al., *Imaging of amyloid β in Alzheimer's disease with ¹⁸F-BAY94-9172, a novel PET tracer: proof of mechanism.* The Lancet Neurology, 2008. **7**(2): p. 129-135.
40. Goedert, M. and M.G. Spillantini, *A Century of Alzheimer's Disease.* Science, 2006. **314**(5800): p. 777-781.
41. Tarawneh, R. and D.M. Holtzman, *The Clinical Problem of Symptomatic Alzheimer Disease and Mild Cognitive Impairment.* Cold Spring Harbor Perspectives in Medicine, 2012. **2**(5): p. a006148.
42. Van Cauwenberghe, C., C. Van Broeckhoven, and K. Sleegers, *The genetic landscape of Alzheimer disease: clinical implications and perspectives.* Genet Med, 2015.
43. Rao, A.T., A.J. Degnan, and L.M. Levy, *Genetics of Alzheimer Disease.* American Journal of Neuroradiology, 2014. **35**(3): p. 457-458.
44. Nicolas, G., et al., *Screening of dementia genes by whole-exome sequencing in early-onset Alzheimer disease: input and lessons.* Eur J Hum Genet, 2015.
45. Cruts, M., J. Theuns, and C. Van Broeckhoven, *Locus-Specific Mutation Databases for Neurodegenerative Brain Diseases.* Human Mutation, 2012. **33**(9): p. 1340-1344.
46. Goate, A., et al., *Segregation of a missense mutation in the amyloid precursor protein gene with familial Alzheimer's disease.* Nature, 1991. **349**: p. 704.
47. *Molecular classification of Alzheimer's disease.* The Lancet, 1991. **337**(8753): p. 1342-1343.
48. MacLeod, R., et al., *The role and therapeutic targeting of α-, β- and γ-secretase in Alzheimer's disease.* Future Science OA, 2015. **1**(3): p. FSO11.
49. Scheuner, D., et al., *Secreted amyloid β–protein similar to that in the senile plaques of Alzheimer's disease is increased in vivo by the presenilin 1 and 2 and APP mutations linked to familial Alzheimer's disease.* Nature Medicine, 1996. **2**: p. 864.

50. Eckman, C.B., et al., *A New Pathogenic Mutation in the APP Gene (I716V) Increases the Relative Proportion of Aβ42(43).* Human Molecular Genetics, 1997. **6**(12): p. 2087-2089.
51. De Jonghe, C., et al., *Pathogenic APP mutations near the γ-secretase cleavage site differentially affect Aβ secretion and APP C-terminal fragment stability.* Human Molecular Genetics, 2001. **10**(16): p. 1665-1671.
52. Pauwels, K., et al., *Structural Basis for Increased Toxicity of Pathological Aβ(42):Aβ(40) Ratios in Alzheimer Disease.* The Journal of Biological Chemistry, 2012. **287**(8): p. 5650-5660.
53. Dewachter, I., et al., *Modeling Alzheimer's disease in transgenic mice: effect of age and of Presenilin1 on amyloid biochemistry and pathology in APP/London mice.* Experimental Gerontology, 2000. **35**(6): p. 831-841.
54. Di Fede, G., et al., *A Recessive Mutation in the APP Gene with Dominant-Negative Effect on Amyloidogenesis.* Science, 2009. **323**(5920): p. 1473-1477.
55. Di Fede, G., et al., *Good gene, bad gene: New APP variant may be both.* Progress in Neurobiology, 2012. **99**(3): p. 281-292.
56. Avramopoulos, D., *Genetics of Alzheimer's disease: recent advances.* Genome Medicine, 2009. **1**(3): p. 34-34.
57. Gatz, M., et al., *ROle of genes and environments for explaining alzheimer disease.* Archives of General Psychiatry, 2006. **63**(2): p. 168-174.
58. O'Brien, R.J. and P.C. Wong, *Amyloid Precursor Protein Processing and Alzheimer's Disease.* Annual review of neuroscience, 2011. **34**: p. 185-204.
59. Tsai, M.S., et al., *Apolipoprotein E: risk factor for Alzheimer disease.* American Journal of Human Genetics, 1994. **54**(4): p. 643-649.
60. Tokuda, T., et al., *Lipidation of apolipoprotein E influences its isoform-specific interaction with Alzheimer's amyloid beta peptides.* Biochemical Journal, 2000. **348**(Pt 2): p. 359-365.
61. Shankar, G.M., et al., *Natural Oligomers of the Alzheimer Amyloid-β Protein Induce Reversible Synapse Loss by Modulating an NMDA-Type Glutamate Receptor-Dependent Signaling Pathway.* The Journal of Neuroscience, 2007. **27**(11): p. 2866-2875.
62. Shankar, G.M., et al., *Amyloid β-Protein Dimers Isolated Directly from Alzheimer Brains Impair Synaptic Plasticity and Memory.* Nature medicine, 2008. **14**(8): p. 837-842.
63. Giuffrida, M.L., et al., *β-Amyloid Monomers Are Neuroprotective.* The Journal of Neuroscience, 2009. **29**(34): p. 10582-10587.
64. Serrano-Pozo, A., et al., *Neuropathological Alterations in Alzheimer Disease.* Cold Spring Harbor Perspectives in Medicine:, 2011. **1**(1): p. a006189.
65. Sokolow, S., et al., *Isolation of synaptic terminals from Alzheimer's disease cortex.* Cytometry, 2012. **81**(3): p. 248-254.
66. Masliah, E., et al., *Altered expression of synaptic proteins occurs early during progression of Alzheimer's disease.* Neurology, 2001. **56**(1): p. 127-129.
67. Mucke, L., et al., *High-Level Neuronal Expression of Aβ_{1–42} in Wild-Type Human Amyloid Protein Precursor Transgenic Mice: Synaptotoxicity without Plaque Formation.* The Journal of Neuroscience, 2000. **20**(11): p. 4050-4058.

68. Pham, E., et al., *Progressive accumulation of amyloid-β oligomers in Alzheimer's disease and APP transgenic mice is accompanied by selective alterations in synaptic scaffold proteins.* The FEBS journal, 2010. **277**(14): p. 3051-3067.
69. Moreno, H., et al., *Synaptic transmission block by presynaptic injection of oligomeric amyloid beta.* Proceedings of the National Academy of Sciences, 2009. **106**(14): p. 5901.
70. Cummings, J.L., T. Morstorf, and K. Zhong, *Alzheimer's disease drug-development pipeline: few candidates, frequent failures.* Alzheimer's Research & Therapy, 2014. **6**(4): p. 37-37.
71. van der Worp, H.B., et al., *Can Animal Models of Disease Reliably Inform Human Studies?* PLoS Medicine, 2010. **7**(3): p. e1000245.
72. Gomez-Nicola, D. and D. Boche, *Post-mortem analysis of neuroinflammatory changes in human Alzheimer's disease.* Alzheimer's Research & Therapy, 2015. **7**(1): p. 42.
73. Robinton, D.A. and G.Q. Daley, *The promise of induced pluripotent stem cells in research and therapy.* Nature, 2012. **481**(7381): p. 295-305.
74. Takahashi, K. and S. Yamanaka, *Induction of Pluripotent Stem Cells from Mouse Embryonic and Adult Fibroblast Cultures by Defined Factors.* Cell, 2006. **126**(4): p. 663-676.
75. Yamanaka, S., *Induced Pluripotent Stem Cells: Past, Present, and Future.* Cell Stem Cell, 2012. **10**(6): p. 678-684.
76. Takahashi, K., et al., *Induction of Pluripotent Stem Cells from Adult Human Fibroblasts by Defined Factors.* Cell, 2007. **131**(5): p. 861-872.
77. Yu, J., et al., *Induced Pluripotent Stem Cell Lines Derived from Human Somatic Cells.* Science, 2007. **318**(5858): p. 1917-1920.
78. Park, I.-H., et al., *Reprogramming of human somatic cells to pluripotency with defined factors.* Nature, 2008. **451**(7175): p. 141-146.
79. Park, I.-H., et al., *Disease-Specific Induced Pluripotent Stem Cells.* Cell, 2008. **134**(5): p. 877-886.
80. Onder, T.T. and G.Q. Daley, *New lessons learned from disease modeling with induced pluripotent stem cells.* Current Opinion in Genetics & Development, 2012. **22**(5): p. 500-508.
81. Mohamet, L., N.J. Miazga, and C.M. Ward, *Familial Alzheimer's disease modelling using induced pluripotent stem cell technology.* World J Stem Cells, 2014. **6**(2): p. 239-47.
82. Dimos, J.T., et al., *Induced Pluripotent Stem Cells Generated from Patients with ALS Can Be Differentiated into Motor Neurons.* Science, 2008. **321**(5893): p. 1218-1221.
83. Woodard, Chris M., et al., *iPSC-Derived Dopamine Neurons Reveal Differences between Monozygotic Twins Discordant for Parkinson's Disease.* Cell Reports, 2014. **9**(4): p. 1173-1182.
84. Devine, M.J., et al., *Parkinson's disease induced pluripotent stem cells with triplication of the α-synuclein locus.* Nat Commun, 2011. **2**: p. 440.
85. Israel, M.A., et al., *Probing sporadic and familial Alzheimer's disease using induced pluripotent stem cells.* Nature, 2012. **482**(7384): p. 216-220.

86. Boulting, G.L., et al., *A functionally characterized test set of human induced pluripotent stem cells.* Nat Biotech, 2011. **29**(3): p. 279-286.
87. Koch, P., et al., *Presenilin-1 L166P Mutant Human Pluripotent Stem Cell–Derived Neurons Exhibit Partial Loss of γ-Secretase Activity in Endogenous Amyloid-β Generation.* The American Journal of Pathology, 2012. **180**(6): p. 2404-2416.
88. Kondo, T., et al., *Modeling Alzheimer's Disease with iPSCs Reveals Stress Phenotypes Associated with Intracellular Aβ and Differential Drug Responsiveness.* Cell Stem Cell, 2013. **12**(4): p. 487-496.
89. Yagi, T., et al., *Modeling familial Alzheimer's disease with induced pluripotent stem cells.* Human Molecular Genetics, 2011. **20**(23): p. 4530-4539.
90. Glomset, J.A., *Role of Docosahexaenoic Acid in Neuronal Plasma Membranes.* Science's STKE, 2006. **2006**(321): p. pe6.
91. Choi, S.H., et al., *A three-dimensional human neural cell culture model of Alzheimer/'s disease.* Nature, 2014. **515**(7526): p. 274-278.
92. Park, J., et al., *A 3D human triculture system modeling neurodegeneration and neuroinflammation in Alzheimer's disease.* Nature Neuroscience, 2018. **21**(7): p. 941-951.
93. Johnson, I.P., *Age-related neurodegenerative disease research needs ageing models.* Frontiers in Aging Neuroscience, 2015. **7**.
94. Sánchez-Danés, A., et al., *Disease-specific phenotypes in dopamine neurons from human iPS-based models of genetic and sporadic Parkinson's disease.* EMBO Molecular Medicine, 2012. **4**(5): p. 380-395.
95. Miller, J.D., et al., *Human iPSC-based Modeling of Late-Onset Disease via Progerin-induced Aging.* Cell stem cell, 2013. **13**(6): p. 691-705.
96. Finkel, T. and N.J. Holbrook, *Oxidants, oxidative stress and the biology of ageing.* Nature, 2000. **408**(6809): p. 239-247.
97. Shi, Y., et al., *Human cerebral cortex development from pluripotent stem cells to functional excitatory synapses.* Nat Neurosci, 2012. **15**(3): p. 477-486.
98. Hodgkin, A.L., A.F. Huxley, and B. Katz, *Measurement of current-voltage relations in the membrane of the giant axon of Loligo.* The Journal of Physiology, 1952. **116**(4): p. 424-448.
99. McCormick, D.A., et al., *Comparative electrophysiology of pyramidal and sparsely spiny stellate neurons of the neocortex.* Journal of Neurophysiology, 1985. **54**(4): p. 782-806.
100. Kornreich, B.G., *The patch clamp technique: Principles and technical considerations.* Journal of Veterinary Cardiology, 2007. **9**(1): p. 25-37.
101. Scanziani, M. and M. Hausser, *Electrophysiology in the age of light.* Nature, 2009. **461**(7266): p. 930-939.
102. Neher, E. and B. Sakmann, *Single-channel currents recorded from membrane of denervated frog muscle fibres.* Nature, 1976. **260**: p. 799-802.
103. Perkins, K.L., *Cell-attached voltage-clamp and current-clamp recording and stimulation techniques in brain slices.* Journal of Neuroscience Methods, 2006. **154**(1-2): p. 1-18.
104. The Allen Institute for Brain Science. *TECHNICAL WHITE PAPER: ELECTROPHYSIOLOGY*. Cell Types Database 2015.

105. Dunlop, J., et al., *High-throughput electrophysiology: an emerging paradigm for ion-channel screening and physiology.* Nat Rev Drug Discov, 2008. **7**(4): p. 358-368.
106. The Petilla Interneuron Nomenclature, G., *Petilla terminology: nomenclature of features of GABAergic interneurons of the cerebral cortex.* Nature reviews. Neuroscience, 2008. **9**(7): p. 557-568.
107. Hochbaum, D.R., et al., *All-optical electrophysiology in mammalian neurons using engineered microbial rhodopsins.* Nature methods, 2014. **11**(8): p. 825-833.
108. Buzsaki, G., *Large-scale recording of neuronal ensembles.* Nat Neurosci, 2004. **7**(5): p. 446-451.
109. Massobrio, P., et al., *In Vitro Studies of Neuronal Networks and Synaptic Plasticity in Invertebrates and in Mammals Using Multielectrode Arrays.* Neural Plasticity, 2015. **2015**: p. 196195.
110. Obien, M.E.J., et al., *Revealing neuronal function through microelectrode array recordings.* Frontiers in Neuroscience, 2014. **8**: p. 423.
111. Wagenaar, D.A., J. Pine, and S.M. Potter, *Effective parameters for stimulation of dissociated cultures using multi-electrode arrays.* Journal of Neuroscience Methods, 2004. **138**(1–2): p. 27-37.
112. Einevoll, G.T., et al., *Towards reliable spike-train recordings from thousands of neurons with multielectrodes.* Current Opinion in Neurobiology, 2012. **22**(1): p. 11-17.
113. Boyden, E.S., et al., *Millisecond-timescale, genetically targeted optical control of neural activity.* Nature Neuroscience, 2005. **8**(9): p. 1263-1268.
114. Deisseroth, K., et al., *Next-Generation Optical Technologies for Illuminating Genetically Targeted Brain Circuits.* The Journal of neuroscience : the official journal of the Society for Neuroscience, 2006. **26**(41): p. 10380.
115. Deisseroth, K., *Optogenetics.* Nat Meth, 2011. **8**(1): p. 26-29.
116. Nagel, G., et al., *Light Activation of Channelrhodopsin-2 in Excitable Cells of Caenorhabditis elegans Triggers Rapid Behavioral Responses.* Current Biology, 2005. **15**(24): p. 2279-2284.
117. Li, X., et al., *Fast noninvasive activation and inhibition of neural and network activity by vertebrate rhodopsin and green algae channelrhodopsin.* Proceedings of the National Academy of Sciences of the United States of America, 2005. **102**(49): p. 17816-17821.
118. Lanyi, J.K. and H. Luecke, *Bacteriorhodopsin.* Current Opinion in Structural Biology, 2001. **11**(4): p. 415-419.
119. Gradinaru, V., K.R. Thompson, and K. Deisseroth, *eNpHR: a Natronomonas halorhodopsin enhanced for optogenetic applications.* Brain cell biology, 2008. **36**(1-4): p. 129-139.
120. Nagel, G., et al., *Channelrhodopsin-2, a directly light-gated cation-selective membrane channel.* Proceedings of the National Academy of Sciences of the United States of America, 2003. **100**(24): p. 13940-13945.
121. Guru, A., et al., *Making Sense of Optogenetics.* Int J Neuropsychopharmacol, 2015. **18**(11).

122. Gorostiza, P. and E.Y. Isacoff, *Optical Switches for Remote and Noninvasive Control of Cell Signaling.* Science, 2008. **322**(5900): p. 395-399.
123. Bernstein, J.G. and E.S. Boyden, *Optogenetic tools for analyzing the neural circuits of behavior.* Trends in cognitive sciences, 2011. **15**(12): p. 592-600.
124. Fenno, L., O. Yizhar, and K. Deisseroth, *The Development and Application of Optogenetics.* Annual Review of Neuroscience, 2011. **34**(1): p. 389-412.
125. McIsaac, R.S., C.N. Bedbrook, and F.H. Arnold, *Recent advances in engineering microbial rhodopsins for optogenetics.* Current Opinion in Structural Biology, 2015. **33**: p. 8-15.
126. Bamann, C., et al., *Spectral Characteristics of the Photocycle of Channelrhodopsin-2 and Its Implication for Channel Function.* Journal of Molecular Biology, 2008. **375**(3): p. 686-694.
127. Nagel, G., et al., *Channelrhodopsins: directly light-gated cation channels.* Biochemical Society Transactions, 2005. **33**(4): p. 863-866.
128. Nagel, G., et al., *Channelrhodopsin-1: A Light-Gated Proton Channel in Green Algae.* Science, 2002. **296**(5577): p. 2395-2398.
129. Zhang, F., et al., *The Microbial Opsin Family of Optogenetic Tools.* Cell, 2011. **147**(7): p. 1446-1457.
130. Zhang, F., et al., *Multimodal fast optical interrogation of neural circuitry.* Nature, 2007. **446**(7136): p. 633-639.
131. Lin, J.Y., *A User's Guide to Channelrhodopsin Variants: Features, Limitations and Future Developments.* Experimental physiology, 2011. **96**(1): p. 19-25.
132. Yizhar, O., et al., *Optogenetics in neural systems.* Neuron, 2011. **71**(1): p. 9-34.
133. Gunaydin, L.A., et al., *Ultrafast optogenetic control.* Nat Neurosci, 2010. **13**(3): p. 387-392.
134. Mattis, J., et al., *Principles for applying optogenetic tools derived from direct comparative analysis of microbial opsins.* Nature methods, 2012. **9**(2): p. 159-172.
135. Hight, A.E., et al., *Temporal Resolution of ChR2 and Chronos in an Optogenetic-based Auditory Brainstem Implant Model: Implications for the Development and Application of Auditory Opsins.* Hearing research, 2015. **322**: p. 235-241.
136. Yizhar, O., et al., *Neocortical excitation/inhibition balance in information processing and social dysfunction.* Nature, 2011. **477**(7363): p. 171-178.
137. Lin, J.Y., et al., *Characterization of Engineered Channelrhodopsin Variants with Improved Properties and Kinetics.* Biophysical Journal, 2009. **96**(5): p. 1803-1814.
138. Schoenenberger, P., Y.-P.Z. Schärer, and T.G. Oertner, *Channelrhodopsin as a tool to investigate synaptic transmission and plasticity.* Experimental Physiology, 2011. **96**(1): p. 34-39.
139. Berndt, A., et al., *Bi-stable neural state switches.* Nat Neurosci, 2009. **12**(2): p. 229-234.
140. Berndt, A., et al., *High-efficiency channelrhodopsins for fast neuronal stimulation at low light levels.* Proceedings of the National Academy of Sciences of the United States of America, 2011. **108**(18): p. 7595-7600.
141. Klapoetke, N.C., et al., *Independent optical excitation of distinct neural populations.* Nature Methods, 2014. **11**(3): p. 338-46.

142. Hochbaum, D.R., et al., *All-optical electrophysiology in mammalian neurons using engineered microbial rhodopsins.* Nature Methods, 2014. **11**(8): p. 825-33.
143. Lin, J.Y., et al., *ReaChR: a red-shifted variant of channelrhodopsin enables deep transcranial optogenetic excitation.* Nature Neuroscience, 2013. **16**: p. 1499.
144. Häusser, M., *Optogenetics: the age of light.* Nature Methods, 2014. **11**: p. 1012.
145. Kleinlogel, S., et al., *Ultra light-sensitive and fast neuronal activation with the Ca2+-permeable channelrhodopsin CatCh.* Nat Neurosci, 2011. **14**(4): p. 513-518.
146. Klapoetke, N.C., et al., *Independent Optical Excitation of Distinct Neural Populations.* Nature methods, 2014. **11**(3): p. 338-346.
147. Ainsworth, M., et al., *Rates and Rhythms: A Synergistic View of Frequency and Temporal Coding in Neuronal Networks.* Neuron, 2012. **75**(4): p. 572-583.
148. Guerrero, G. and E.Y. Isacoff, *Genetically encoded optical sensors of neuronal activity and cellular function.* Current Opinion in Neurobiology, 2001. **11**(5): p. 601-607.
149. Chemla, S. and F. Chavane, *Voltage-sensitive dye imaging: Technique review and models.* Journal of Physiology-Paris, 2010. **104**(1): p. 40-50.
150. Lin, M.Z. and M.J. Schnitzer, *Genetically encoded indicators of neuronal activity.* Nature Neuroscience, 2016. **19**: p. 1142.
151. Cohen, L.B., et al., *Changes in axon fluorescence during activity: Molecular probes of membrane potential.* The Journal of Membrane Biology, 1974. **19**(1): p. 1-36.
152. Grinvald, A., et al., *Fluorescence monitoring of electrical responses from small neurons and their processes.* Biophysical Journal, 1983. **42**(2): p. 195-198.
153. Carter, M. and J. Shieh, *Chapter 7 - Visualizing Neural Function*, in *Guide to Research Techniques in Neuroscience (Second Edition)*, M. Carter and J. Shieh, Editors. 2015, Academic Press: San Diego. p. 167-183.
154. Broussard, G.J., R. Liang, and L. Tian, *Monitoring activity in neural circuits with genetically encoded indicators.* Frontiers in Molecular Neuroscience, 2014. **7**: p. 97.
155. Yan, P., et al., *Palette of fluorinated voltage-sensitive hemicyanine dyes.* Proceedings of the National Academy of Sciences of the United States of America, 2012. **109**(50): p. 20443-20448.
156. Douglass, A.D., *The Voltage Imaging Frontier*, in *New Techniques in Systems Neuroscience*, A.D. Douglass, Editor. 2015, Springer International Publishing: Switzerland. p. 97-127.
157. Peron, S., T.-W. Chen, and K. Svoboda, *Comprehensive imaging of cortical networks.* Current Opinion in Neurobiology, 2015. **32**: p. 115-123.
158. Akemann, W., et al., *Route to genetically targeted optical electrophysiology: development and applications of voltage-sensitive fluorescent proteins.* Neurophotonics, 2015. **2**(2).
159. Gong, Y., et al., *High-speed recording of neural spikes in awake mice and flies with a fluorescent voltage sensor.* Science (New York, N.Y.), 2015. **350**(6266): p. 1361-1366.
160. Osakada, F., et al., *New rabies virus variants for monitoring and manipulating activity and gene expression in defined neural circuits.* Neuron, 2011. **71**(4): p. 617-631.

161. Yang, H.H. and F. St-Pierre, *Genetically Encoded Voltage Indicators: Opportunities and Challenges.* The Journal of Neuroscience, 2016. **36**(39): p. 9977-9989.
162. Siegel, M.S. and E.Y. Isacoff, *A Genetically Encoded Optical Probe of Membrane Voltage.* Neuron, 1997. **19**(4): p. 735-741.
163. Guerrero, G., et al., *Tuning FlaSh: Redesign of the Dynamics, Voltage Range, and Color of the Genetically Encoded Optical Sensor of Membrane Potential.* Biophysical Journal, 2002. **83**(6): p. 3607-3618.
164. Peterka, D.S., H. Takahashi, and R. Yuste, *Imaging Voltage in Neurons.* Neuron, 2011. **69**(1): p. 9-21.
165. Dimitrov, D., et al., *Engineering and Characterization of an Enhanced Fluorescent Protein Voltage Sensor.* PLOS ONE, 2007. **2**(5): p. e440.
166. Mishina, Y., et al., *Exploration of genetically encoded voltage indicators based on a chimeric voltage sensing domain.* Frontiers in Molecular Neuroscience, 2014. **7**.
167. St-Pierre, F., et al., *High-fidelity optical reporting of neuronal electrical activity with an ultrafast fluorescent voltage sensor.* Nat Neurosci, 2014.
168. Kralj, J.M., et al., *Optical recording of action potentials in mammalian neurons using a microbial rhodopsin.* Nature Methods, 2011. **9**(1): p. 90-95.
169. Gong, Y., J.Z. Li, and M.J. Schnitzer, *Enhanced Archaerhodopsin Fluorescent Protein Voltage Indicators.* PLoS One, 2013. **8**(6): p. e66959.
170. St-Pierre, F., M. Chavarha, and M.Z. Lin, *Designs and sensing mechanisms of genetically encoded fluorescent voltage indicators.* Current Opinion in Chemical Biology, 2015. **27**(0): p. 31-38.
171. Gong, Y., et al., *Imaging neural spiking in brain tissue using FRET-opsin protein voltage sensors.* Nature communications, 2014. **5**: p. 3674-3674.
172. Zou, P., et al., *Bright and fast multi-colored voltage reporters via electrochromic FRET.* Nature communications, 2014. **5**: p. 4625-4625.
173. St-Pierre, F., M. Chavarha, and M.Z. Lin, *Designs and sensing mechanisms of genetically encoded fluorescent voltage indicators.* Current Opinion in Chemical Biology, 2015. **27**: p. 31-38.
174. Storace, D., et al., *Genetically Encoded Protein Sensors of Membrane Potential*, in *Membrane Potential Imaging in the Nervous System and Heart*, M. Canepari, D. Zecevic, and O. Bernus, Editors. 2015, Springer International Publishing. p. 493-509.
175. Kralj, J.M., et al., *Optical recording of action potentials in mammalian neurons using a microbial rhodopsin.* Nature methods, 2012. **9**(1): p. 90-95.
176. Dombeck, D.A., et al., *Functional imaging of hippocampal place cells at cellular resolution during virtual navigation.* Nature Neuroscience, 2010. **13**: p. 1433.
177. McCombs, J.E. and A.E. Palmer, *Measuring calcium dynamics in living cells with Genetically Encodable Calcium Indicators.* Methods (San Diego, Calif.), 2008. **46**(3): p. 152-159.
178. Hille, B., *Pumping Ions.* Science, 1992. **255**(5045): p. 742.

179. Helmchen, F., J.G. Borst, and B. Sakmann, *Calcium dynamics associated with a single action potential in a CNS presynaptic terminal.* Biophysical Journal, 1997. **72**(3): p. 1458-1471.
180. Akerboom, J., et al., *Optimization of a GCaMP calcium indicator for neural activity imaging.* The Journal of neuroscience : the official journal of the Society for Neuroscience, 2012. **32**(40): p. 13819-13840.
181. Shimomura, O., F.H. Johnson, and Y. Saiga, *Extraction, Purification and Properties of Aequorin, a Bioluminescent Protein from the Luminous Hydromedusan, Aequorea.* Journal of Cellular and Comparative Physiology, 1962. **59**(3): p. 223-239.
182. Head, J.F., et al., *The crystal structure of the photoprotein aequorin at 2.3 Å resolution.* Nature, 2000. **405**: p. 372.
183. Xu, X., et al., *Imaging protein interactions with bioluminescence resonance energy transfer (BRET) in plant and mammalian cells and tissues.* Proceedings of the National Academy of Sciences, 2007. **104**(24): p. 10264.
184. Chiesa, A., et al., *Recombinant aequorin and green fluorescent protein as valuable tools in the study of cell signalling.* Biochemical Journal, 2001. **355**(1): p. 1.
185. Ottolini, D., T. Calì, and M. Brini, *Chapter Two - Methods to Measure Intracellular Ca2+ Fluxes with Organelle-Targeted Aequorin-Based Probes*, in *Methods in Enzymology*, L. Galluzzi and G. Kroemer, Editors. 2014, Academic Press. p. 21-45.
186. Baubet, V., et al., *Chimeric green fluorescent protein-aequorin as bioluminescent Ca²⁺ reporters at the single-cell level.* Proceedings of the National Academy of Sciences, 2000. **97**(13): p. 7260.
187. Iwano, S., et al., *Single-cell bioluminescence imaging of deep tissue in freely moving animals.* Science, 2018. **359**(6378): p. 935.
188. Grynkiewicz, G., M. Poenie, and R.Y. Tsien, *A new generation of Ca2+ indicators with greatly improved fluorescence properties.* Journal of Biological Chemistry, 1985. **260**(6): p. 3440-3450.
189. Tsien, R.Y., *Fluorescent Probes of Cell Signaling.* Annual Review of Neuroscience, 1989. **12**(1): p. 227-253.
190. Tsien, R.Y., T.J. Rink, and M. Poenie, *Measurement of cytosolic free Ca2+ in individual small cells using fluorescence microscopy with dual excitation wavelengths.* Cell Calcium, 1985. **6**(1): p. 145-157.
191. Garaschuk, O., et al., *Large-scale oscillatory calcium waves in the immature cortex.* Nature Neuroscience, 2000. **3**: p. 452.
192. Garaschuk, O., E. Hanse, and A. Konnerth, *Developmental profile and synaptic origin of early network oscillations in the CA1 region of rat neonatal hippocampus.* The Journal of Physiology, 1998. **507**(Pt 1): p. 219-236.
193. Bonifazi, P., et al., *GABAergic Hub Neurons Orchestrate Synchrony in Developing Hippocampal Networks.* Science, 2009. **326**(5958): p. 1419.
194. Trevelyan, A.J., et al., *Modular Propagation of Epileptiform Activity: Evidence for an Inhibitory Veto in Neocortex.* The Journal of Neuroscience, 2006. **26**(48): p. 12447.

195. Stosiek, C., et al., *In vivo two-photon calcium imaging of neuronal networks.* Proceedings of the National Academy of Sciences, 2003. **100**(12): p. 7319-7324.
196. Helmchen, F. and W. Denk, *Deep tissue two-photon microscopy.* Nature Methods, 2005. **2**: p. 932.
197. Aramuni, G. and O. Griesbeck, *Chronic calcium imaging in neuronal development and disease.* Experimental Neurology, 2013. **242**: p. 50-56.
198. Miyawaki, A., et al., *Fluorescent indicators for Ca2+based on green fluorescent proteins and calmodulin.* Nature, 1997. **388**: p. 882.
199. Miyawaki, A., et al., *Dynamic and quantitative Ca(2+) measurements using improved cameleons.* Proceedings of the National Academy of Sciences of the United States of America, 1999. **96**(5): p. 2135-2140.
200. Tian, L., et al., *Imaging neural activity in worms, flies and mice with improved GCaMP calcium indicators.* Nature Methods, 2009. **6**: p. 875.
201. Chen, T.-W., et al., *Ultra-sensitive fluorescent proteins for imaging neuronal activity.* Nature, 2013. **499**(7458): p. 295-300.
202. Tian, L., S.A. Hires, and L.L. Looger, *Imaging Neuronal Activity with Genetically Encoded Calcium Indicators.* Cold Spring Harbor Protocols, 2012. **2012**(6): p. pdb.top069609.
203. Sun, X.R., et al., *Fast GCaMPs for improved tracking of neuronal activity.* Nature Communications, 2013. **4**: p. 2170.
204. Baird, G.S., D.A. Zacharias, and R.Y. Tsien, *Circular permutation and receptor insertion within green fluorescent proteins.* Proceedings of the National Academy of Sciences, 1999. **96**(20): p. 11241.
205. Nagai, T., et al., *Circularly permuted green fluorescent proteins engineered to sense Ca<sup>2+</sup&gt.* Proceedings of the National Academy of Sciences, 2001. **98**(6): p. 3197.
206. Nakai, J., M. Ohkura, and K. Imoto, *A high signal-to-noise Ca2+ probe composed of a single green fluorescent protein.* Nature Biotechnology, 2001. **19**: p. 137.
207. Tallini, Y.N., et al., *Imaging cellular signals in the heart in vivo: Cardiac expression of the high-signal Ca(2+) indicator GCaMP2.* Proceedings of the National Academy of Sciences of the United States of America, 2006. **103**(12): p. 4753-4758.
208. Tian, L., et al., *Imaging neural activity in worms, flies and mice with improved GCaMP calcium indicators.* Nature methods, 2009. **6**(12): p. 875-881.
209. Muto, A., et al., *Genetic visualization with an improved GCaMP calcium indicator reveals spatiotemporal activation of the spinal motor neurons in zebrafish.* Proceedings of the National Academy of Sciences of the United States of America, 2011. **108**(13): p. 5425-5430.
210. Dana, H., et al., *High-performance GFP-based calcium indicators for imaging activity in neuronal populations and microcompartments.* bioRxiv, 2018: p. 434589.
211. Resendez, S.L., et al., *Visualization of cortical, subcortical and deep brain neural circuit dynamics during naturalistic mammalian behavior with head-mounted microscopes and chronically implanted lenses.* Nature Protocols, 2016. **11**: p. 566.

212. Yang, Y., et al., *Improved calcium sensor GCaMP-X overcomes the calcium channel perturbations induced by the calmodulin in GCaMP.* Nature Communications, 2018. **9**(1): p. 1504.
213. Akerboom, J., et al., *Genetically encoded calcium indicators for multi-color neural activity imaging and combination with optogenetics.* Frontiers in Molecular Neuroscience, 2013. **6**: p. 2.
214. Zhao, Y., et al., *An Expanded Palette of Genetically Encoded Ca(2+) Indicators.* Science (New York, N.Y.), 2011. **333**(6051): p. 1888-1891.
215. Broussard, G.J., R. Liang, and L. Tian, *Monitoring activity in neural circuits with genetically encoded indicators.* Frontiers in Molecular Neuroscience, 2014. **7**.
216. Adam, Y., et al., *All-optical electrophysiology reveals brain-state dependent changes in hippocampal subthreshold dynamics and excitability.* bioRxiv, 2018.
217. Dana, H., et al., *Sensitive red protein calcium indicators for imaging neural activity.* eLife, 2016. **5**: p. e12727.
218. Chen, T.-W., et al., *Ultrasensitive fluorescent proteins for imaging neuronal activity.* Nature, 2013. **499**(7458): p. 295-300.
219. Inoue, M., et al., *Rational design of a high-affinity, fast, red calcium indicator R-CaMP2.* Nature Methods, 2014. **12**: p. 64.
220. Ben Jehuda, R., Y. Shemer, and O. Binah, *Genome Editing in Induced Pluripotent Stem Cells using CRISPR/Cas9.* Stem Cell Reviews and Reports, 2018. **14**(3): p. 323-336.
221. Jang, M.J. and Y. Nam, *NeuroCa: integrated framework for systematic analysis of spatiotemporal neuronal activity patterns from large-scale optical recording data.* Neurophotonics, 2015. **2**(3): p. 035003.
222. Patel, T.P., et al., *Automated quantification of neuronal networks and single-cell calcium dynamics using calcium imaging.* Journal of Neuroscience Methods, 2015. **243**: p. 26-38.
223. Alivisatos, A.P., et al., *The Brain Activity Map Project and the Challenge of Functional Connectomics.* Neuron, 2012. **74**(6): p. 970-974.
224. Kim, J.H., et al., *High Cleavage Efficiency of a 2A Peptide Derived from Porcine Teschovirus-1 in Human Cell Lines, Zebrafish and Mice.* PLOS ONE, 2011. **6**(4): p. e18556.
225. Yaguchi, M., et al., *Characterization of the Properties of Seven Promoters in the Motor Cortex of Rats and Monkeys After Lentiviral Vector-Mediated Gene Transfer.* Human Gene Therapy Methods, 2013. **24**(6): p. 333-344.
226. Morikawa, S., et al., *Activation of perineuronal net-expressing excitatory neurons during associative memory encoding and retrieval.* Scientific Reports, 2017. **7**: p. 46024.
227. Jiang, M. and G. Chen, *High Ca2+-phosphate transfection efficiency in low-density neuronal cultures.* Nat Protoc, 2006. **1**(2): p. 695-700.
228. Chernousova, S. and M. Epple, *Live-cell imaging to compare the transfection and gene silencing efficiency of calcium phosphate nanoparticles and a liposomal transfection agent.* Gene Therapy, 2017. **24**: p. 282.

229. Dudek, H., A. Ghosh, and M.E. Greenberg, *Calcium Phosphate Transfection of DNA into Neurons in Primary Culture.* Current Protocols in Neuroscience, 1998. **3**(1): p. 3.11.1-3.11.6.
230. Goetze, B., et al., *Chemically controlled formation of a DNA/calcium phosphate coprecipitate: Application for transfection of mature hippocampal neurons.* Journal of Neurobiology, 2004. **60**(4): p. 517-525.
231. Elliott, C., et al., *National Instruments LabVIEW: A Programming Environment for Laboratory Automation and Measurement.* JALA: Journal of the Association for Laboratory Automation, 2007. **12**(1): p. 17-24.
232. Sakuma, T., Michael A. Barry, and Y. Ikeda, *Lentiviral vectors: basic to translational.* Biochemical Journal, 2012. **443**(3): p. 603.
233. Dittgen, T., et al., *Lentivirus-based genetic manipulations of cortical neurons and their optical and electrophysiological monitoring in vivo.* Proceedings of the National Academy of Sciences of the United States of America, 2004. **101**(52): p. 18206-18211.
234. Parr-Brownlie, L.C., et al., *Lentiviral vectors as tools to understand central nervous system biology in mammalian model organisms.* Frontiers in Molecular Neuroscience, 2015. **8**: p. 14.
235. Denning, W., et al., *Optimization of the transductional efficiency of lentiviral vectors: effect of sera and polycations.* Molecular biotechnology, 2013. **53**(3): p. 308-314.
236. Iwabuchi, S., et al., *Examination of Synaptic Vesicle Recycling Using FM Dyes During Evoked, Spontaneous, and Miniature Synaptic Activities.* Journal of Visualized Experiments : JoVE, 2014(85): p. 50557.
237. Aras, M.A., K.A. Hartnett, and E. Aizenman, *Assessment of Cell Viability in Primary Neuronal Cultures.* Current Protocols in Neuroscience, 2008. **44**(1): p. 7.18.1-7.18.15.
238. White, M.J., M.J. DiCaprio, and D.A. Greenberg, *Assessment of neuronal viability with Alamar blue in cortical and granule cell cultures.* Journal of Neuroscience Methods, 1996. **70**(2): p. 195-200.
239. Björk, S., et al., *Evaluation of Optogenetic Electrophysiology Tools in Human Stem Cell-Derived Cardiomyocytes.* Frontiers in Physiology, 2017. **8**: p. 884.
240. Rampersad, S.N., *Multiple Applications of Alamar Blue as an Indicator of Metabolic Function and Cellular Health in Cell Viability Bioassays.* Sensors (Basel, Switzerland), 2012. **12**(9): p. 12347-12360.
241. Vogt, N., *Sensing calcium in red.* Nature Methods, 2016. **13**: p. 468.
242. Makarov, V.A., F. Panetsos, and O.d. Feo, *A method for determining neural connectivity and inferring the underlying network dynamics using extracellular spike recordings.* Journal of Neuroscience Methods, 2005. **144**(2): p. 265-279.
243. Lin, Y.-C., et al., *Development of excitatory synapses in cultured neurons dissociated from the cortices of rat embryos and rat pups at birth.* Journal of Neuroscience Research, 2002. **67**(4): p. 484-493.
244. Mark, L.P., et al., *Pictorial Review of Glutamate Excitotoxicity: Fundamental Concepts for Neuroimaging.* American Journal of Neuroradiology, 2001. **22**(10): p. 1813-1824.

245. Manninen, T., et al., *Challenges in Reproducibility, Replicability, and Comparability of Computational Models and Tools for Neuronal and Glial Networks, Cells, and Subcellular Structures.* Frontiers in Neuroinformatics, 2018. **12**(20).
246. Junek, S., et al., *Activity Correlation Imaging: Visualizing Function and Structure of Neuronal Populations.* Biophysical Journal, 2009. **96**(9): p. 3801-3809.
247. Ito, S., et al., *Extending Transfer Entropy Improves Identification of Effective Connectivity in a Spiking Cortical Network Model.* PLOS ONE, 2011. **6**(11): p. e27431.
248. Orlandi, J.G., et al., *Transfer Entropy Reconstruction and Labeling of Neuronal Connections from Simulated Calcium Imaging.* PLOS ONE, 2014. **9**(6): p. e98842.
249. Seth, A.K., *A MATLAB toolbox for Granger causal connectivity analysis.* Journal of Neuroscience Methods, 2010. **186**(2): p. 262-273.
250. Bardy, C., et al., *Neuronal medium that supports basic synaptic functions and activity of human neurons in vitro.* Proceedings of the National Academy of Sciences, 2015. **112**(20): p. E2725-E2734.
251. van Aerde, K.I., G. Qi, and D. Feldmeyer, *Cell Type-Specific Effects of Adenosine on Cortical Neurons.* Cerebral Cortex (New York, NY), 2015. **25**(3): p. 772-787.
252. Yanovsky, Y., S. Velte, and U. Misgeld, *Ca2+ release-dependent hyperpolarizations modulate the firing pattern of juvenile GABA neurons in mouse substantia nigra pars reticulata in vitro.* The Journal of Physiology, 2006. **577**(3): p. 879-890.
253. Kerkhofs, A., et al., *Caffeine Controls Glutamatergic Synaptic Transmission and Pyramidal Neuron Excitability in Human Neocortex.* Frontiers in Pharmacology, 2018. **8**(899).
254. Hogins, J., et al., *Excitotoxicity triggered by Neurobasal culture medium.* PloS one, 2011. **6**(9): p. e25633-e25633.
255. Agus, V. and H. Janovjak, *Optogenetic methods in drug screening: technologies and applications.* Current Opinion in Biotechnology, 2017. **48**(Supplement C): p. 8-14.
256. Kiskinis, E., et al., *All-Optical Electrophysiology for High-Throughput Functional Characterization of a Human iPSC-Derived Motor Neuron Model of ALS.* Stem cell reports, 2018. **10**(6): p. 1991-2004.
257. Muratore, C.R., et al., *Cell-type Dependent Alzheimer's Disease Phenotypes: Probing the Biology of Selective Neuronal Vulnerability.* Stem cell reports, 2017. **9**(6): p. 1868-1884.
258. Zhang, Y., et al., *Rapid Single-Step Induction of Functional Neurons from Human Pluripotent Stem Cells.* Neuron, 2013. **78**(5): p. 785-798.
259. Wojcik, S.M., et al., *An essential role for vesicular glutamate transporter 1 (VGLUT1) in postnatal development and control of quantal size.* Proceedings of the National Academy of Sciences of the United States of America, 2004. **101**(18): p. 7158.
260. Maragakis, N.J., et al., *Glutamate transporter expression and function in human glial progenitors.* Glia, 2003. **45**(2): p. 133-143.

261. Ullian, E.M., et al., *Control of Synapse Number by Glia.* Science, 2001. **291**(5504): p. 657.
262. Tukker, A.M., et al., *Human iPSC-derived neuronal models for in vitro neurotoxicity assessment.* NeuroToxicology, 2018. **67**: p. 215-225.
263. Gossen, M., et al., *Transcriptional activation by tetracyclines in mammalian cells.* Science, 1995. **268**(5218): p. 1766.
264. Xu, Y., P. Zou, and A.E. Cohen, *Voltage imaging with genetically encoded indicators.* Current Opinion in Chemical Biology, 2017. **39**: p. 1-10.
265. Shew, W.L., T. Bellay, and D. Plenz, *Simultaneous multi-electrode array recording and two-photon calcium imaging of neural activity.* Journal of neuroscience methods, 2010. **192**(1): p. 75-82.
266. Sterneckert, J.L., P. Reinhardt, and H.R. Scholer, *Investigating human disease using stem cell models.* Nat Rev Genet, 2014. **15**(9): p. 625-639.
267. Wainger, B.J., et al., *Modeling pain in vitro using nociceptor neurons reprogrammed from fibroblasts.* Nat Neurosci, 2015. **18**(1): p. 17-24.
268. Keller, Philipp J. and Misha B. Ahrens, *Visualizing Whole-Brain Activity and Development at the Single-Cell Level Using Light-Sheet Microscopy.* Neuron, 2015. **85**(3): p. 462-483.
269. Bouchard, M.B., et al., *Swept confocally-aligned planar excitation (SCAPE) microscopy for high-speed volumetric imaging of behaving organisms.* Nat Photon, 2015. **9**(2): p. 113-119.
270. Pampaloni, F., E.G. Reynaud, and E.H.K. Stelzer, *The third dimension bridges the gap between cell culture and live tissue.* Nat Rev Mol Cell Biol, 2007. **8**(10): p. 839-845.
271. Wang, C., et al., *Scalable Production of iPSC-Derived Human Neurons to Identify Tau-Lowering Compounds by High-Content Screening.* Stem Cell Reports, 2017. **9**(4): p. 1221-1233.
272. Barral, J. and A.D. Reyes, *Optogenetic Stimulation and Recording of Primary Cultured Neurons with Spatiotemporal Control.* Bio-protocol, 2017. **7**(12): p. e2335.
273. Packer, A.M., et al., *Simultaneous all-optical manipulation and recording of neural circuit activity with cellular resolution in vivo.* Nature Methods, 2015. **12**(2): p. 140-146.
274. Thestrup, T., et al., *Optimized ratiometric calcium sensors for functional in vivo imaging of neurons and T lymphocytes.* Nature Methods, 2014. **11**(2): p. 175-82.
275. Cho, J.-H., et al., *The GCaMP-R Family of Genetically Encoded Ratiometric Calcium Indicators.* ACS Chemical Biology, 2017. **12**(4): p. 1066-1074.
276. Steinmetz, N.A., et al., *Aberrant Cortical Activity in Multiple GCaMP6-Expressing Transgenic Mouse Lines.* eNeuro, 2017. **4**(5): p. ENEURO.0207-17.2017.

Appendix A - Sequencing and Plasmids

OptoCaMP – BamHI-jRCaMP1b-AscI-P2A-CheRiffeGFP-EcoRI

GGATCCACCATGCTGCAGAACGAGCTTGCTCTTAAGTTGGCTGGACTTGATATTAACAAGACT
GGAGGAGGTTCTCATCATCATCATCATCATGGTATGGCTAGCATGACTGGTGGACAGCAAATG
GGTCGGGATCTGTACGACGATGACGATAAGGATCTCGCAACAATGGTCGACTCATCGCGACG
TAAGTGGAATAAGTGGGGTCACGCAGTCAGAGCTATAGGTCGGCTGAGCTCAGCGAACAACA
CCGAAATGATGTACCCAGCGGATGGTGGTCTGCGTGGTTACACTCACATGGCGCTGAAAGTT
GATGGCGGCGGTCACCTGTCCTGTTCTTTCGTGACCACCTACCGCTCCAAAAAGACTGTCGGC
AACATTAAGATGCCTGCCATTCATTACGTCAGCCACCGTCTGGAGCGCCTGGAGGAGAGCGAT
AACGAAATGTTTGTCGTACAGCGTGAACACGCAGTTGCCAAGTTTGTGGGCCTGGGTGGTGG
CGGCGGTACCGGAGGGAGCATGAACTCCCTGATCAAGGAGAACATGCGTATGAAAGTGGTTC
TGGAAGGCTCCGTAAACGGCCACCAGTTCAAATGCACTGGTGAAGGCGAAGGCAACCCGTAT
ATGGGCACCCAGACTATGCGTATCAAAGTGATCGAGGGTGGTCCGCTGCCGTTTGCGTTCGAC
ATCCTGGCGACGTCCTTTATGTATGGCTCCCGTACCTTCATCAAATATCCGAAAGGCATCCCGG
ATTTCTTTAAGCAGTCCTTCCCGGAAGGTTTTACCTGGGAACGTGTGACCCGTTACGAAGACG
GCGGCGTAATTACCGTTATGCAAGACACGTCTCTGGAGGATGGCTGCCTGGTGTATCACGTGC
AGGTTCGCGGTGTGAACTTCCCGAGCAATGGTGCTGTAATGCAAAAGAAAACCAAAGGTTGG
GAGCCTACGGACTCCCAACTGACTGAAGAGCAGATCGCAGAATTTAAAGAGGCTTTCTCCCTA
TTTGACAAGGACGGGGATGGGACAATAACAACCAAGGAGATGGGGACGGTGATGCGGTCTC
TGGGGCAGAACCCCACAGAAGCAGAGCTGCAGGACATGATCAATGAAGTAGATGCCGACGG
TGACGGCACAATCGACTTCCCTGAGTTCCTGATTATGATGGCAGGCAAAATGAAATACACAGA
CAGTGAAGAAGAAATTAGAGAAGCGTTCGGCGTGTTTGATAAGGATGGCAATGGCTACATCA
GTGCAGCAGAGCTTCGCCACGTGATGACAAACCTTGGAGAGAAGTTAACAGATGAAGAGGTT
GATGAAATGATCAGGGAAGCAGACAGCGATGGGGATGGTCAGGTAAACTACGAAGAGTTTG
TACAAATGATGACAGCGAAGAGGCGCGCCGGCTCCGGAGCCACGAACTTCTCTCTGTTAAAG
CAAGCAGGAGACGTGGAAGAAAACCCCGGTCCCGGCGGAGCTCCTGCTCCAGACGCTCACAG
CGCCCCACCTGGAAACGATTCTGCCGGAGGCAGTGAGTACCATGCCCCAGCTGGATATCAAGT
GAATCCACCCTACCACCCCGTGCATGGGTATGAGGAACAGTGCAGCTCCATCTACATCTACTAT
GGGGCCCTGTGGGAGCAGGAAACAGCTAGGGGCTTCCAGTGGTTTGCCGTGTTCCTGTCTGC
CCTGTTTCTGGCTTTCTACGGCTGGCACGCCTATAAGGCCAGCGTGGGATGGGAGGAAGTGT
ACGTGTGCTCCGTGGAGCTGATCAAAGTGATTCTGGAGATCTATTTCGAGTTCACCAGTCCTG
CTATGCTGTTCCTGTACGGAGGGAACATTACCCCATGGCTGAGATATGCCGAATGGCTGCTGA
CATGTCCCGTGATCCTGATTCATCTGTCTAACATCACCGGCCTGAGTGAGGCATACAATAAGC
GGACAATGGCTCTGCTGGTGTCCGACCTGGGAACTATTTGCATGGGAGTGACAGCCGCTCTG
GCCACTGGGTGGGTGAAGTGGCTGTTTTACTGTATCGGCCTGGTGTATGGAACCCAGACATTC
TACAACGCTGGAATCATCTACGTGGAGTCTTACTATATCATGCCTGCCGGCGGCTGTAAGAAA
CTGGTGCTGGCCATGACTGCCGTGTACTATTCTAGTTGGCTGATGTTTCCCGGCCTGTTCATCT
TTGGGCCTGAAGGCATGCACACCCTGAGCGTGGCTGGGTCCACTATTGGCCATACCATCGCCG
ACCTGCTGTCCAAGAATATTTGGGGACTGCTGGGGCACTTCCTGCGGATCAAAATTCACGAGC

ATATCATTATGTACGGCGATATCAGGAGACCAGTGAGCTCCCAGTTTCTGGGACGCAAGGTG
GACGTGCTGGCCTTCGTGACAGAGGAAGATAAAGTGGCGGCCGCCAAGAGCAGGATCACCA
GCGAGGGCGAGTACATCCCCCTGGACCAGATCGACATCAACGTGGTGAGCAAGGGCGAGGA
GCTGTTCACCGGGGTGGTGCCCATCCTGGTCGAGCTGGACGGCGACGTAAACGGCCACAAGT
TCAGCGTGTCCGGCGAGGGCGAGGGCGATGCCACCTACGGCAAGCTGACCCTGAAGTTCATT
TGCACCACCGGCAAGCTGCCCGTGCCCTGGCCCACCCTCGTGACCACCCTGACCTACGGCGTG
CAGTGCTTCAGCCGCTACCCCGACCACATGAAGCAGCACGACTTCTTCAAGTCCGCCATGCCC
GAAGGCTACGTCCAGGAGCGCACCATCTTCTTCAAGGACGACGGCAACTACAAGACCCGCGC
CGAGGTGAAGTTCGAGGGCGACACCCTGGTGAACCGCATCGAGCTGAAGGGCATCGACTTCA
AGGAGGACGGCAACATCCTGGGGCACAAGCTGGAGTACAACTACAACAGCCACAACGTCTAT
ATCATGGCCGACAAGCAGAAGAACGGCATCAAGGTGAACTTCAAGATCCGCCACAACATCGA
GGACGGCAGCGTGCAGCTCGCCGACCACTACCAGCAGAACACCCCCATCGGCGACGGCCCCG
TGCTGCTGCCCGACAACCACTACCTGAGCACCCAGTCCGCCCTGAGCAAAGACCCCAACGAGA
AGCGCGATCACATGGTCCTGCTGGAGTTCGTGACCGCCGCCGGGATCACTCTCGGCATGGAC
GAGCTGTACAAGTAAGAATTC

Primers used for the sequencing of FCK-OptoCaMP:

Primer 1	TCGTCAGTCAAGCCGGTTCTC
Primer 2	ATGTTTGTCGTACAGCGTGAA
Primer 3	TACGGACTCCCAACTGACTGA
Primer 4	ACGTGGAAGAAAACCCCGGTC
Primer 5	GCTCTGCTGGTGTCCGACCTG
Primer 6	GATCGACATCAACGTGGTGAG
Primer 7	AGGTGAACTTCAAGATCCGCC